The Dissertation Committee for Edward Park Certifies that this is the approved version of the following dissertation:

TRIBUTARY IMPACTS, HYDROLOGICAL CONNECTIVITY AND DISTRIBUTION OF SEDIMENT SINKS ALONG THE MIDDLE-LOWER AMAZON RIVER

Committee:

Edgardo M. Latrubesse, Supervisor

Eugenio Y. Arima

Sheryl Luzzader-Beach

Jose C. Stevaux

Jorge D. Abad

TRIBUTARY IMPACTS, HYDROLOGICAL CONNECTIVITY AND DISTRIBUTION OF SEDIMENT SINKS ALONG THE MIDDLE-LOWER AMAZON RIVER

by

Edward Park

Dissertation

Presented to the Faculty of the Graduate School of

The University of Texas at Austin

in Partial Fulfillment

of the Requirements

for the Degree of

Doctor of Philosophy

The University of Texas at Austin

August 2017

Dedication

To my loved family, friends, fellow scholars, and the Amazon.

Acknowledgements

My PhD dissertation, covering multidisciplinary areas from traditional field-based geomorphology to remote sensing, and involving extensive hydro-geomorphological field works in distant regions along the Amazon River in South America, could never have been done only by myself. There are a lot of people contributed to this work, whether directly or indirectly, making my dissertation research productive and successful.

I used to tell my family and close friends that one of the most fortunate things in my life is having met Edgardo. Certainly, most of the acknowledgement for my dissertation research has to go to my supervisor Edgardo Latrubesse who has been not only an academic supervisor, but also a sincere mentor of my career and life during my PhD. I also have to acknowledge my dissertation committee members, Eugenio Arima, Sheryl Luzadder-Beach, Jose Stevaux, and Jorge Abad, who selflessly supported my PhD research in different ways. I first met Eugenio Arima in my first year at UT. I have been a teaching assistant for Eugenio's GIS classes several times and had opportunity to learn from him, not only about GIS, but also properly interacting with students and managing variety of situations in classes, which has contributed toward my professional development. Eugenio was always interested in discussing my research (mostly quantitative method parts) whenever I asked for and provided relevant guidance to me, which most of them have become important foundations of the key methods those have been developed throughout my dissertation research. I thank Sheryl Luzzader-Beach for her huge supports in many stages during my PhD. Sheryl has always encouraged me so I

could advance with confidence in my research. She tirelessly supported me by writing multiple reference letters for different scholarships and fellowships during my PhD. I would like to take this opportunity to appreciate her once again, for her efforts to provide me with the University Continuing Fellowships, and to nominate me for other fellowships on behalf of our department. Without Jose Stevaux, our field expedition, which is an essential component of my dissertation research, would have never been possible. Field works in the Amazon, which involves tremendous efforts from different individuals is very complicated tasks to manage. Jose always played a key role in dealing with these complicated field work logistics for our team. Every time, he kindly transferred multiple hydrogeomorphic equipment from Maringa to Manaus with necessary permits, enabling our field work possible. Jose had been also very liberal with precious suggestions, guidance, and his experiences in the field for me, which were all invaluable resources for me in refining and expanding my knowledge on large river systems. Last but never the least, I thank Jorge Abad for being my dissertation committee member. Jorge provided me with lots of important knowledge which helped me to extend my scope on understanding the river system, particularly on river hydraulics. Also I must reiterate his huge efforts for me during the RCEM conference which happened in 2015 at Iquitos. Jorge gave me accesses to ADCP workshops, which were very important chances for me to participate and learn cutting-edge morphodynamics modeling from different experts around the world. This opportunity indeed advanced in a great degrees my knowledge and skills in fluvial geomorphic analysis.

I would like to extend my appreciations to the two senior scientists whom I was very lucky to have chances to have academic interactions with during my PhD, Thomas Dunne (UCSB) and Juan Restrepo (EAFIT). They provided me with huge inspirations to become an ambitious scientist and guidance which shed light on my dissertation research. I met Tom twice during my PhD, once in Peru and another in Austin. I had an honor to have discussion on my works about the Amazon with one of the giants in our field and receive priceless advices on further directions, which dramatically enriched discussion, especially the Chapter 5 of my dissertation on the Amazon floodplain sediment budgets. Juan has influenced my perspective on fluvial geomorphology to further expand to a continental scale and coastal regions. Through series of interactions with him, I was able to realize the importance of my work on large rivers, not only from geomorphic point of view, but also connecting my research to environmental, political, and management issues those are impacted by the human modification of the system.

My gratitude to our Large Rivers Group members, Samia Aquino, Anwar Slitine, Xiwei Guo, Maximiliano Bayer and Landerlei Santos, cannot be fully expressed. Samia, our group's laboratory manager, has always helped me with all the field works and massive amount of sample managements, and also taught me variety of sediment sample analyses, which are fundamental for fluvial geomorphologist. Anwar, my best friend and also the person I trust the most, has shared a great amount of priceless time with me during our PhDs. We had uncountable and endless conversations on our researches in past years, which I will never forget. Xiwei has provided our team a great support, especially during our Amazon River field works in 2016. Finally, both Maximiliano and

Landerlei should be highly acknowledged in my dissertation for their precious times and tireless efforts in assisting us with the field work in the Amazon. They were never reluctant in joining us for several intensive field works. For sure, without them, the quality of my dissertation as of now, could have never been attained. I also would like to mention our former group members in my dissertation, who are still very good friends of mine, Richard Knox, Katherine Lininger, Christine Bonthius, Vince Clause, Charles Wight, and Eder Merino. Finally, I thank my old friend Niti Mishra, who I used to bother with bunch of remote sensing questions in my early graduate life at UT. Niti was always willing to give me advices, which helped expanding and deepening my knowledge and skills in remote sensing.

I should not miss acknowledging NASA and USGS for making a variety of dataset available for researchers, especially the remote sensing data, which were extensively utilized in my dissertation. HYBAM and ASF have to be acknowledged in my dissertation as well for their generous supplies of field hydrological data of the Amazon Basin, and radar remote sensing data, respectively. My dissertation is supported also from variety of different resources from University of Texas at Austin including College Continuing Fellowship, Bruton Endowed Fellowship, Veselka and LILLAS Grants, and external funding, mainly NSF-DDRI (#1558446) and NSF-FESD (#1338694).

Finally, I would like to thank my family, my wife Yaelim, my son John, my daughter Jenny, my parents, grandparents, and sisters for their unconditional supports and

constant inspirations throughout my life. Especially thanks to my wife, I was able to focus and do my works well. I will miss the time we had together in Austin.

TRIBUTARY IMPACTS, HYDROLOGICAL CONNECTIVITY AND DISTRIBUTION OF SEDIMENT SINKS ALONG THE MIDDLE-LOWER AMAZON RIVER

Edward Park, PhD

The University of Texas at Austin, 2017

Supervisor: Edgardo M. Latrubesse

By integrating hydro-geomorphic data collected from the field with remote sensing data, this dissertation investigates the roles of the tributaries and vast floodplain on suspended sediment distribution patterns in the Amazon River system. To assess the tributary impacts, I focused on the Solimões and Negro Rivers, and found the significant seasonal variations in surface water mixing and distribution patterns; however inter-annual variations between flooded (2009) and drought years (2005) were not notable. It is also observed that the anabranching channel patterns were observed to prevent fast mixing of different water types. Channel-floodplain hydro-sedimentary interactions were investigated over water-saturated floodplain in the lower Amazon by mapping geomorphic mosaic, and characterizing the seasonal flooding and storage patterns. Hydrological connectivity processes over floodplain varied significantly between geomorphic units, which were not correlated with their distance from the river, implying that application of the traditional “flood pulse” model is not applicable in the Amazon. The channel-floodplain connectivity also resulted in failure of the rating curve around

Obidos due to the seasonal water storage in floodplain. Using a series of ADCP data, both the threshold of hydrological connectivity and geomorphic factors influencing the rating curve were assessed, and then the rating curve at Obidos was revised. Floodplain suspended sediment storage along the lower Amazon in between Manacapuru and Obidos was estimated as 79 million tons annually. However sedimentation rates which are determined by the connectivity processes and geomorphologic characteristics of floodplain significantly varied between different reaches, showing downstream increase in the magnitude of sediment sinks. This indicates a nonlinear geomorphic evolution of the Amazon floodplain at least since the Holocene through the river's longitudinal profile.

Through sequences of interrelated chapters, I arrived to the conclusion that the influences of the tributaries and channel-floodplain interactions on the Amazon River system's suspended sediment distribution are significant and their patterns are more complex than expected. The major factor contributing to this complexity is the geomorphologic styles of the river, which are related both to the long-term evolution processes and to the current anabranching channel dynamics. These geomorphologic styles along the Amazon River are different reach-by-reach due to the varying interactive processes with regional tectonics, hydroclimatology and human activities.

Table of Contents

List of Tables

List of Figures

Chapter 1: Introduction

1.1. Background And Motivations

Large rivers play a fundamental role on the planet by transporting eroded sediments from the continent to the ocean; facilitating the transfer of nutrients through biogeochemical cycles; and sustaining complex ecosystems and high biodiversity. They are also important resources (e.g. energy, irrigation, food, recreation, and transportation), a sink (e.g. pollution), and even a hazard (e.g. floods) for human populations. For this reason, the tropics are the most strategic area for the fluvial research, because nine largest rivers on Earth (in terms of water discharge) are located in the tropics or are related to the tropical climatic circulation (Latrubesse et al. 2005). Among these nine largest rivers, six of them are flowing in South America and that 24 out of the 34 largest tropical rivers are in the Amazon Basin or are related to the Amazon rainforest (Latrubesse 2008; Latrubesse et al. 2005). The Amazon river, with a drainage area over six million km^2, discharges 6,300 km^3 each year to the ocean, an amount which comprises approximately 20% of the annual global fresh water discharge (Filizola and Guyot 2004). As the largest river on our planet, the Amazon also has an enormous sediment load discharge ranging 800-1,200 million tons annually (Filizola and Guyot 2009; Meade et al. 1985; Mertes et al. 1996b).

As in other large tropical rivers, sediment plays a major role in the hydrophysical and ecological functions, evolution of the complex channel-floodplain system, and biogeochemical cycles in the Amazon fluvial system (Bayley 1995; Filizola et al. 2011a; Junk 1997). Therefore, mapping sedimentary environments and landforms in the Amazon River Basin and their changes through time have been areas of focus for Amazonian river scientists across disciplines. In the Amazon River, however this goal has been difficult to achieve because the spatiotemporal complexity in the sediment transport patterns is mainly affected by the following aspects. First, large tributaries, such as the Madeira, Negro, and Purus Rivers (some of which are among the largest rivers on Earth), source suspended sediments into the main trunk system those are different in their characteristics with the main trunk system (Park and Latrubesse 2015). Second, the interactions with huge and complex floodplains (Alsdorf et al. 2007; Park and Latrubesse 2017) where the annual sediment fluxes exchanges between the main channel exceed 3,500 million tons along the Amazon River (Dunne et al. 1998b). Traditional in-situ assessments of sedimentary processes concentrating on point-based hydro-sedimentologic measurements are restricted by access, cost, and logistics and therefore, provide limited information on the continuous monitoring of sediment transport through this large and complex fluvial environment. Until recently, the patterns of suspended sediment transport to understand the fluvial morphodynamics in the Amazon River remains largely unknown.

In this context, satellite remote sensing is a relevant and efficient means to regularly monitor the river sediment discharge over the large (regional to continental) area (Mertes and Magadzire 2008b). The variance in reflectivity of sediments (silt and

clay) on river surfaces depending on their quantities enabled researchers to develop nonlinear relationships between spectral signatures recorded at sensors mounted on satellites and surface water color (Doxaran et al. 2002, among others). As surface reflectance is predominantly controlled by the scattering from suspended particles on the water surface (Kirk 1994), the strong response within the visible spectrum as a function of surface sediment concentration at the water surface enabled the acquisition of a river surface sediment load from space (Villar et al. 2012, among others), with root mean square errors of estimated surface sediment concentration less than 20 mg/l (Mertes et al. 1993b). Along the Amazon River in Brazil (Figure 1.01), the suitable applicability of moderate-resolution remote sensing instrument (i.e. MODIS) in modeling surface sediment distribution patterns across time and space has already been demonstrated (Figure 1.02) (Park 2013; Park and Latrubesse 2014). Distinct from previous studies using remote sensing to measure surface sediments in the Amazon Basin (i. e. Kilham and Roberts 2011; Martinez et al. 2009; Mertes et al. 1993b; Montanher et al. 2014; Villar et al. 2012; Villar et al. 2013), a study by Park and Latrubesse (2014) derived field-calibrated models empirically with an unprecedentedly large sample size (N=752 after strict data quality controls) collected over 10 years in three different areas (representing upstream, midstream, and downstream sections) in the Amazon River accounting for the spatiotemporal variability in sediment concentration-reflectance relationships.

By substantially adapting these remote sensing models proposed by Park and Latrubesse (2014) and incorporating extensive sets of field hydro-sedimentological data collected during 2015 and 2016, this dissertation research aims to investigate (1) the roles

of tributaries and anabranching planform, and (2) vast floodplains on suspended sediment distribution patterns in the largest fluvial system on Earth: the Amazon River.

Figure 1.1. Map of the Solimoes-Amazon River and its major tributaries. Three gauging stations used for calibration with remote sensing data are marked: Tabatinga, Manacapuru, and Obidos. (Source: Park and Latrubesse, 2014, used with permission from Elsevier)

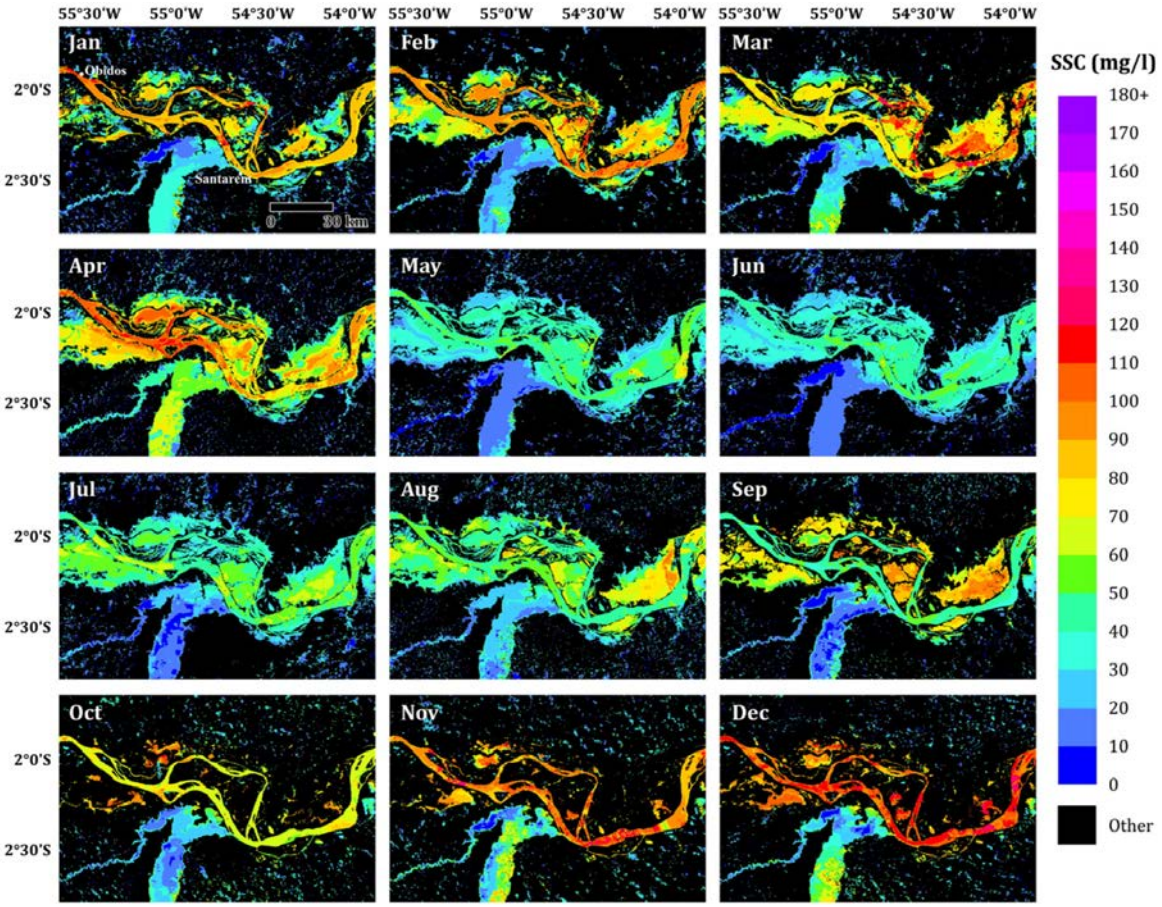

Figure 1.2. Suspended sediment concentration (SSC) distribution maps around Obidos in 2006. One image from each month is displayed. “Other” indicate non-water classes including land, could cover/shade, sand bar and aquatic vegetation. (Source: Park and Latrubesse, 2014, used with permission from Elsevier)

1.2. CONCEPTUAL APPROACH: CURRENT STATUS OF RESEARCH

This study aims to characterize spatiotemporal patterns of suspended sediment distribution patterns in the Amazon River from the two aspects as mentioned above: (1) the impacts of tributaries and (2) channel-floodplain interactions.

1.2.1. Impacts of Tributaries on Suspended Sediment Distribution

River junctions are interfaces where remarkable hydrophysical and geoecological processes take place (Rice et al. 2008, among others). The efforts to understand the role of fluvial confluences have been made across a wide variety of disciplines including geomorphology and sedimentology (e.g. Rice and Church 1998; Zhang et al. 2014), hydraulics (e.g. Constantinescu et al. 2012), and ecology (e.g. Benda et al. 2004; Blettler et al. 2014). The assessments of confluences and downstream hydrodynamics relied on laboratory experiments (e.g. Best and Roy 1991), field measurements (e.g. Biron et al. 2002), and substantially on numerical modeling (e.g. Bradbrook et al. 2001). However, most of the previous studies have focused on small-scale rivers, with widths typically ranging up to several tens of meters, and only a few cases concentrated on large rivers.

Regarding channel patterns, previous studies on confluences concentrate on meandering and braided rivers but, the largest rivers of the world are anabranching systems (Latrubesse 2008). Studies on confluence and post-confluence morphodynamics of large anabranching rivers are scarce with only a few cases on some reaches of the Paraná (Lane et al. 2008a; Parsons et al. 2007; Stevaux et al. 2009a; Szupiany et al. 2009b), Jamuná (Best and Ashworth 1997a), Mekong (Hackney and Carling 2011) and

Amazon Rivers. On the Amazon River, the only existing studies related to confluences are the works by Aucour et al. (2003), Maurice-Bourgoin et al. (2003), Laraque et al. (2009), Filizola et al. (2009), and Bouchez et al. (2010). Except for a study by Bouchez et al. (2010), the others were conducted at the confluence of the Negro River. Aucour et al. (2003) used triple tracers ($\delta^{18}O$, δD, Cl^-) to assess the Negro tributary's chemical contribution to the Solimões River and found that the particulate fraction of major elements (Ca, Mg, Fe, Al, Si) and the dissolved fractions of DOC, Fe, and MN had non-conservative behaviors at the initial mixing of the confluence. Maurice-Bourgoin et al. (2003) examined the mercury (Hg) distribution at the confluence of the Solimões-Negro Rivers, and highlighted the roles of the particulate and dissolved organic carbon in controlling the Hg distribution. Laraque et al. (2009) defined the spatial extent of Solimões-Negro River mixing zone using parameters of velocity, conductivity, turbidity, pH, and temperature measured from a single field campaign in September of 1997. They observed the buoyant effect of the Negro over the Amazon at the confluence, and estimated the complete mixing time and distance were around 30 hours and 100 km, respectively. Filizola et al. (2009)'s observation at the confluence confirmed that the Negro River has a lower discharge during the water level's rising period than during the period of lowest water levels in the Solimões River due to the backwater effect generated by the Solimões River (Meade et al. 1991). Upstream of the Amazon-Negro confluence, Bouchez et al. (2010) studied turbulent mixing patterns of the Solimões and Purús rivers by analyzing the sodium concentration and strontium isotopic composition. Their survey along a 100 km stretch of the Solimões River downstream the Purús confluence revealed

the transversal heterogeneities of the water masses (distinct cross-sectional chemical and isotopic signatures), indicating a poor mixing status between the two rivers.

However, finite collections of point-based and cross-sectional measurements obtained from the field around large river confluences provide limited information on the continuous monitoring of suspended sediment patterns. As of yet, the post-confluence identification of suspended sediment routing through channel junctions is still only partially understood (Best and Rhoads 2008). Further complications are found in large and mega rivers to assess the distribution of suspended sediments at confluences for three main reasons: they present complex anabranching channel patterns (Latrubesse 2008), significant channel-floodplains interactions (Dunne et al. 1998b), and the tributaries that drain different geological and climatic regions than the main trunk system source waters of contrasting physicochemical characteristics. Therefore, there have long been specific needs to characterize the impacts of tributaries on the suspended sediment dispersion patterns along the main systems in a larger spatiotemporal scale.

1.2.2. Channel-Floodplain Sediment Interactions

Understanding the patterns of sediment delivery processes and their budgets between channel and floodplains of large rivers is important because both hydrogeomorphic and biogeochemical alterations in floodplains take place through these interactions (Junk et al. 1989; Mertes 1997). In addition, trapping of water and sediment in upstream reservoirs, construction of human-made levees, or impacts of climate changes (Graf 1999; Latrubesse et al. 2017; Petts 1984; Syvitski et al. 2005) can trigger

widespread and remarkable changes in the floodplain sediment budget and their transference frequencies, which can substantially affect the geomorphic and biogeochemical processes in floodplains (Meade 1996). Transport and deposition patterns of sediment in large rivers floodplains shape the landscapes through constructions of levees, extensive aggradations around floodplain lakes, and progradation of floodplain tributary deltas. In large rivers, these interactions generally occur through overbank flooding and channelized flow through floodplain channel networks (Dunne and Aalto 2013b).

The Amazon River has a continuous exchange of sediment with floodplains, which may rework over 3,500 million metric tons per year (Mt/yr) of sediment fluxes (Dunne et al. 1998b). This large amount of sediment exchanged in each direction between channel and floodplains, i.e. ~1,600 Mt/yr (to channel) and ~2,100 Mt/yr (to floodplains) exceeds the annual sediment fluxes of the Amazon River at Obidos (~1,200 Mt/yr), the lowermost gauge station of the Amazon River (Figure 1.01) (Dunne et al. 1998b). Among these remarkable? interactions, the net sediment transfer to its floodplains is estimated to exceed 500 Mt/yr, indicating the significant role of the floodplains as active sedimentary sinks (Figure 1.03) (Latrubesse 2010; Latrubesse 2015). Along the entire Solimões-Amazon River (~2,010 km), however, these sedimentary sinks are not homogeneously distributed and the most critical sedimentary sinks are located in a downstream section of the river between the confluence with the Madeira River and Obidos (Bourgoin et al. 2007). Although a macro-scale work of Dunne et al. (1998b) and other smaller scale studies in the shorter reaches of the lower

Solimões River (Mertes 1994, 1997) on sediment budget based on limited field observations developed an initial framework to study sedimentary processes along the Amazon River, characterizing the sediment transport and depositional patterns in floodplains and quantifying their budgets in different seasons and years still remains a challenge.

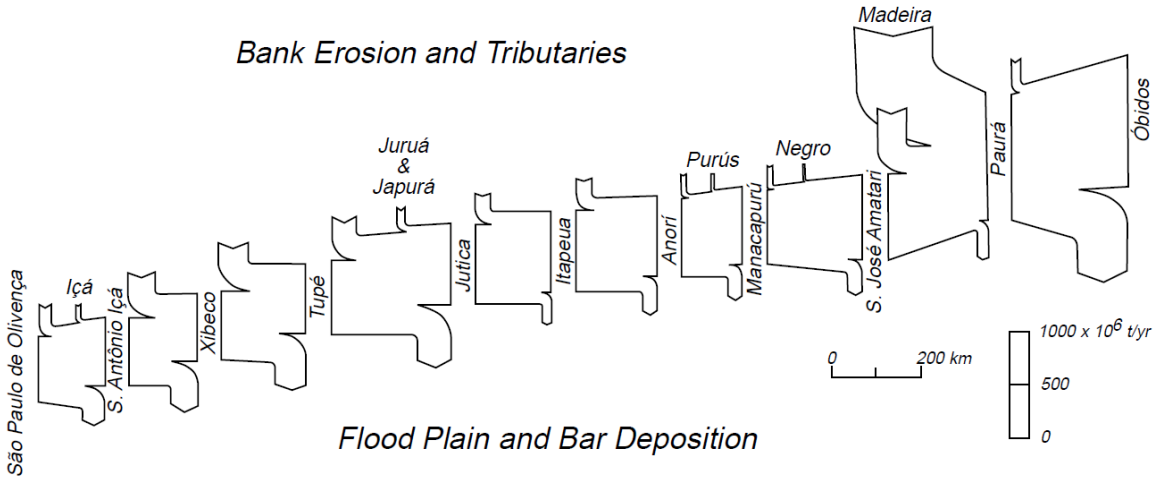

Figure 1.3. Sediment budgets for the Amazon River in between São Paulo de Olivenca and Obidos, showing the budgets estimated (through reach-scale input and output) for each of the 10 reaches (each ranging 150-300 km). (Source: Dunne et al, 1998, used with permission from Geological Society of America)

Although a few studies have recently examined floodplains along the lower Amazon River, their focal points were to assess the water turbidity (e.g. Alcântara et al. 2009), water volume storage (e.g. Alsdorf et al. 2010), vegetation (e.g. Martinez and Le

Toan 2007), phytoplankton (e.g. de Moraes Novo et al. 2006), carbon deposits (e.g. Moreira-Turcq et al. 2004), and substantially on surface water hydrodynamics (e.g. Bonnet et al. 2008; de Paiva et al. 2013; Rudorff et al. 2014a). Only a case study by Bourgoin et al. (2007) tried to calculate the seasonal variability in sedimentation rates (and budgets) in a single floodplain in the lower Amazon River. However, no study has yet been performed to analyze the sediment transport mechanisms and calculate the sediment budgets through the complex hydrogeomorphic networks in large floodplains along the Amazon River.

1.3. RESEARCH OBJECTIVES

The objectives of this dissertation are to combine field acquired hydrosedimentologic data with remotely sensed data to investigate the hydrogeomorphologic and hydrosedimentologic roles of large river tributaries and vast floodplain on the generation of suspended sediment distribution patterns in the largest fluvial system on Earth: the Amazon River. The first research objective is to assess the surface water types mixing and sediment distribution patterns (seasonal and inter-annual) in the confluence of the Amazon River with the Negro River. Here, the role of the anabranching channels on the mixing of different water types is also investigated. The second research objective is to assess the spatiotemporal distribution patterns of the sediment sinks along the lower Amazon River. Addressing this objective involves the quantifications of sediment fluxes through the channel and floodplain budgets (i.e. how

much sediment amount is exchanged between the main channel and floodplain) along the lower Amazon River over different seasons and years.

Chapter 2: Post-confluence Surface Water Types and Sediment Distribution Patterns: the Solimões and Negro Rivers junction[1]

2.1. INTRODUCTION AND BACKGROUNDS

River confluences are important because remarkable hydrophysical and geoecological processes take place here (Rice et al. 2008, among many others). The efforts to understand the fluvial confluences have been made across a variety of disciplines including hydrosedimentology (e.g. Best 1988; Rice and Church 1998), hydraulics (e.g. Best and Ashworth 1997b), and ecology (e.g. Benda et al. 2004). The assessments of confluence hydrodynamics relied on laboratory experiments (e.g. Best and Roy 1991; Escauriaza et al. 2012), field measurements (e.g. Biron et al. 2002; Lane et al. 2008b), and substantially on numerical modeling (e.g. Baranya et al. 2013; Bradbrook et al. 2001). Most of the previous studies, however have been focusing on small-scale rivers, which are tens of meters in their length, and only a few cases were focused on large rivers.

Since the recent developments in hydrographic and geochemical techniques, trials have been frequently made to improve the understanding of large rivers' confluences and

[1] This chapter contains a previously published material from:
Park, E., & Latrubesse, E. M. (2015). Surface water types and sediment distribution patterns at the confluence of mega rivers: The Solimões-Amazon and Negro Rivers junction. *Water Resources Research*, *51*(8), 6197-6213. Edward Park conceived the research idea, collected data, developed methodology, analyzed results and wrote initial version of the manuscript with guidance of supervisor Edgardo Latrubesse.

their post-confluence hydro-geomorphology, such as in some reaches along the Paraná, Jamuna, Mekong and Amazon rivers. In the Paraná-Paraguay Rivers confluence, Parsons et al. (2007) highlighted the importance of bed roughness on water mixing and secondary flows. They pointed out that in large river confluences, many of the important aspects observed within smaller rivers, such as secondary flow cells did not exist. Lane et al. (2008b) supplemented results of Parsons et al. (2007) by adding the significance of momentum ratio along with bed morphology at channel confluence, and addressed that their interactions affect the mixing rates of two river bodies. In the Paraná River, the flow and suspended bed sediment concentration are also affected by the cross-sectional velocity distribution along braided bar confluences, and this might becomes more significant when the ratio between width and depth increases (Szupiany et al. 2009a). In the Paraná River, Stevaux et al. (2009b), (2011) investigated the hydro-morphodynamics at junctions with Paranapanema and Ivaí rivers where there is a confluence islands. Here they observed that the bed form dynamics and the tributary morphology facilitated the formation of an asymmetric confluence. Scours also could be one of typical features in some other confluences. Best et al. (1997b) revealed that bed scour in the Jamuna-Ganges confluence, which could be five times deeper than the mean channel depth, is associated with confluences of large braided rivers. In the Mekong River, Hackney et al. (2011) tried to relate the junction angles with post-confluence channel width along the 284 junctions in the ~2,200 km reach; however, have not found any effects between the two.

Existing studies of confluences along the Amazon River are the works by Aucour et al. (2003), Maurice-Bourgoin et al. (2003), Laraque et al. (2009), Filizola et al. (2009),

and Bouchez et al. (2010). Aucour et al. (2003) used triple tracers ($\delta^{18}O$, δD, Cl^-) to assess the Negro tributary's contribution in its chemical composition on Solimões River and found that particulate fraction of major elements (Ca, Mg, Fe, Al, Si) and DOC, Fe, and MN of dissolved fraction don't have conservative behaviors at the initial mixing of the confluence. Maurice-Bourgoin et al. (2003) explored the distribution of mercury (Hg) the Solimões-Negro Rivers confluence, and highlighted the roles of the particulate and dissolved organic carbon in controlling the Hg distribution. Laraque et al. (2009) determined the extent of Solimões-Negro River mixing using parameters of velocity, conductivity, turbidity, pH, and temperature measured from a field campaign in September of 1997. They observed the buoyant effect of the Negro over Amazon at the post-confluence zone and estimated the time and distance for the complete mixing to be around 30 hours and 100 km, respectively. Filizola et al. (2009)'s observation at the confluence confirmed that the Negro River has lower discharge during the water level rising period than when the water level is the lowest in the Solimões River due to the backwater effect (Meade et al. 1991). Bouchez et al. (2010) studied turbulent mixing patterns of the Solimões and Purús rivers by analyzing the sodium concentration and strontium isotopic composition. Their survey along 100 km of the Solimões River downstream from the Purús confluence revealed the cross-sectional heterogeneities of the waters (e.g. distinct cross-sectional chemical and isotopic signatures), that indicates poor mixing rates.

However, finite collections of point-based and cross-sectional measurements obtained from the field using acoustic Doppler current profiler (ADCP), multi-beam echo

sounder, global positioning system (GPS) and other geochemical applications around large river confluences provide limited information on the continuous monitoring of patterns of suspended sediment distribution and surface water types. Yet, characterizing suspended sediment post-confluence distribution dynamics is still partially understood (Best and Rhoads 2008). There are also further complications in large and mega rivers to assess the distribution of suspended sediments at confluences for the following reasons: they present anabranching channel patterns (Latrubesse 2008), channel-floodplains interactions (Dunne et al. 1998b), and the tributaries that may drain different geological and climatic regions than the main trunk system source waters of contrasting physicochemical characteristics.

In this context, satellite remote sensing could be considered an efficient mean to regularly monitor the river surface sediment distributions over the large (regional to continental) area (Park and Latrubesse 2014). Until now, the only existing works utilizing remote sensing regarding the confluence of large rivers measured junction angles in the Mekong River (Hackney and Carling 2011) and the mixing of waters and suspended sediment dispersion patterns at the Paraná-Paraguay Rivers junction (Lane et al. 2008b). However, tributary impacts along a substantially long reaches at different temporal scales in a large river have not been examined before from remote sensing approach. In this chapter, spatiotemporal patterns of post-confluence water types and suspended sediment distribution patterns are characterized using the ultimate example of large river confluence on Earth, where distinct water types drain: The Solimões-Amazon (muddy-white water) and Negro (black water) rivers. Seasonal and inter-annual variations of

surface water distribution patterns and their mixing rates both through the main channel and branches of the Amazon River along ~150 km in between the confluences with the Negro and Madeira rivers are investigated (Figure 2.01) from a hydrogeomorphic point of view.

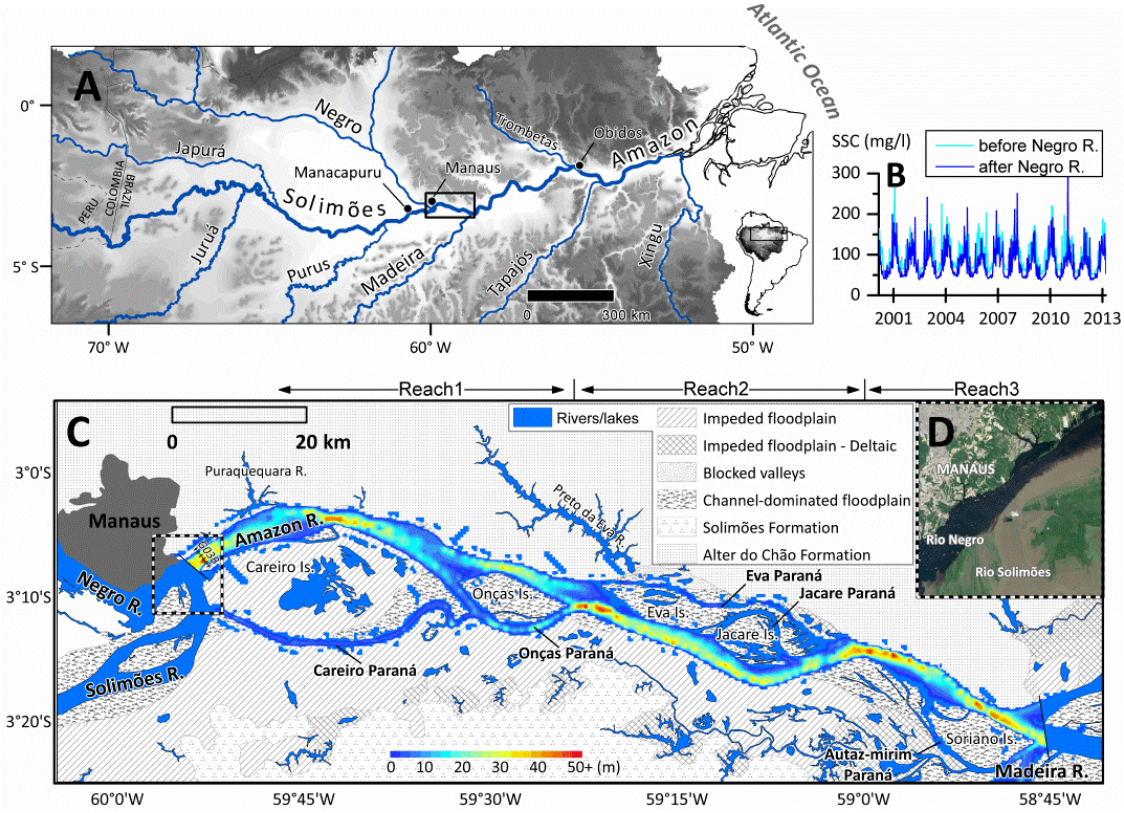

Figure 2.1. A: Large scale map of the Amazon River and the major tributaries. The Solimões-Amazon River (bold line) is segmented into the Solimões River (Brazil border-Manaus) and Amazon River (Manaus-mouth). We use hydrometric data at the Manacapuru gauge station (3° 19’ 37”S, 60° 33’ 13”W). B: Fourteen years (2000-2013, N=1,387 each) of time series surface suspended sediment concentration extracted from MODIS virtual gauge stations in the Amazon River located upstream (~70 km) and downstream

(~100 km) of the Negro River confluence. C: Geomorphic map of the reach of focus (in between the confluences with Negro and Madeira rivers). Descriptions of geomorphology are provided in section 3.1. Interpolated river bathymetry (bounded both ends with black lines) of the study reach is superimposed on the river/lake feature. Location of cross-sectional water quality measurements is indicated (G03B). D: Advanced Land Imager (ALI) natural color image taken on June 17 of 2012 during the flood peak showing impressive meeting of the two rivers at the confluence of the Negro and Solimões rivers (extent indicated in C). This image was downloaded from NASA Earth Observatory at http://earthobservatory.nasa.gov/. (Source: Park and Latrubesse, 2015, used with permission from John Wiley and Sons)

2.2. MATERIALS AND METHODS

2.2.1. Amazon River and the Confluence with the Negro River

For this study, Amazon River is selected, a superlative example of complexity, even for confluence studies. The Amazon extends from the Peruvian Andes to the Atlantic Ocean, draining 6 x 10^6 km^2, which represents 5% of land on Earth (Filizola and Guyot 2004). The mean annual discharge (MAD) of the river is nearly 210 x 10^3 m^3/s, contributing approximately 16% of the annual global fresh water discharge. Thus, it is not surprising that four mega rivers (defined as MAD>17 x 10^3 m^3/s) among the ten largest rivers in the world (Amazon, Madeira, Negro, and Japurá rivers) and three of the largest river confluences are part of the Amazon River System (Latrubesse et al. 2005). The Amazon River also has a sediment load discharge that ranges from 600 to 1300 million tons per year (Mt/yr) estimated at Obidos (Figure 2.01) (Filizola and Guyot 2004; Meade et al. 1985; Milliman and Meade 1983). Over 90% of transported sediments

originate in the Andean headwater tributaries, where weathering occurs due to high relief, intense rainfall and erodible rocks (Filizola et al. 2011b; Meade 1994, 2007) and many catchments are characterized by high sediment yields (Latrubesse and Restrepo 2014). The Madeira River, for example, the largest tributary of the Amazon River, drains the Bolivian-Peruvian Andes and crosses the Brazilian Shield (ancient uplands), and delivers approximately 50% of the total sediment load carried by the Amazon River (Filizola Jr 1999; Filizola and Guyot 2009; Meade 1994). In contrast, other large tributaries draining cratonic areas such as Negro, Tapajós, and Xingu rivers supply very low suspended sediment loads ranging from 10 to 20 Mt/yr (Filizola Jr 1999) to the main stream.

The most famous confluence in the Amazon Basin is that of the Negro River with the Solimões-Amazon, known as the 'meeting of the waters (*Encontro das Águas*)'. This junction is considered the most impressive fluvial site in the Amazon Basin, attracting thousands of tourists every year (Goulding et al. 2003; Sioli 1984) (Figure 2.01D). The two rivers have contrasting sedimentary characteristics (Table 2.01). While the Amazon River is a representative continental mixed terrain river transporting abundant suspended sediments (silt and clay) (Latrubesse et al. 2005), the Negro River is black water with a poor amount of suspended sediment that drains predominantly old terrains of the Guyana shield (Filizola and Guyot 2009; Latrubesse and Franzinelli 2005). The Negro's water tends to be highly acidic (pH ranges 3.8-5.4) due to the high concentration of organic compounds, while the pH of Andean white water is often above neutral. The dark water of the Negro absorbs higher amount of heat than the Amazonian white water. Upon the

confluence of the two rivers, the black and white waters flow side by side without completely mixing for a long distance downstream through the anabranching channels.

Table 2.1. Cross-sectional water quality parameters measured at the confluence (location see Figure 2.01C) during Sep 18-19th of 1997 provided by Laraque et al. (2009). Surface reflectance is acquired from MODIS data on Sep 3rd of 2005 at similar hydrological conditions (river stage) than Sep 18-19th of 1997. The length of the transect is 1,897 m.

Transect code	Left bank distance (m)	Temperature (°C)	Conductivity (µS/cm)	Turbidity (NTU)	pH	Suspended sediment concentration (mg/l)	Surface reflectance
G03B	436	30.8	8.4	5	5.6	14.1	0.022
	1,335	30.7	69.6	79	6.8	72	0.171

2.2.2. Water Discharge and Surface Sediment Concentration Data

Water discharge (Q) and surface sediment concentration (SSC) data of the Amazon Basin since 1972 and 1995, were acquired from the Hydrogeodynamics of the Amazon Basin (HYBAM) (www.ore-hybam.org). Q and SSC data collected during field campaigns in Manacapuru gauge station (Figure 2.01A) were analyzed. Manacapuru was chosen because it is the closest gauge station from the confluence (approximately 75 km upstream of Manaus) and there is no major hydrosedimentary input between them. The Solimões River at Manacapuru has a mean annual Q of 102,458 m^3/s over 40 years (1973-2012) with an average range between the annual minimum and maximum Q of 83,389 m^3/s. The standard deviation of the range is 15,778 m^3/s. Q data at Manus on the

Negro River (grey dashed line) was used which is estimated by Filizola and Guyot (2009), as no discharge measurements are available because of the backwater effect (Meade et al. 1991). Q at Negro seasonally oscillates between 18,000 to 51,000 m^3/s, contributing approximately less than 25% to the Amazon River. During the rising stage, contribution of the Negro Q to the Amazon Q remains below 15%. However, the contribution increases to 30% during the peak stage, and reaches up to 40% during the falling stage.

Annual hydrologic series from the three years were selected in this chapter, representing drought (2005), average hydrological (2007), and large flood (2009) conditions in the Amazon River (see the inset in Figure 2.02) (Filizola et al. 2013; Tomasella et al. 2013) to assess the variability of water mixing and distribution patterns in different hydrologic scenarios. Daily Q data and monthly SSC variability are plotted in Figure 2.02. Three years of hydrographs of daily Q show similar behaviors with the distinct rising (Q_{rising}) - peak (Q_{peak}) - falling ($Q_{falling}$) - low (Q_{low}) stages with flood peaks in early- to-mid June. The highest SSC were observed in January during the Q_{rising}, about five months before the Q_{peak}. During these five months, SSC drops gradually to the lowest when the Q reaches its peak in June. SSC variability also tends to increase with its mean values.

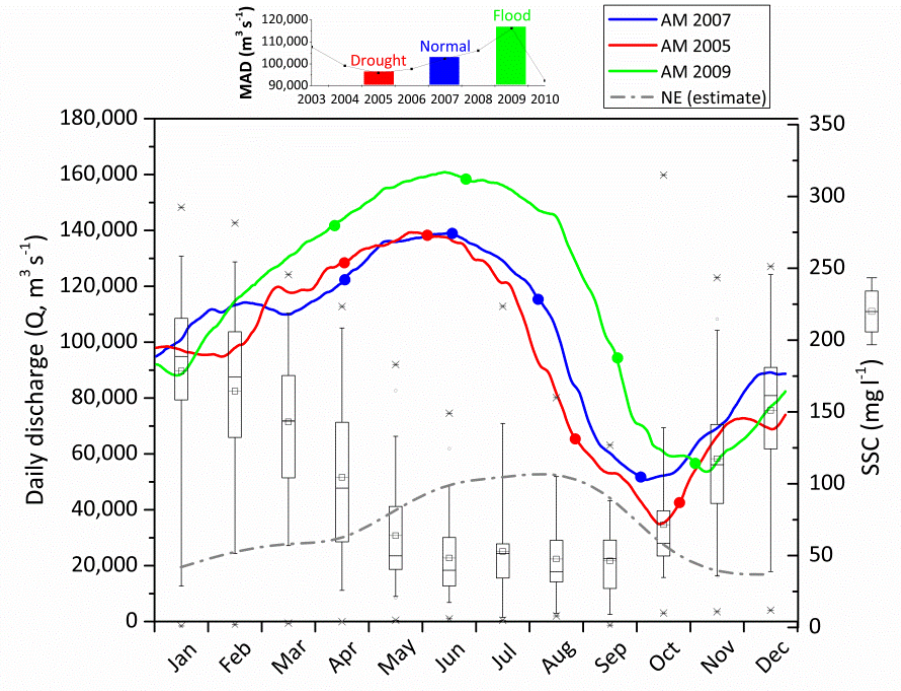

Figure 2.2. Daily discharge measured at Manacapuru for three selected years based on the yearly hydrological conditions: Normal (2007-blue), Drought (2005-red), and Flood (2009-green). MODIS imagery acquisitions dates are marked with filled circle (color corresponding to that of the year) on each hydrograph. We decided specific dates of image acquisition for each season by considering discharges of the Negro River at Manaus in relation to the Amazon River at Manacapuru. Following are the rationales: 1) In the Q_{rising} season, we selected MODIS images from April, because during this period, the largest difference between the Q_{Amazon} *and* Q_{Negro} is observed, 2) MODIS images in June were chosen to represent Q_{peak} as both rivers' discharges reach their peak during this period, with Q_{Negro} remaining relatively homogeneous until September due to the backwater effect, 3) MODIS Images from mid-August to September are selected for the $Q_{falling}$ season, because during this period, steepest drops of both discharges are measured and also the smallest difference between the Q_{Amazon} *and* Q_{Negro} is observed, and 4) MODIS images acquired during October to November is used for the Q_{low} season, since Q_{Amazon} is the lowest, and also the Q_{Negro} at Manaus is the lowest in this period. MAD is shown as the inset graph above the daily discharge hydrograph. Monthly surface sediment concentration data and its variability (box plot) over 11 years (2000-2010) at Manacapuru is also displayed.

2.2.3. Remote Sensing Applications

2.2.3.1. MODIS data and preprocessing

In this study, MODIS 8-day composite data from both Terra (MOD09Q1) and Aqua (MYD09Q1) at 250-m resolution were used, which suitably capture the spatiotemporal variability of surface sediment distribution patterns in the Amazon (Park and Latrubesse 2014). These products are corrected for the effects of atmospheric gases, aerosols, and thin cirrus clouds (Vermote and Vermeulen 1999) and generated from the daily observations (i.e. MOD/MYD09GQ) using constrained-view angle maximum value composite method (processed to Level 3-Version 5) (Huete et al. 2002a) to yields surface reflectance (SR, ranges between 0 and 1) at two bands: band 1 (red, 620-670 nm) and band 2 (near infrared, 841-876 nm). Although SR from both bands (and their ratio for reduced noise) are strongly correlated with the surface sediment concentrations, here band 1 SR is used to map surface sediment distribution patterns because higher and constant sensitivity to sediments in turbid inland water are observed between 600 and 800 nm (Mertes et al. 1993b; Park 2013, among others).

MODIS data were downloaded from the Land Processes Distributed Active Archive Center (LP DAAC, https://lpdaac.usgs.gov/) FTP site for the three years: 2007, 2005, and 2009 (Figure 2.02). The rationale of specific date selection within each season is provided in the caption of Figure 2.02. Collected images are re-projected to South America Albers Equal Area Conic (-60° central meridian) projection using MRTool and

resampled to 250-m using the bilinear interpolation (from 231.66-m in the original tiling system). Further series of image processing steps including controls on pixel quality, filtering solar zenith angle, and interpolating unqualified pixels followed series of methods described in Park and Latrubesse (2014).

2.2.3.2. Tributary's impact and its mixing patterns along the river

To present the impact of the Negro River on sediment concentrations of the Amazon River main channel the MODIS calibration model by Park and Latrubesse (2014) is utilized to extract suspended sediment concentration time series (2000-2013) at two virtual gauge stations located before and after the confluence (Figure 2.01A and B). To examine if there is a significant difference in SSC between the pre- and post-confluence, Student's t-test with pairwise combination was performed. Here statistical significances is detected (p-Value 1.25E-8), suggesting the significant influences of the Negro River on the suspended sediment concentration of the Amazon River main channel.

Internal surface water type variability (i.e. mixing state) of the mainstream is first assessed by calculating the standard deviations (STD) of SR along the river cross-sections. STDs of SR within each polygon were extracted perpendicular to the channel (and branch) centerline, and at 250-m intervals were plotted against river distance downstream from the confluence (Figure 2.03A). This is an efficient way to present the cross-sectional heterogeneity of SR in the river. Through this process, the role of mid-channel islands on surface sediment distributions variability is also assessed. Branches

were separately plotted to examine their SR variability to the anabranching planforms, main channel mixing pattern, seasonality, and annual hydrological conditions.

2.2.3.3. Classifying surface water types

The main objective of this chapter was identifying surface water types and mixing patterns. Although the starting point is the calibration model that was previously developed to estimate SSC in the Amazon River (Park and Latrubesse 2014), this study aims to understand surface water types distributions. Surface water types that have different physical and chemical characteristics (beyond suspended sediments) are related not only to different hydrodynamics and hydrogeomorphologic conditions but also to distinct ecological environments. The reasons we use SR as a proxy and not SSC to discriminate surface water types are as follow: 1) the relationship between particle concentration and the reflectance monotonically increasing (Dring 1984; Mertes et al. 1995b), 2) their nonlinear relationship complicates linear spectral mixture analysis, and 3) there is no SR-SSC model calibrated in any black water body.

The typical distribution of the red band of the river in this study area is shown in Figure 2.04A. The histogram is bimodal with the smaller mean and variance belonging to the Negro and the higher mode to the Amazon. In this example, two river bodies overlap between the modes and the overlapping zone varies for different seasons (e.g. it will expand with increased turbidity during the Q_{rising} or Q_{peak}). Density slicing was applied to MODIS images first to define the surface mixing zones (thus simultaneously determining the pure Amazon and Negro surface water bodies). Density slicing is a one-dimensional classification method, which is an efficient way to differentiate classes when the spectral

reflectance characteristics of heterogeneous surface types are well known. Determining the threshold reflectance value and separating surface types from the image histogram is a key in this method. However, often times it is a challenging task to pinpoint the boundary between classes in a remotely sensed image histogram when transition from one class to another happens continuously, presenting regions composed of multiple spectra, in this case the surface mixture of two rivers.

Spectral mixture analysis was used to further separate the mixed surface water zone. When determining the surface mixing zone, both modes were chosen as boundary so that the entire possible mixed water surface area is present between the two modes. Instead of the commonly used *mean* value of the distribution, the histogram modes was selected as the end-member to be used in spectral mixing model for each water types. Since the two classes are partially mixed, it is problematic to calculate mean (or median) for each distribution. Moreover, the seasonally varying shapes of the image histograms (Figure 2.05B) indicate that the mode better represents the central tendency of each distribution. Spectral mixing approach using these two end-members to separate distinct large river bodies is expected to estimate fractions with high accuracy because 1) no other feature exists in the image other than the two selected end-member spectra, 2) high degrees of spectral homogeneity and heterogeneity within and between classes, respectively (Park 2013) are presented in the histograms (Figure 2.05B), and 3) end-member spectra used in the analysis are extracted individually from each different image (Table 2.02) accounting for the temporal-spectral variability.

There are two reasons for choosing the wide mixing zone bounded by the two modes: 1) since the image histogram expresses a linear sum of two features distributions (Figure 2.04A), it is difficult to identify the extreme values of each distribution lying between the two modes (in this case, lowest and the highest SR values for the Amazon and Negro rivers, respectively) and 2) because of the distinct spectral characteristics of two rivers (muddy-white versus black water bodies), the range of SR of one river does not include SR value at the mode (and mean) of the other river. SSC from Negro River is usually below 10 mg/l, while SSC below 10 mg/l in the Amazon River at Manacapuru has been recorded only five times over 17 years (since 1995, N=450). Thus, considering outside the mixing zone was relevant to be considered either pure Amazon or Negro rivers zones.

Subsequently, a linear spectral mixture model (SMM) (Adams et al. 1986) is applied on each pixel in the mixing zones for the 12 selected images to decouple the Amazon and Negro rivers and retrieved the portions (fraction image) occupied by each river body within each pixel. Extremes of the surface mixing zone (i.e. histogram modes) were chosen as the end-member for each water body in solving the SMM. SMM models the reflectance value of a spectrally mixed pixel as a linear combination of end-member spectral reflectance weighted by the fraction (sub-pixel area/250^2) of each end-member. The formula of SMM implemented in this analysis is:

$$P_{(x,y)} = \frac{R_{Am}A_{Am} + R_{Neg}A_{Neg}}{250^2} + \varepsilon \ , \quad A_{Am} + A_{Neg} = 250^2$$

where $P_{(x, y)}$ is the surface reflectance of pixel in the MODIS image. $R_{Am,}$ $R_{Neg,}$ and $A_{Am,}$ A_{Neg} denotes the end-member reflectance and area of Amazon and Negro rivers, respectively. ε refers to the residual term (RMSE) of the model, which fluctuates around zero. Selected end-members are also summarized in Table 2.02.

Table 2.2. Summary of remote sensing dataset and selected end-members

Date [a]	Valid pixels (%) [b]	Selected end-members		Statistics [c]		Annual condition	Season
		Negro R.	Amazon R.	μ	∂		
2007 Apr. 15	97	0.037	0.116	0.092	0.031	Average	Rising
2007 Jun. 18	99	0.023	0.069	0.054	0.021		Peak
2007 Aug. 5	99	0.027	0.065	0.068	0.040		Falling
2007 Oct. 8	96	0.076	0.120	0.071	0.043		Low
2005 Apr. 15	99	0.047	0.124	0.087	0.032	Drought	Rising
2005 Jun. 2	98	0.020	0.067	0.047	0.022		Peak
2005 Aug. 29	99	0.024	0.097	0.089	0.029		Falling
2005 Nov. 1	97	0.025	0.140	0.107	0.045		Low
2009 Apr. 7	96	0.024	0.069	0.055	0.020	Flood	Rising
2009 Jun. 26	99	0.024	0.051	0.020	0.023		Peak
2009 Sep. 22	99	0.038	0.075	0.043	0.034		Falling
2009 Nov. 9	96	0.070	0.121	0.060	0.048		Low

[a] Dates indicate the first day of 8 successive image acquisitions

[b] Portion of valid pixels within the channel reach after quality control prior to gap-filling interpolation.

[C] Statistics are calculated for the whole river study reach.

The Amazonian fraction images ($A_{AM}/250^2$) are further classified into two classes: an Amazon dominated class (C_{AD}, 0.5<fraction<1) and a Negro dominated class (C_{ND}, 0<fraction≤0.5). Note that the pure Amazon class (C_{AR}) and the pure Negro class (C_{NR}) are already defined through density slicing prior to the SMM analysis. Surface water type classification maps and the Amazonian surface water portion variability are presented in Figure 2.05B. Amazonian surface water portion is calculated separately for the main channel and branches as following:

$$\frac{count(C_{AR}) + \sum \frac{A_{AM}}{250^2}}{count(pixels)}$$

where $count(C_{AR})$ and $count(pixels)$ are number of pixels in the pure Amazon class and the total number of pixels being calculated, respectively (Figure 2.05C). These classification results are used to assess the distribution patterns of the surface water types in different hydrogeomorphic scenarios. A geomorphic map of the study area was generated using the classification by Latrubesse and Franzinelli (2002) and Latrubesse (2012) that describes the reach immediately upstream of the study area. Two L-band HH-polarization images from dry and wet seasons of 2007 (processed to level 1.5) acquired by PALSAR (downloaded from https://www.asf.alaska.edu/) were extensively used for the geomorphic mapping of this area aided by Landsat TM images.

2.2.3.4. Incorporating bathymetric data

Spatial variability of bathymetry information is incorporated into the interpretations of surface suspended sediment distribution patterns in this region because river bathymetry is critical in controlling flow hydrodynamics and sediment transport. Complete river bed topography is created using kriging geostatistics, which the formula is written as:

$$\hat{z}(x_0) = \sum_{i=1}^{n} \lambda_i z(x_i), \quad \sum_{i=1}^{n} \lambda_i = 1$$

where $z(x_i)$ is measured depth at *n* locations, $\hat{z}(x_0)$ is the estimated depth at spatial coordinate x_0, and λ_i is the weight. $z(x_i)$ were supplied from the Garmin Bluechart (G2-HXSA009R), that integrates existing digitized government and other official navigation charts of the region as isolines and points. Anisotropic kriging technique was adapted (total N=14,009) with the deterministic channel trend controlled by the local polynomial regression considering the downstream influence through the channel bathymetry (Figures 2.01C and 7) (Merwade et al. 2006). Kriging is often referred to as the best unbiased estimator (Isaaks and Srivastava 2011) that provides an optimized weight to a limited number of depth measurements because these weights are estiamted based on distance and spatial autocorrelation between every measured points. Traditionally, isotropy is assumed in interpolation methods, namely Inverse distance weight, Natural neighbor, Ordinary kriging, where the spatial trend is considered the same regardless of the direction. Ordinary kriging implements an omni-directional semivariogram model. However, it has been simulated that considering the directional

influence of the dataset (i.e. anisotropy) in interpolating scattered depth measurements substantially outperforms other isotropic interpolation methods in retrieving a continuous river channel bathymetry (Merwade et al. 2006). This anisotropic kriging takes care of the spatial trend (deterministic) using regression models and estimates the remaining residuals (stochastic) through the two-dimensional semivariogram presenting azimuthal lag directions.

Depth measurement data at every 500 m along the 6 ADCP cross-sections from Laraque et al. (2009) and 8 cross-sections extracted from the Brazilian Navy bathymetric charts used by Franzinelli and Igreja (2011) were compared with interpolated channel bed topography for cross validation of my interpolated bathymetry. The values by Laraque et al. (2009) obtained during Sep 18-23rd of 1997 were corrected to the average of the minimum historical stages at Manacapuru, which is used to design the bathymetric charts (see next section for detailed correction methods). Root mean square error (RMSE) of 1 m was calculated between the field and interpolated depth points with globally consistent residuals over the different channel depth. Flowchart showing the methodological details is in Figure 2.3.

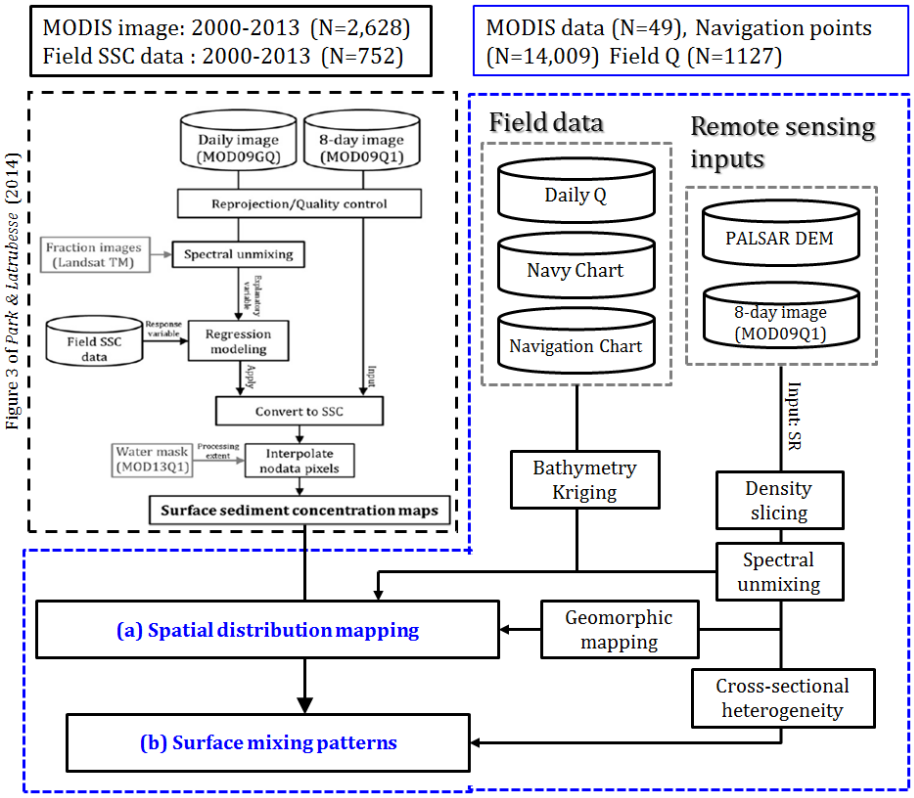

Figure 2.3. Flowchart of methodological details. Bounded by black dashed line is a calibration model to retrieve SSC developed in the previous publication (Park and Latrubesse, 2014). Bounded by blue dashed line is an extended model based on field and remote sensing data to run series of analyses to map (a) spatial distribution of surface water types, and (b) their mixing patterns from the confluence.

2.2.3.5. Water flow survey at the confluence

Water flows data around the confluence (location G03B in Figure 2.01) during a field work in August 28th, 2015 was collected. Survey was performed over the cross section starting from the left bank toward the right bank of the Careiro Island (≈2.5 km). We used GPS-linked ADCP (Teledyne Rio Grande 600 kHz) for the flow velocity and acoustic backscatter measurements. Acquired transect data is further processed using

Velocity Mapping Toolbox to visualize the complex flow structure (including depth-averaged flow velocity and transverse profile) of the confluence.

2.2.3.6. Water level correction methods to cross-validate bathymetry of the channel

Depth measurement data at every 500 meters along the six cross sections (transect code G3~G8) from Laraque et al. 2009 were compared with interpolated channel bed topography for cross validation. For comparison of cross-sectional depth data measured at different stages by Laraque et al. 2009, the following correction methods were applied: interpolated bathymetry was based at 8.6 meter, the inter-annual mean low water level measured at Manacapuru (N = 41, 1972-2012) (Table 2.03). Then the discrepancies between 8.6 meter and the water levels at Manacapuru during September-18, 20, 21, 22, and 23 of 1997 were calculated, when the field campaigns were conducted by Laraque et al. 2009 (Table 2.04). Calculated discrepancy values were subtracted from Laraque et al. 2009's cross sections to retrieve water level-corrected cross section for inter-seasonal comparison with interpolated bathymetry data. Root mean square error (RMSE) of 1 meter was calculated between the selected field and interpolated depth points with globally consistent residuals over different depths. This slight disagreement in RMSE is considered negligible, which may be attributed to the differences in resolution between the interpolated surface (coarser) and transect scanned from ADCP (finer).

Table 2.3. Lowest water stages of each year measured at Manacapuru.

Year	Date[a]	Lowest WL (cm)	Lowest WL (m)
1972	1110	1066	10.66
1973	1118	1146	11.46
1974	1203	1252	12.52
1975	1124	1004	10.04
1976	1120	884	8.84
1977	1012	1125	11.25
1978	1010	1095	10.95
1979	1021	789	7.89
1980	1026	845	8.45
1981	1021	774	7.74
1982	1102	877	8.77
1983	1019	748	7.48
1984	1027	991	9.91
1985	1126	1030	10.3
1986	1015	1182	11.82
1987	1105	849	8.49
1988	1012	826	8.26
1989	1018	1121	11.21
1990	1027	670	6.7
1991	1103	667	6.67
1992	1107	835	8.35
1993	1023	1011	10.11
1994	1122	1101	11.01
1995	1029	552	5.52
1996	1014	941	9.41
1997	1106	495	4.95
1998	1028	557	5.57
1999	1121	750	7.5
2000	1209	860	8.6
2001	1030	745	7.45
2002	1029	801	8.01
2003	1030	989	9.89
2004	1112	1022	10.22
2005	1022	508	5.08
2006	1021	748	7.48
2007	1026	808	8.08

2008	1026	872	8.72
2009	1127	768	7.68
2010	1022	356	3.56
2011	1111	742	7.42
2012	1125	672	6.72
	μ	855.46	8.6
	σ	201.97	2.0

[a] MMDD

Table 2.4. Water level correction values.

Laraque et al. (2009)			
Date	Transect code	WL (m) at Manacapuru	Difference from inter-annual Mean Low WL
19970918	G03B	9.9	+ 1.3
19970920	G04	9.42	+ 0.82
19970921	G05	9.18	+ 0.58
19970922	G06, G07	8.95	+ 0.35
19970923	G08	8.7	+ 0.1

2.3. RESULTS AND DISCUSSION

2.3.1. Geomorphic style of the reaches

The middle Amazon River presents a moderate anabranching pattern with low sinuosity and dominated by suspended load. The main channel of the Amazon at the study area could be characterized by a straight channel belt (sinuosity<1.24), low gradient (1.8-2.1 cm/km), low stream power (6-12 W/m^2), w/d ratios typically ranging from 60 to 120, and a sandy bed load (Latrubesse 2008). The Solimões-Amazon anabranching system does not divide into more than three branches at the same location and flows between heavily vegetated mid-channel islands. The system occasionally generates

episodic sand bars and most of the reaches are confined by stable levee complex (Latrubesse 2008; Rozo et al. 2012). Branches can be more sinuous than the main stem, but they generally have short lateral distances (Latrubesse and Franzinelli 2002; Mertes et al. 1996a).

The major floodplain units are impeded and channel-dominated floodplains located at the southern side (right bank), with numerous rounded lakes subject to the influence of the main channel floods. Northern side of the river (left bank) is predominantly upland on older rocks (*terra firme*). Enduring islands and levees established by a continuous main channel overbank vertical accretion favor the development of a complex patchy pattern of impeded and channel-dominated floodplains. Although there is active overbank sedimentation, the floodplain is still partially 'incomplete', presenting topographic amplitude with both positive (e.g. scroll bars and levees) and negative geomorphic features that trap sediments, such as rounded lakes. They typically develop on a very flat surface and have complex networks affected by inundation dynamics of the main and floodplain channels. Levee lakes form on the side of the sediment laden main channel and receive direct overbank sedimentation from the river. Sedimentary layers in this geomorphic unit result mainly alterations of fine and sandy deposits, and form levee heights up to 10 m in relation to the mean low water level (Latrubesse 2012). Large islands formed by sandy bar deposits and the mixture of features developed by both the lateral and vertical accretions are typical in large anabranching rivers (therefore some islands present a mixture of both impeded and channel-dominated floodplains).

Branches (secondary channels) are locally called ‘paranás’ (de Andrade 1956), when it reconnects to the main channel. Island levee lakes experience annual water level oscillation from the river. Islands are considered to be persistent over 2,000 years indicated by ^{14}C dating results in Careiro Island, (Latrubesse and Franzinelli 2002; Rozo et al. 2012, Sternberg, 1960). Accounting for the regional geomorphic variability, the river was further segmented into three reaches, using two nodal points (geologic controls) where the river becomes a single channel system (local narrowest sections) (Figure 2.01C). Reach 1 encompasses the large Careiro and Onças Islands which are surrounded by straight paranás on the south side. These paranás consistently discharge water from the Solimões River (Figure 2.06B), as well as carry abundant suspended sediment and transfer suspended sediments to floodplains on both sides. *w*/*d* ratio of these secondary channels are relatively high (>150), presenting a similar value with the main stream of the middle Amazon River. Careiro Island can be characterized by an internal impeded floodplain that is morphologically controlled by levees embracing internal big rounded lakes (Lago do Rei), while Onças Island is dominated by channel-dominated floodplain where the scroll bar morphology is extensively developed. Two major paranás in Reach 2 are Eva and Jacare paranás. Eva Paraná has the lowest sinuosity and *w*/*d* ratio in the study reach. Eva Paraná is predominantly filled by black water acting as a corridor for the Negro River and receives seasonal interactions with Preto da Eva River, which forms a blocked valley at its mouth. Incised by these paranás, two islands are formed (Eva and Jacare islands), which are mainly composed of channel-dominated floodplain with complex channelized network flows. Unlike paranás in Reach 1 and 2, Autaz-mirim

Paraná flows through deltaic-impeded and channel-dominated floodplains (Soriano Island), and presents high sinuosity and *w*/*d* ratio. Black water tributaries from huge and complex inter-connected delta system converge into the Autaz-mirim Paraná through a narrow connection eastward to meet the Madeira River. These islands have mostly undergone erosion (15-30 m/yr) over the past 30 years according to Rozo et al. (2012); however they maintain similar channel widths that range from 700 to 750 m. Morphometric characteristics of paranás were summarized in Table 2.05.

Table 2.5. Summary of characteristics of paranás. Width and depth are in meters.

Paranás	Sinuosity	Width (w_{bf})[a]		Depth (d)[b]		w/d ratio[c]
		μ	∂	μ	∂	
Careiro	1.21	955	222	4.7	0.9	203.19
Onças	1.22	1386	249	8.9	7.3	155.73
Eva	1.05	495	111	3.6	1.1	137.50
Jacare	1.67	791	86	-	-	-
Autaz-Mirim	1.33	719	133	2.8	1.8	256.79

[a] width measured at bankfull stage.
[b] calculated from interpolated bathymetry.
[c] calculated from means of w_{bf} and d.

2.3.2. Seasonal and Inter-annual Variability of the Cross-channel Reflectance

Temporal variability of the STD along the main channel and its branches are assessed individually (Figure 2.04A) and are summarized in Figure 2.04B using mean and the variability of STD for each reach and branches. STD along the main channel

decreased downstream (i.e. toward the mixing of surface waters), then remained relatively constant throughout the observed periods. The STD along the main stem is the highest during the standard year (2007) followed by the drought year (2005), and last the flood year (2009). The highest and lowest STDs were observed during Q_{rising} and Q_{peak} seasons, respectively, indicating that the surface water mixing rate was high during the Q_{peak} and relatively low during the Q_{rising}. The highest variability in Q_{rising} can be attributed to the large differences between Q_{Amazon} and Q_{Negro} during this period. In Q_{peak} when the Q_{Amazon} and Q_{Negro} reach their peaks, they mix faster with increased turbidity. Similar discharge levels at the Q_{rising} and Q_{peak} in 2007 and 2005 may have resulted from the similar seasonal variations (Figure 2.02). In 2009, STD along the main channel is relatively constant and it remains lower than other two years with less seasonal variability (Figure 2.4B).

Transversal surface mixings through the main channel of the Amazon River were not complete before meeting the confluence with the Madeira River for all investigated years. Pure Amazon or Negro Rivers did not exist downstream of the nodal point dividing Reach 1 and 2 (~65km from the confluence) during most of the periods. Thus, mixed surface water occupies the Amazon main channel in Reach 2 with each of the Amazon and Negro, dominating waters sharing the channel surface almost equally (Figure 2.6C main channel) which might be related to asymmetric bathymetry. Only during the Q_{rising} when the difference between Q_{Amazon} and Q_{Negro} is the largest (Figure 2.02), the Pure Amazon class extends further downstream toward the nodal point dividing reach 2 and 3, as observed in 2007 and 2009 (Figure 2.6B). In Reach 3, although

predominantly occupied by the Amazon dominated water throughout the periods, black water from the Negro River still flows along the left bank of the main channel with less than 15% surface domination within the reach. The observations in this study are different from the previous studies by Laraque et al. (2009) and Maurice-Bourgoin et al. (2003), where they present the downstream distances for the complete mixing from the confluence along the Amazon River main channel to be 100 km and 25 km, respectively. To summarize, most of the pure waters disappeared upon passing Reach 1; however complete mixing of the two waters were not achieved until meeting the Madeira River confluence. I consider that the existence of the anabranching patterns helps to prevent fast mixing in a shorter distance.

Branches (Paranás) generally present smaller STD and its variability than the main channel (Figure 2.4B). Individual paranás present their specific water types because they are fed exclusively by either the Amazon or Negro rivers' portions of the main channel, at the water surface level. Most of the cross-sectional variability detected in the branches is temporary, and no remarkable inter-annual variability. Branches in Reach 1 (Careiro and Onças paranás) are dominated by the Amazon River muddy water (Figure 2.6B). Therefore the STD in the branches is low and stable without interference from other types of water. At CS1 in Figure 2.4A, STD slightly increases in the Q_{rising} of 2005, and 2007 when the main channel bifurcates through the Onças Island. Careiro and Onças paranás flow around two large heavily vegetated islands, which have similar heights with surrounding floodplain, without significant input from floodplains channels. In Reach 2, STD oscillates along the branches only during the Q_{rising} when the muddy Amazon River

water enters partially into the Eva Paraná. It is considered that this oscillation is due to the large differences between Q_{Amazon} and Q_{Negro} during Q_{rising} (Figure 2.02). In Q_{rising} the Amazon River flow becomes strong sufficiently to generate inflow through the Eva and Jacare paranás, which are incised in the northern floodplains. An immediate increase at CS2 in Eva Paraná is associated with the black water tributary entering to the paraná from the Preto da Eva River (Figure 2.1). Most of the blocked valleys along the Amazon River normally maintain seasonal connections to the main channel (or its anabranches) (Latrubesse 2012). Preto da Eva River is the largest black water blocked tributary in the studied area. During Q_{rising} this blocked valley lakes interacts with the river, introducing surface water variability along the Eva Paraná (see Q_{rising} in Figure 2.4A Paranás CS2). However, during $Q_{peak,}$ interior sedimentation in the valley lake and backwater effect produced by the Amazon River prevents their interactions (see Q_{peak} in Figure 2.04A Paranás CS2). Another surge at CS3 in the Eva Paraná during Q_{rising} is because of the surface water interactions (overbank diffusion) with the Jacare Paraná (see Q_{rising} in Figure 2.04A Paranás CS3). The lower heights and the narrow widths of the Eva and Jacare islands (than the adjacent floodplains) are susceptible to the seasonal inundation from the river. This phenomenon is most pronounced in 2007, followed by 2005 and then 2009. In Reach 3 (around CS4), surface water variability in the branch (Autaz-mirim Paraná) is introduced by the black water export from the extensively distributed impeded deltaic lakes in the vast floodplain. The highest variability is observed in 2005 Q_{rising} and 2009 Q_{peak}, probably due to the local runoff (Figure 2.4A Paranás CS4).

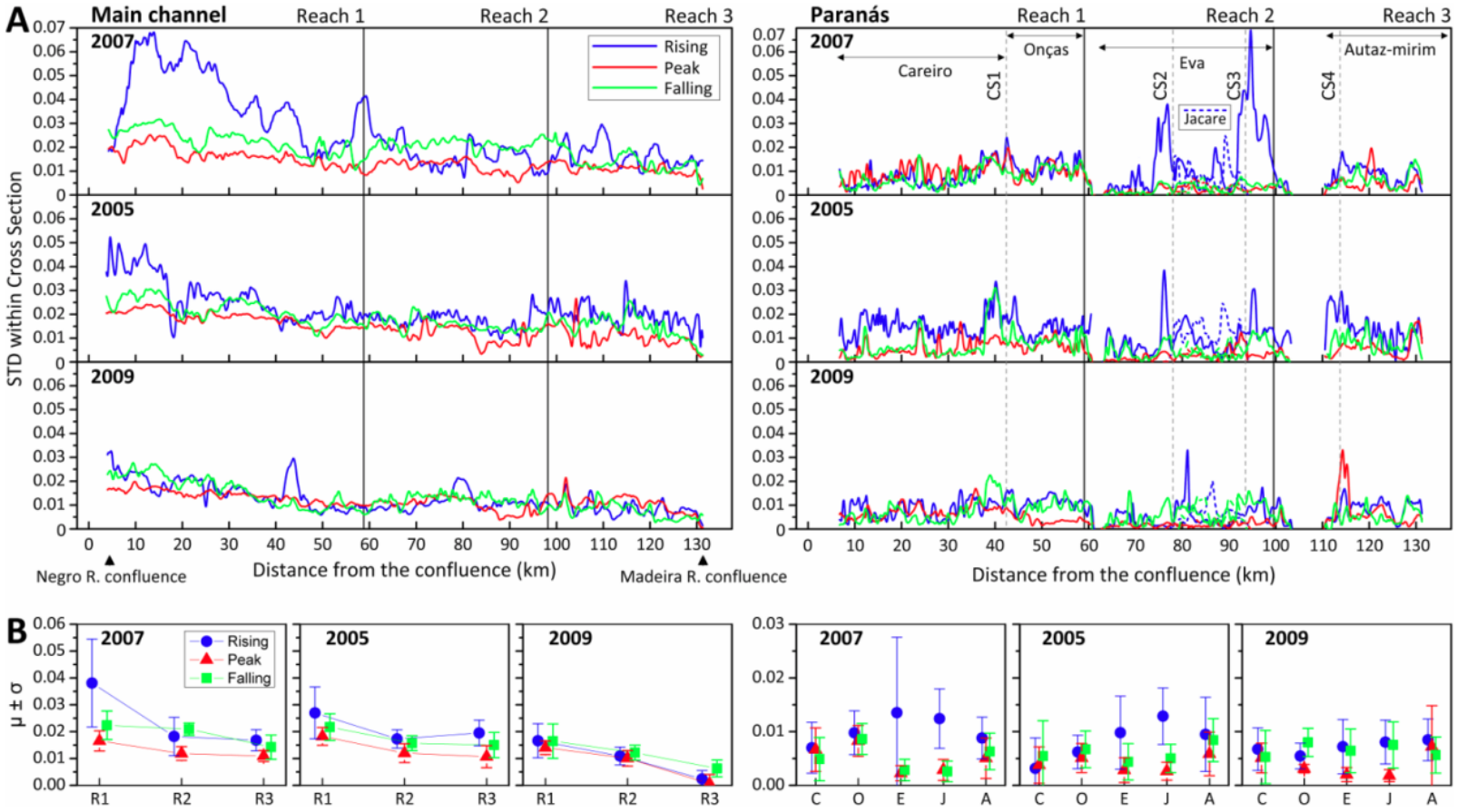
A
Main channel
Reach 1
Reach 2
Reach 3
2007
2005
2009
Rising
Peak
Falling
STD within Cross Section
Negro R. confluence
Distance from the confluence (km)
Madeira R. confluence
Paranás
Careiro
Onças
Eva
Autaz-mirim
CS1
CS2
CS3
CS4
Jacare
B
μ ± σ
R1
R2
R3
C
O
E
J
A

Figure 2.4. A: Plots of standard deviations (STD) of cross-sectional SR by along-river distance downstream of the confluence both for the main channel (left) and paranás (right). Note that STD along the downstream shows cross-channel heterogeneity of surface water types; however, it does not tell which water types are dominant. Four Critical Sections (CS) in paranás are indicated where STD increased abruptly inter-annually in relation to the local geomorphology. B: STD mean and its variability of each reach (B-left) and paranás (B-right) retrieved from different seasons and years in the main channel and paranás. Note the decreasing global trend in the main channel and different Y-axis scales between the main channel and paranás. X-axis abbreviations: R1=Reach 1, R2=Reach 2, R3=Reach 3, C=Careiro, O=Onças, E=Eva, J=Jacare, and A=Autaz-Mirim paranás.

2.3.3. Temporal Variability in End-members

Descriptive statistics in Table 2.2 show the seasonal to inter-annual surface water responses in the study reach. Regardless of the annual hydrological conditions, the highest mean SRs in the whole channel occurred during the Q_{rising} or Q_{low} seasons. In contrast, the lowest mean SRs were observed during the Q_{peak} due to the dilution with the water. Q_{peak} seasons presented the lowest standard deviations within a year with the highest variability shown in the Q_{low} season. During the Q_{peak} in the three assessed years, the lowest end-member SRs were observed, followed by $Q_{falling}$ and Q_{rising}, which is similar to the surface sediment concentration cycle at the Manacapuru (Figure 2.2). 2007 case is shown as an example because seasonally varying patterns were similar for the three years (Figure 2.5B).

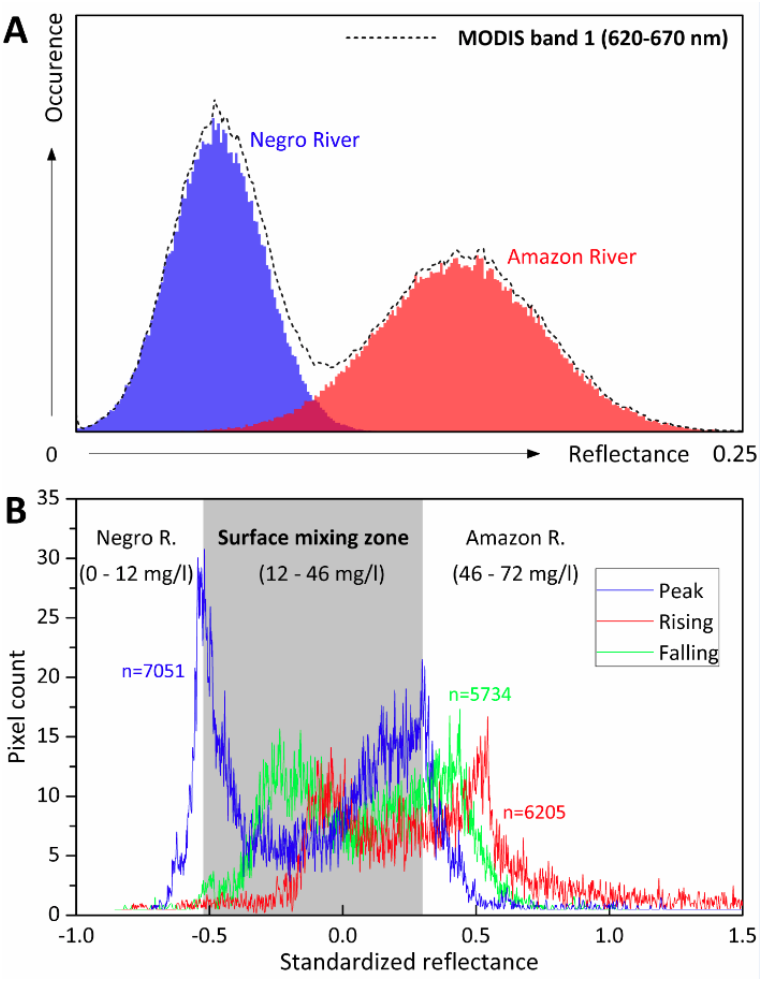

Figure 2.5. A: Typical spectral signature histograms of the Negro and Amazon Rivers in the study reach. Mean reflectance value for the Negro River is lower than that of the Amazon River, because black water bodies absorb substantially higher rates of solar radiation than white water. Very small reflectance variability (standard deviation) characterizes the black water type. In the MODIS band 1 (red), reflectance from the river surface is measured as an integral of the two curves from Negro and Amazon rivers (black dashed line). B: Histograms of the whole river reach studied from three seasons in 2007: Q_{rising}, Q_{peak}, and $Q_{falling}$. Histogram from Q_{low} season is excepted because its behavior is similar to that of Q_{rising}. The mixing zone of Q_{peak} is highlighted with grey background. SSC ranges of each class in Q_{peak} are also displayed. Reflectance from each season is standardized (X-axis) by the inter-seasonal

Surface water types are classified into four classes: C_{AR}, C_{AD}, C_{ND}, and C_{NR} as described in previous section (Figure 2.6B. Surface waters start to mix quickly upon the confluence. Pure portions of the Negro river (C_{NR}) decrease fast and completely disappear before passing the Careiro Island. Water from the Negro River never flows close toward the right bank within the study area throughout the whole investigated years. Thus, it can be concluded that sedimentation over the southern floodplains is exclusively a process of the muddy Amazon River water. C_{AR} endures relatively longer than the Negro River along the main channel. During Q_{rising} in 2007 and 2009 when the discharge difference between two rivers is the greatest, C_{AR} remains until Reach 2 alongside the right bank. Throughout all hydrologic conditions, C_{AR} encircles Careiro Island (the largest island in the Amazon River), while the C_{AD} mostly encircles Onças Island. In contrast to the general dominance of Amazon in Reach 1, Negro's surface occupation increases in Reach 2 and the water surface coverage becomes similar with the Amazon. The pattern in Reach 2 results from the asymmetric channel bathymetry (Figure 2.7c), the anabranching pattern, and the inputs from black water tributaries from the northern side. Paranás in Reach 2 are mainly fed by black waters that encircle Eva and Jacare Islands most of the time. In Reach 3, surface water in both the main channel and the branch is dominantly characterized by the Amazon River.

Figure 2.6C summarized the spatial distribution patterns of surface water types in each reach, by displaying the portion occupied by the Amazon River. The distribution patterns over the surface of the river might slightly underestimate the actual depth-

integrated water flowing behavior, because the warmer and lighter water in the Negro tends to float over the cooler and heavier water in the Amazon (Laraque et al. 2009) (Figure 2.8). In Reach 1, Amazonian dominance both along the main channel and paranás are high. However, seasonal oscillations in the Amazonian dominance are observed to be the highest during the Q_{rising} and the lowest during the Q_{peak} or $Q_{falling}$ throughout the studied years. Amazonian dominance is decreased in Reach 2. As mentioned before, this is mainly attributed to the bathymetric control as river depth becomes dramatically shallower on the left side of the bank when bifurcating through the Eva Island. This mid-channel island in anabranching systems has been typically a stable feature colonized by vegetation over several centuries. As in Reach 1, the Amazonian dominance is the highest during the Q_{rising}. Reach 3 is characterized by high dominance (mostly >0.85) of the Amazon River (Figure 2.6C).

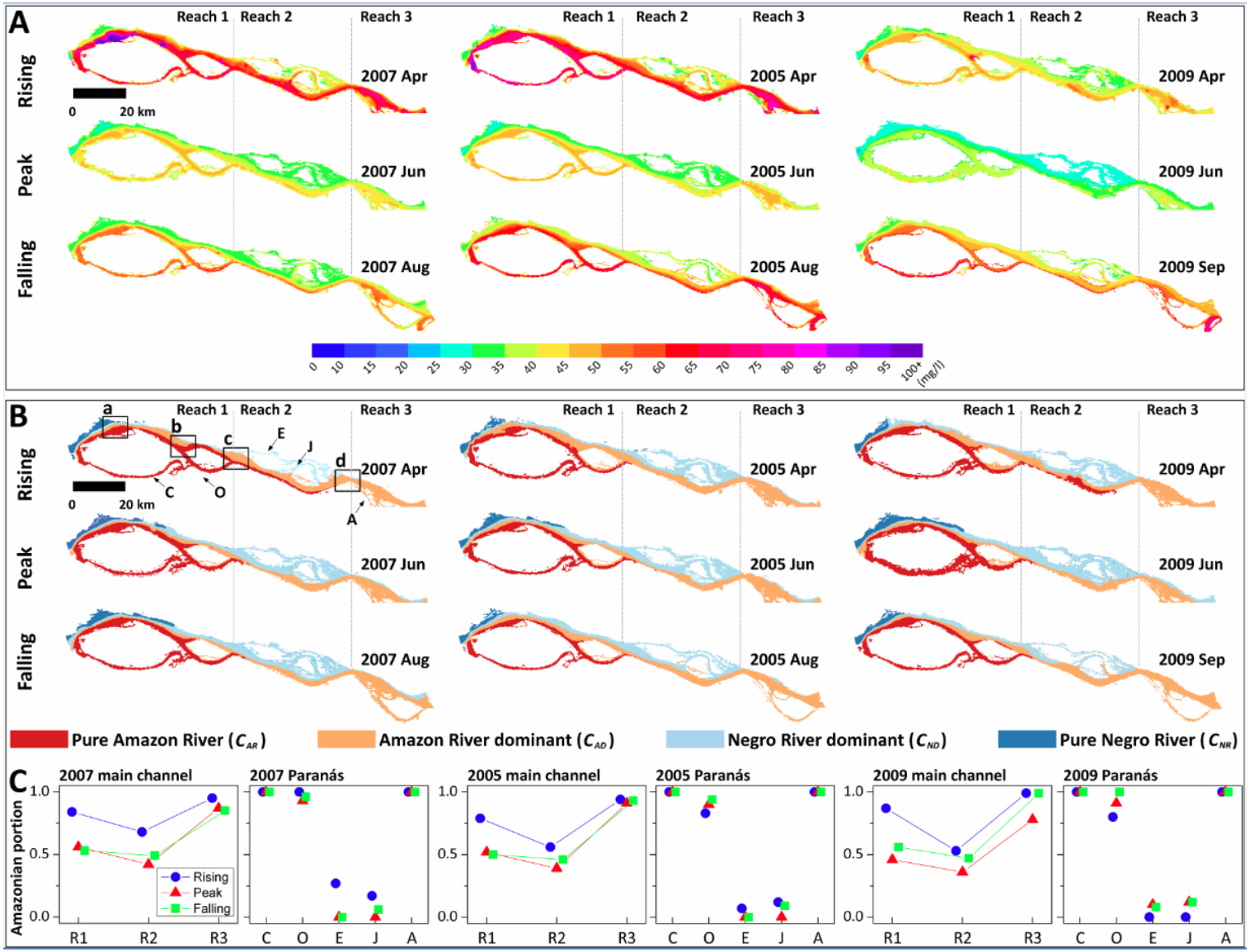
A
Reach 1
Reach 2
Reach 3
Rising
Peak
Falling
2007 Apr
2007 Jun
2007 Aug
2005 Apr
2005 Jun
2005 Aug
2009 Apr
2009 Jun
2009 Sep
0
20 km
0 10 15 20 25 30 35 40 45 50 55 60 65 70 75 80 85 90 95 100+ (mg/l)
B
a
b
c
d
E
J
C
O
A
Pure Amazon River (C_{AR})
Amazon River dominant (C_{AD})
Negro River dominant (C_{ND})
Pure Negro River (C_{NR})
C
2007 main channel
2007 Paranás
2005 main channel
2005 Paranás
2009 main channel
2009 Paranás
Amazonian portion
1.0
0.5
0.0
Rising
Peak
Falling
R1
R2
R3
C
O
E
J
A

Figure 2.6. A: Surface sediment concentration maps in different seasons and years derived from published calibration model in the Amazon River by Park and Latrubesse (2014). The contrast between the muddy Amazon River and the black water of the Negro River is evident. Although additional information is required to quantify the surface sediment load of the Negro River, qualitative comparisons between the white and black water are allowed. B: Surface water type classification maps into four classes (C_{AR}, C_{AD}, C_{ND}, and C_{NR}). Four black windows in the 2007 Q_{rising} image (a, b, c, and d) indicate the locations where more detailed analysis with bathymetry is provided in Figure 2.07. C: Spatiotemporal variability of Amazonian surface water portion. X-axis abbreviations: R1=Reach 1, R2=Reach 2, R3=Reach 3, C=Careiro, O=Onças, E=Eva, J=Jacare, and A=Autaz-Mirim paranás.

As mentioned above, Amazonian surface water portions are very high in branches along the southern floodplains (i.e. Careiro, Onças, and Autaz-Mirim paranás) and low along the northern floodplains (i.e. Eva and Jacare paranás) without notable inter-annual variations.

Unlike the bed scour observed in large braided rivers confluence, where it can be developed on a sandy bed and can be over five times deeper than the mean channel depth (Best and Ashworth 1997b), the thalweg in the Amazon-Negro River confluence is deeper and more stable because it is incised in bed rocks. The impressive depth observed in the lower Negro (Latrubesse and Franzinelli 2005) seems to be a feature developed over the long term, as the Negro hydraulic power is currently very limited to build a scour at the confluence because of the backwater effect produced by the Amazon River (Meade et al. 1991). At the confluence, the hydraulic competence of the Amazon is much higher in relation to the Negro as, the mean water velocity of the Amazon River is twice as fast as that of the Negro River (Figure 2.8) (Filizola et al. 2009). Downstream from the

confluence, the bathymetry of the main channel is highly asymmetric. For example, in a single cross-section, the depth can range from 10 m near the left bank to approximately 60 m at the right bank (Figure 2.7c). Asymmetric bathymetry is developed by the interactions between the Amazon and Negro rivers and also by local geologic controls (the curvature of the Amazon), due to the blocking effect of the Careiro Island and the atrophy of the Careiro Paraná, which concentrates the Amazon flow toward the north (Figure 2.1C). On the other hand, flux of the Amazon waters through the Careiro Parana perhaps is also favoring the relatively high bifurcation angle and the Amazon River's local sinuosity. This kind of relation was proposed for a highly sinuous anabranching reaches in the upstream Peruvian Amazon (Frias et al. 2015). However, the Careiro Parana's lateral migration rates were lower than the branches in the upper Peruvian Amazon described by Frias et al. (2015), and despite the width of branch is large (about 30% of the width of the Amazon main channel), it only transports 6-12 % of the discharge transported by the main channel.

Immediately downstream of the confluence (Reach 1), the Negro and Amazon waters flow on the main channel, through an asymmetric cross-section. The spatial limitation to accommodate both large volumes of waters and the different hydrophysical characteristics of the water types makes the turbulent flow of the Amazon River dominant in the deeper zone and the right side of the main channel, compressing the buoyant Negro waters toward the left bank to form a black water corridor. Comparing surface water distribution patterns and the location of thalweg in Reach 1, the buoyancy effects of the Negro waters over the Amazon can be observed throughout different

seasons (Figure 2.7a and b). In Figure 2.06b, the thalweg is adjoined to the left bank of the channel and, simultaneously, the top of the thalweg (surface) is occupied predominantly by the black waters, especially during Q_{peak} and $Q_{falling}$. This buoyancy effect was also observed during our field survey. According to our ADCP data collected at the confluence (at G03B in Figure 2.1), higher surface water temperature of the Negro River due to higher insolation absorption rates can be clearly observed (Figure 2.08). Hence, upon confluence, Amazon River water with relatively lower density slides beneath the Negro water, which can be also observed from the acoustic backscatter distribution patterns. Because acoustic backscatter magnitude has proportional relation with the suspended sediment concentration (hence muddy Amazon River water should have higher backscatter rates). Local variations of the surface water temperature over the Negro water side seem to be due to the upwelling turbulent plumes of the Amazonian muddy water beneath the Negro water. Also due to the back water effect imposed to Negro River (Meade et al. 1991), velocity of the Amazon River is observed to be faster at the confluence.

Thereafter, the buoyancy effect of Negro waters on the thalweg declines and after the Reach 2 is no longer observed. That is, the Negro water dominance observed in Reach 2 is considered to be attributed more to the asymmetric bathymetry of the region (again note the large scour near the right bank that concentrates the muddy waters of the Amazon in Figure 2.7c) than to the buoyancy effect. Until it meets the Madeira River downstream Reach 2, the thalweg runs under the Amazonian dominant water with

different degrees of dominance depending on the season (examples shown in Figure 2.7c and d).

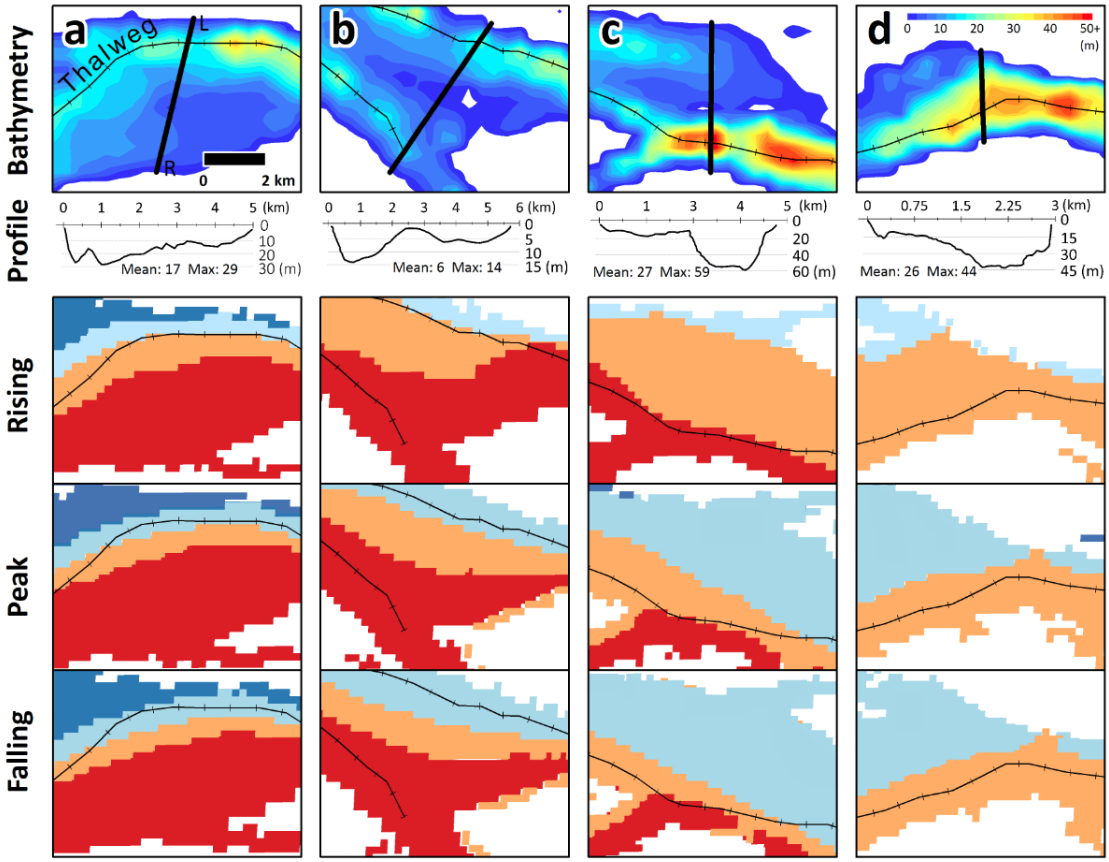

Figure 2.7. Four selected windows (a, b, c, and d) are indicated in Figure 2.06B. Within each magnified window, interpolated bathymetry of the river, cross-section profiles (starting at left bank), and classified surface water types of Q_{rising}, Q_{peak}, and $Q_{falling}$ in 2007 are mapped. All maps are in the same scale.

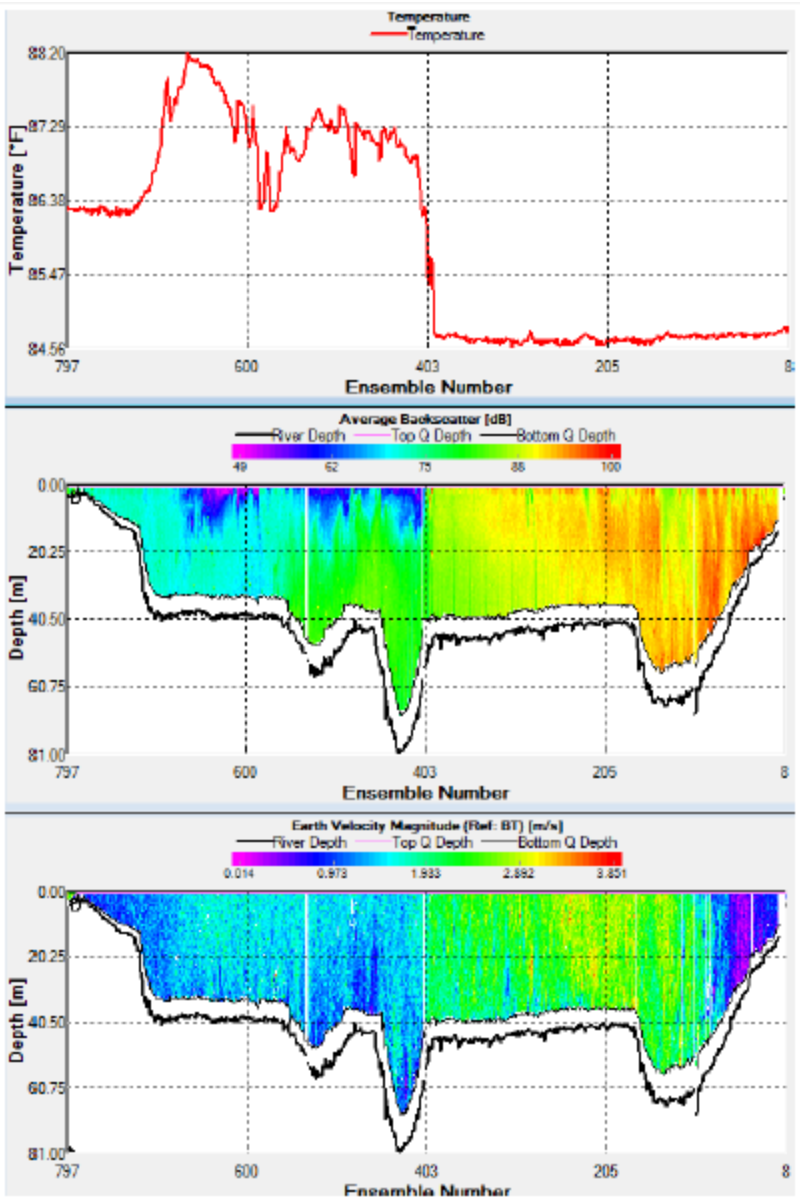

Figure 2.8. ADCP data collected at the Amazon-Negro confluence during the field work on August 28th, 2015. Top: Temperature at the water surface, Middle: Acoustic backscatter data, and Bottom: Flow velocity data. The location is G03B in Figure 2.1.

2.4. IMPLICATIONS BEYOND HYDROGEOMORPHOLOGY

The scope of this chapter can be extended to improve understandings of the distribution of floodplain vegetation and associated ecological patterns as floods are related to nearby surface water distributions in the main channel and paranás (Junk et al. 1989). In the study reach, the contrasting influences of white water flooding (vàrzea) and black water flooding (igapò) to the both margins along the Amazon River probably favor atypical patterns of vegetation and lakes with contrasting water types. For example, entire southern floodplains and islands in Reach 1 are dominantly flooded by muddy water from the Amazon. In contrast, islands in Reach 2 and northern floodplains (including the Preto da Eva River's delta region) are consistently flooded by the water from the Negro River throughout the igapò, which is composed of acidic sandy soils with low sediment and nutrients. This environment has tendency to sustain lower vegetation biodiversity and species richness compared to the forest in terra firme and vàrzea in the Amazon (Koponen et al. 2004). However, the islands in this area were built up by vertical accretion of the muddy sediments of the Amazon. Therefore, we can speculate that this is a very peculiar zone as it could contain mixed vegetation components of igapò and vàrzea forest.

Regarding fauna, also interesting signals appear. The diversity of floodplain birds along the Solimões-Amazon River is estimated to be at least 169 species, which represents 15% of the whole avifauna of the Amazon Basin and differences in habitat preferences of bird species between igapò and vàrzea have been acknowledged (Remsen

Jr and Parker III 1983). The Solimões-Amazon and Negro rivers confluence seems to mark a change in the endemism zones of the floodplain birds and forest composition, acting as a fluvial corridor (Cohn-Haft et al. 1997). The surface water distribution patterns also have important effects on the fish species distributions as well. For example, an analysis of 139 fish species habitats in Central Amazon floodplains showed a significant influence of the vegetation cover associated with the hydrologic interactions with main channel (Petry et al. 2003).

Considering that the development of contrasting floodplain environments is mainly affected by the surface water distribution patterns of the river, this study in this chapter may potentially play an important role as a resource for the large river floodplain ecologists. Further assessments on the richness, structure, and distribution of vegetation and fauna, which are influenced by hydrogeomorphic characteristics of floodplains, would benefit from our approaches.

2.5. CONCLUSION

Surface water types and sediment distribution patterns are mapped downstream from the confluence of the Solimões-Amazon and Negro rivers in three different years: average hydrological condition (2007) and two years when extreme events occurred in the Amazon Basin (drought-2005 and flood-2009). Amazonian surface water domination along the main channel is the highest during Q_{rising} inter-annually. The buoyancy effect of the Negro River waters overtopping the muddy waters of the Amazon River is observed

in Reach 1, while the Negro surface water dominates Reach 2. It is also related to the asymmetric bathymetry of the channel in this reach, which concentrates a majority of the water discharge on the southern side in a deeply incised channel (40-60 m). Surface water mixing along the main channel depends on the hydrological seasons with the highest homogenized area observed during Q_{peak} and the lowest during Q_{rising}. Water mixture also depends on the hydrological conditions of the year with the highest rates of water mixing observed in 2009 followed by 2005 and at a minor degree in 2007. For the three investigated years, transversal surface mixings along the main channel were incomplete within our study reach.

Surface water type variability along the branches (paranás) is subjective to the anabranching style. Surface water type variability was low in the branches when compared to the main channel which displays more water mixing activity. The southern branches keep the water type identical during the whole year and are dominated by muddy waters (i.e. Careiro, Onças, and Autaz-Mirim paranás). The Eva and Jacare, black water dominated branches, however are affected by the Amazon River muddy inflows only during Q_{rising}. Inter-annual variations in the surface water distribution patterns were not observed both along the main channel and paranás. Since our model has been simulated in different years with extreme events, we believe that the dominant mixing patterns observed in this study have been persistent over a decadal scale.

The understanding of these patterns is relevant not only for hydrogeomorphology, but also for floodplain ecology. Considering that large rivers generally follow an anabranching channel pattern, the proposed approach can be applied to a variety of

morphodynamics and environmental studies in confluences of large rivers around the world.

Chapter 3: Hydrological Connectivity in the Amazon River Floodplain Assessed From Remote Sensing and Field Control[2]

3.1. INTRODUCTION

The largest axial alluvial rivers on the planet in water discharge are anabranching fluvial systems that contain the longest and widest floodplains (Latrubesse 2008, 2015). In this context, the Amazon River could be considered a superlative case where massive volume of water and sediment are seasonally exchanged during the complex channel floodplain interactions (e.g. Alsdorf et al. 2010; Dunne et al. 1998a; Richey et al. 1989; Wilson et al. 2007). Through channelized flow and overbank diffusion processes (Mertes et al. 1995b), a complex maze of interconnected network of lakes, channels, and swales over vast floodplains experience spatiotemporally heterogeneous patterns of inundations (Alsdorf 2003). However, this mechanism of flood routing, which depends on floodplain geomorphology, still remains poorly understood in the Amazon. Only existing works on large river floodplain hydrology accounting for the differences in floodplain geomorphology were in Mississippi River (e.g. Hudson and Colditz 2003; Hudson et al. 2012), which is a meandering fluvial system. However most of the large rivers on Earth

[2] This chapter contains a previously published material from:
Park, E., & Latrubesse, E. M. (2017). The hydrogeomorphologic complexity of the Amazon River floodplain and hydrological connectivity assessed from remote sensing and field control. *Remote Sensing of Environment, 198*, 321-332. Edward Park conceived the research idea, collected data, developed methodology, analyzed results and wrote initial version of the manuscript with guidance of supervisor Edgardo Latrubesse.

("mega" rivers, mean annual discharge > 17,000 m^3/s) are anabranching system where the processes of floodplain formation are distinct (Latrubesse 2008). Yet, no study has investigated the hydrological connectivity processes by integrating the geomorphic mosaic over floodplain in the Amazon or other large anabranching river systems around the world.

Floodplain construction in the lower Amazon River is related to the evolution of the fluvial system since the last glacial maximum and also to the current functioning of the anabranching channel processes and overbank deposition (Latrubesse and Franzinelli 2002; Mertes et al. 1996a). The importance in considering the morphosedimentary imprints in the floodplain evolution as a basis to understand the current floods and hydrological connectivity patterns is recognized (Latrubesse and Park 2017). However, the extension and distribution of the floodplain area covered by seasonally flooding water along the Amazon River are still to be comprehensively understood from the geomorphic perspective incorporating the floodplain evolutionary history. The floodplain of the Amazon River is not entirely inundated during the typical seasonal floods (Iriondo 1982; Tricart 1977). In the Brazilian territory, for example Mertes et al. (1996a) estimated, based on landform interpretations of Iriondo (1982) that 44,000 km^2 of the floodplains and islands are inundated directly from the Amazon River, while 20,000 km^2 of remaining alluvial deposits may stay dry or recharged locally by ground water interactions, rain fall, or small local tributaries. The floodplain under the influence of river flooding is typically composed of a patch network of large shallow inter-connected round lakes (i.e. impeded lakes, Latrubesse 2012). This water-saturated floodplain is a

representative floodplain style of the lower Amazon River, typically observed downstream of the Madeira River confluence (Hess et al. 2003; Latrubesse 2015). During the passage of the Amazon flood wave, different floodplain landforms experience complex spatiotemporal patterns of inundation depending on their bathymetric and hydraulic characteristics (Alsdorf et al. 2007). Therefore, to understand the underlying flood routing patterns and hydrological connectivity over the floodplain geomorphic mosaic, individual floodplain hydrogeomorphic units (hereafter "geomorphic units" or "unit") should be identified in terms of their own hydrogeomorphic functions.

Traditional in-situ measurements in floodplains, which are restricted mainly by regular access, provide temporary, thus partial information on the hydrological connectivity processes for different geomorphic units. Monitoring the hydrological connectivity necessitates more continuous records of inundation dynamics taking place over the floodplain. In this context, satellite remote sensing offers an efficient tool to overcome these limiting factors because it enables the multi-temporal observations of the hydrogeomorphic processes over the floodplain at a large extent (Mertes and Magadzire 2008a; Park and Latrubesse 2014). Characteristically, optical remote sensing data have been widely used to monitor the water quality in the Amazon floodplain lakes (e.g. Mertes et al. 1993a; Novo et al. 2006), while Synthetic Aperture Radar (SAR) data have been utilized mainly to measure the hydraulic variables in floodplains (e.g. Hess et al. 2003; Jung and Alsdorf 2010). In this chapter, time-series optical remote sensing (MODIS), radar (PALSAR) data, water level data at gauge station, and measurements and observations during the field work conducted on June of 2016 were integrated to

characterize the hydrological connectivity processes in the Amazon floodplain. Specifically, using the Lago Miratuba Floodplain (LMF) along the lower Amazon, seasonal water extent and quality variabilities were mapped, channel-floodplain connection thresholds were identified, and the results were validated using field measurements. LMF is selected because it is a representative area of "incomplete" floodplain in the Amazon that actively responds to the hydrological variability of the river through oscillations of the lake surface area and depth, and by storing water and trapping sediment.

3.2. INCOMPLETE FLOODPLAIN OF THE AMAZON RIVER AND LAGO MIRATUBA FLOODPLAIN (LMF)

The Amazon River, extending over 4,000 km from Peruvian Andes to the Atlantic Ocean along the six million km^2 drainage area, discharges 6,300 km^3 each year to the ocean, an amount which comprises approximately 16 % of the annual global fresh water discharge (Filizola and Guyot 2009). The Amazon River also transports very large amount of sediment load that could range from 600 to 1200 million tons per year (Mt/yr) (e.g. Dunne et al. 1998a; Filizola and Guyot 2004; Meade et al. 1985; Milliman and Meade 1983) and exhibits vast floodplains along its anabranching channel. The floodplain of the Amazon, however presents distinct geomorphic styles from up to downstream reaches (typically from Madeira confluence), due to the lagged geomorphic responses to the Holocene climatic change. Most of the upstream reaches have achieved

equilibrium condition where there remains small or no available space for further sedimentations. In contrast, valleys and sedimentary basins/sinks along downstream reaches are partially filled up and thus have not yet reached the quasi-equilibrium conditions. The lower Amazon valley, upstream the estuary, is a geomorphologically "incomplete" floodplain, which have not had enough time and sediment inputs to attain the equilibrium stage since the last deglaciation (Latrubesse 2015).

During this progressive dynamic equilibrium stage, the Amazon River experiences continuous exchange of water and sediment with floodplains, which are estimated to be 235 km^3/yr (Alsdorf et al. 2010) and 500 Mt/yr net transport to floodplains (Dunne et al. 1998a), respectively. This indicates the significant role of the floodplains both as active water storage and sedimentary sinks. These floodplains are morphologically complex, composed of mosaic of different alluvial architectures and depositional environments with diversity in their origins, shapes, and functioning (Latrubesse 2012; Mertes et al. 1996a), which are related to the anabranching channel processes (Latrubesse 2008). Floodplain width of the Amazon generally becomes larger downstream, and the widest and the most critical sedimentary sinks are located at lower section of the river, in between the confluence with the Madeira River and Obidos (Bourgoin et al. 2007). Lago Miratuba Floodplain (LMF) is located immediately downstream the confluence with the Madeira River, the largest tributary of the Amazon that delivers nearly 50% of the sediment load carried by the Amazon River (Filizola and Guyot 2009; Meade 1994). The LMF is delimited to the north by the Amazon River, west by the Madeira River, and south/east by uplands (Solimões Formation) with its total area

around 1,100 km^2 (Figure 3.1). Hydrology of the LMF is under the influence of both the Amazon and Madeira Rivers. We select LMF as a representative incomplete floodplain in the lower Amazon where the lake surface area seasonally oscillates in phase with water level changes in the main channel.

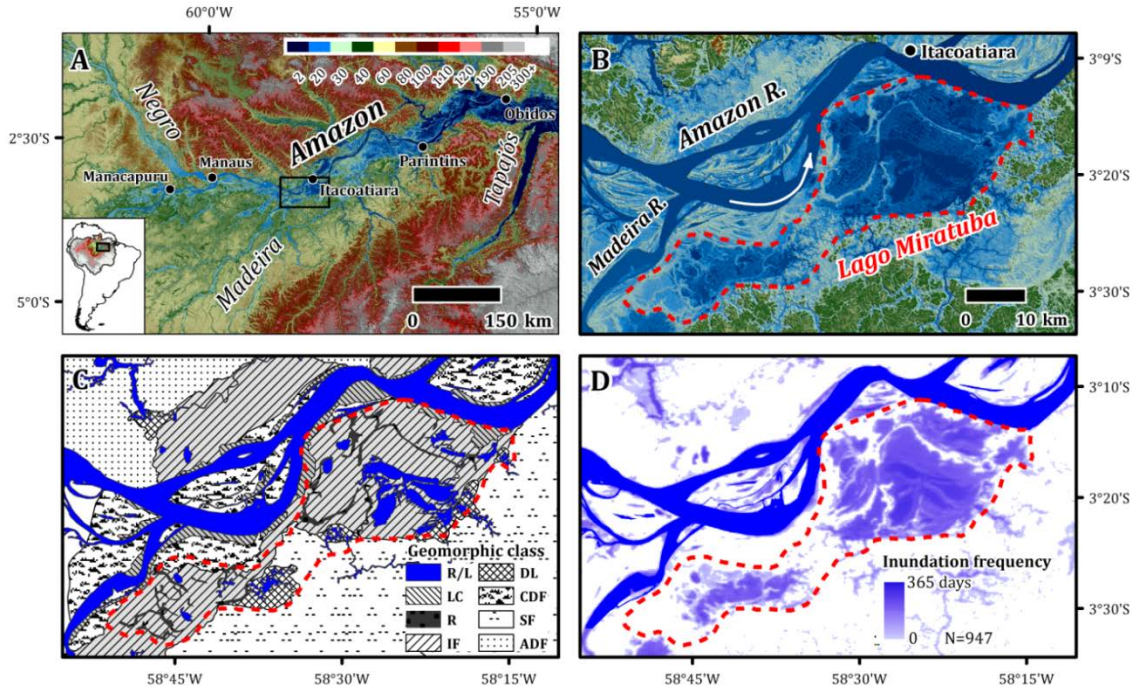

Figure 3.1. A: Small scale map of the Amazon River (Manacapuru-Obidos) with major tributaries. Itacoatiara (3°8'34.48"S, 58°25'12.13"W) is labeled where we use hydrometric data in this study, as well as Manacapuru, Manaus, Parintins and Obidos. Background is the SRTM DEM. B: Study area (indicated in A) with Lago Miratuba floodplain extent portrayed in thick red dashed line. The floodplain extent is delineated as the outer boundary of hydrologically inter-connected lakes. C: Geomorphic map of the study area following the classification of Latrubesse (2012): River and Lakes (R/L), Levee Complex (LC), Ridges (R), Impeded Floodplain (IF), Deltaic Lakes (DL), Channel-Dominated Floodplain (CDF), uplands (Solimões Formation-SF and Alter do Chão Formation-ADF). D: Inundation frequency map of Lago Miratuba

generated by averaging 15 years (2001-2014) MODIS 8-day composite time series water masks.

3.3. MATERIALS AND METHODS

3.3.1. Water Level Data At Gauge Station

Daily water level data at Itacoatiara station was obtained from Hydrology and Geodynamics of the Amazon Basin (HYBAM) (Cochonneau et al. 2006). Itacoatiara is the closest station from the LMF where systematic field measurements are available (mean annual discharge at Itacoatiara is $167 \cdot 10^3$ m^3/s, with a drainage area of $4{,}200 \cdot 10^3$ km^2) (Figure 3.1). Mean and variability of daily water level data recorded over eight years (2006-2013) shows a typical hydrologic trend observed along the Amazon River with the distinct water level rising (WL_{rising}), peak (WL_{peak}), falling ($WL_{falling}$), and low (WL_{low}) stages (Figure 3.02A). The highest water levels are observed during early June (≈2240 cm) and the lowest during the late October to November (≈1240 cm), with the annual stage fluctuation around 10 m. To calibrate the seasonal inundation dynamics of the Lago Miratuba we chose the water level data from 2006-2007, an average hydrological year when the Amazon River was free of extreme events.

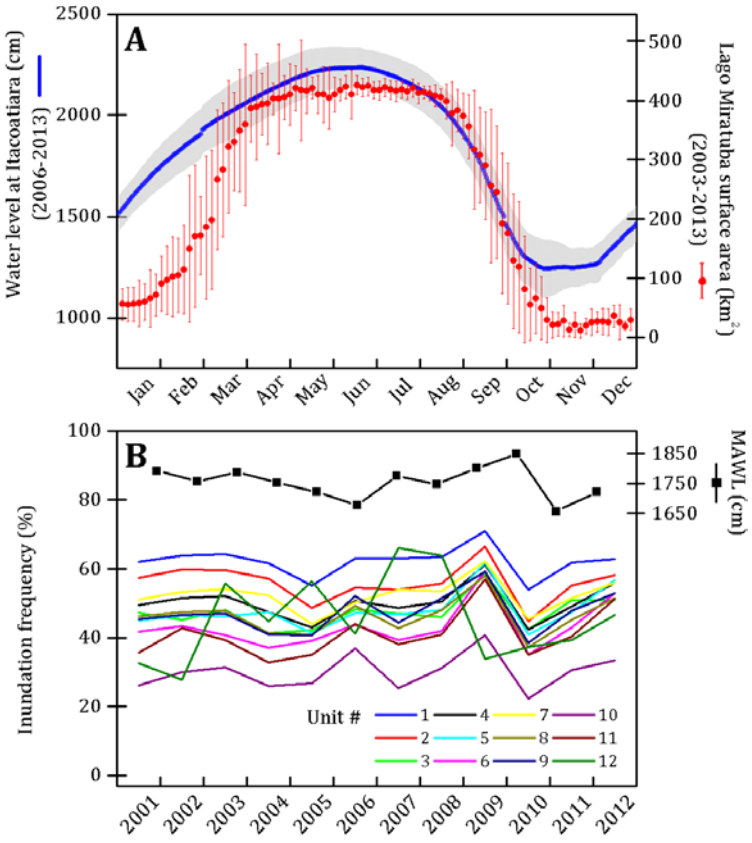

Figure 3.2. A: Mean and standard deviation of daily water level data (2006-2013) measured at Itacoatiara and Lago Miratuba surface extent variability calculated from MODIS time-series data (2001-2014). Daily water level data between 2006-2009 and 2010-2012 were measured with different baseline references. The baseline of 2010-2012 series were corrected by adjusting the mean to 2006-2009 series. B: Inundation frequency (IF) for each unit over calculated from MODIS data (2001-2014) with Mean annual water level (MAWL) at Itacoatiara.

3.3.2. Remote Sensing Data and Pre-processing

In this study, optical remote sensing data (i.e. MOD/MYD09GQ and MOD/MYD09Q1 at 250 m) aided by SAR data were mainly utilized (Table 3.1). MODIS

L2 (and L3) V005 data are acquired for the periods between 2000 and 2014 (15 years). These images are geo-rectified and corrected for the atmospheric effects including aerosols and Rayleigh scattering (Vermote and Vermeulen 1999), and yield surface reflectance at two bands: red (620-670 nm) and near infrared (841-876 nm). We followed further series of image processing steps described in Park and Latrubesse (2014). MOD09A1 product is also used to supply the green band at 500 m.

PALSAR (center frequency at 1.27 GHz, level 1.5) data on board ALOS-1 were supplied from Alaska Satellite Facility (ASF) during the period when the water stages at Itacoatiara were above the mean annual water level (i.e. 1697 cm) during the 2006-2007. We used ScanSAR mode (at 100 m) which is available at single polarization (HH) and operated with five beams transmission at 14 MHz short burst bandwidth collected during descending orbit (Rosenqvist et al. 2007). ScanSAR mode have been widely used to map the surface water extent in large river floodplains due to its wide swath (~350 km) (e.g. Arnesen et al. 2013). These data are calibrated for incidence angle, and corrected for the radiometric and geometric distortions (Shimada et al. 2009). Image pre-processing including georeferening, backscattering coefficient conversion, and speckle noise filtering were performed following Evans et al. (2010) using MapReady. Two Terrain corrected (RTC) high resolution PALSAR data were also used for geomorphic mapping purpose.

Table 3.1. Remote sensing data used in this study.

MODIS					PALSAR					
Data product	Date	Number of images	Process level	Spatial resolution (m)	Operation Mode	Date (yyyymmdd)	Path/ Frame	Polarization	Spatial resolution (m)/Swath (km)	Water level at Itacoatiara (cm)
MOD/MYD09GQ	2006-2007	730	L2G-V5	250	Fine beam single (RT1)	20080101	7110/73 7120/73	HH	12.5/70	1531
MOD/MYD09Q1	2000-2015	1298	L3-V5	250	Fine beam dual (RT1)	20070710	73/7110	HH+HV	12.5/70	2060
MOD/MYD09A1	2000-2015	703	L3-V5	500	ScanSAR wide beam 1	2006Dec-2007Oct	412/3700-417/3700	HH 5scan	100/350	1766-2152
MODIS image quality control criteria: Cloud cover = clear or assumed clear; Band data acquisition quality = highest; Solar zenith angle (viewing geometry) < 37°.										

3.3.3. Mapping Floodplain Geomorphology

A geomorphic map of the study area was generated, following the classification described in Latrubesse and Franzinelli (2002) and Latrubesse (2012): levee complex,

floodplain ridges, impeded floodplains, deltaic lakes, channel-dominated floodplains, and uplands (Figure 3.1C). Each geomorphic class is digitized mainly based on the interpretation of 1) the two PALSAR RTC products each acquired during the wet and dry seasons, and 2) 30-m resampled SRTM (C-band 5.6 cm) aided by high resolution true color images such as Landsat TM and Google Earth. Then we identified major "geomorphic units" (as defined in Introduction) and flow paths by simulating the lake extent at different river stages both using 1) MODIS time series water extent and surface sediment concentration (SSC) maps (Park and Latrubesse 2014), and 2) Global Mapper flood simulator. These geomorphic mapping results are validated with our field observations on June 28th of 2016. During the field campaign, channel-floodplain connections are verified through careful observations along the entire LMF levee complex.

3.3.4. Delineating Lake Extents

Delineating complete water masks consists of the three steps: 1) Density slicing, 2) calculating Normalized Difference Water Index (NDWI), and 3) Spectral mixture analysis. First, density slicing on NIR band were preferentially used to determine the initial lake water extent. When NIR radiant fluxes are increased due to the rich organic/inorganic matters over the lake surface or to the shallow water columns, NDWI (McFeeters 1996) was substituted for the density slicing method, which is defined as $NDWI = (G - NIR)/(G + NIR)$, where G and NIR refers to green and NIR spectra, respectively. Green band is supplied from MOD09A1 and resampled to 250 m using

bilinear interpolation. After these two steps, it was verified that over 95% of flooded woodlands in LMF, where open tree canopies' crowns not touching each other (FGDC 2008) are classified as water.

Along the 5 km outer buffer of the water extents derived above, MODIS sub-pixel fractions of three classes were estimated: 1) water (w), 2) vegetation (v), and 3) water beneath vegetation canopies (u) using Spectral Mixture Analysis (SMA) (Sippel et al. 1994). Subsequently, selected PALSAR data were reclassified using backscattering coefficients (σ_0 in dB) thresholding (Lee et al. 2014). Within the 5 km buffer zones, flooded herbaceous vegetation that is not masked by MODIS water extents are reclassified as σ_0 < -14 dB, and included in water class. Flooded forests are further separated from non-flooded forests by using σ_0 = -6.5 dB, which is a site-specifically calibrated threshold in the Amazon floodplain (Hess et al. 2003). End-member spectra of flooded vegetation were obtained within MODIS vegetation pixels on close dates (±3 days) with PALSAR those have been delineated as flooded vegetation feature.

SMA calculations to estimate surface fractional area based on selected end-members follow $P_{(bn)} = \sum R_{c(bn)} f_c + \varepsilon$, $\sum f_c = 1$, where $P_{(bn)}$ denoting pixel value of MODIS at band n(n=1 or 2), $R_{c(bn)}$ denoting the mode of end-member reflectance of class c (w,v,u) at band n, f_c and ε referring to the fractional cover for each class within a pixel and the residual term of the mixing model which theoretically fluctuates around zero, respectively. Thus, the final water extents (km^2) were computed as

$\left[count(w) + \sum f_u\right] \times (0.25)^2$, where $count(w)$ denotes number of MODIS water pixels within each geomorphic unit. It was also verified that the flooded area results to that of Hess et al. (2003) during wet and dry seasons.

3.3.5. Decoupling "Local-Recharge" And "River-Recharge" Connection Thresholds

Lake water extents were plotted against the water level data measured at Itacoatiara. In these plots, "*local recharge*" thresholds are identified as an inflecting moment of water level in the river, when water extent start to deviate from zero during WL_{rising}. Because in the Amazon floodplains, seasonal precipitations (clear water) and local runoffs (black water dominant) typically recharge floodplain lakes prior to the connections from the main channel (Mertes 1997). We further performed regression analysis between the water level and inundation extents for each unit, to see the level of river hydrology's influence on the floodplain lake extent variability. "*River-recharge*" connection thresholds are identified thereafter, by detecting high sediment laden water entering into the floodplain lakes where black and clear water types are already present (Mertes 2000; Pavelsky and Smith 2009). Here, time series median-maximum SSC values were plotted observed in each geomorphic units and determined *river-floodplain* connection thresholds (as main channel water level) when the maximum SSC start to soar and are maintained at a higher level.

Chlorophyll-*a* concentration (Chl-*a*) maps were generated for the 2006-2007 hydrological year (Carder et al. 2003). Previous studies have shown that Chl-*a* could be efficiently estimated using the MODIS ocean color algorithms for single large lakes

(typically >100 km^2, case II water) throughout the globe (e.g. Chavula et al. 2009; Pavelsky and Smith 2009; Sayers et al. 2015; Wu et al. 2009). Increase in the phytoplankton density over the water surface could mask the reflectance sensitivity to SSC (Martinez et al. 2003; Restrepo et al. 2016) and it has been reported that this effect may become significant when Chl-*a* >30 mg/m^3 (Dogliotti et al. 2015). Therefore, pixels with Chl-*a* $\geq$ 30 mg/m^3 were masked and replaced with the closest unaffected pixels.

Note the two different threshold terms used in this chapter: *local recharge* (when lakes receive non-sediment laden water before the connection with river) and *river-floodplain* connection (when lakes start to receive muddy/white water from the river) thresholds. *Disconnection* thresholds during $WL_{falling}$ are also identified separately due to the hysteresis between flooded area and water level, as the water extents converge back to zero.

3.3.6. Validating River Connectivity Thresholds in The Field

Identified remote sensing-driven channel-floodplain connectivity water level is validated by matching to the bed elevation of the floodplain channels connecting LMF during the field survey on June 28th of 2016. Floodplain channel depths (at nadir and sidescan images) and flow velocity of initially flooded unit (i.e. unit1) were measured using Side-imaging device (Humminbird 899ci HD, at 200 kHz bean mode) and Acoustic Doppler Current Profiler (ADCP, Teledyne Rio Grande 1200 kHz), respectively. Since the floodplain channel bed was relatively flat, we also present the ADCP data collected longitudinally along the channel to show the flow structure. Velocity Mapping Toolbox

(Parsons et al. 2013) was used to process depth-averaged velocity to visualize the flow directions and transverse profile to assess the velocity, which adjust the bed slope in the floodplain channel.

3.3.7. Incorporating Overbank Diffusion Processes

Overbank diffusion, which happens after the channelized flow, cannot be monitored using the identical approach due to the presence of turbid water in floodplain lakes. Unlike channelized flows (i.e. "flow pulse" in Tockner et al. 2000), overbank process is mainly controlled by the bank height along the river. Therefore, information on bank height continuously extracted from DEM along the LMF levee, integrated with our field observations provide clues on the location and timing of overbank diffusion processes (e.g. Hudson et al. 2013). Vegetation removed SRTM DEM at 90-m (O'Loughlin et al. 2016) was used to extract bank elevations at every 90 m interval longitudinally along the LMF. Elevation at river surface is calibrated with water level data collected at Itacoatiara station on February 16th of 2000 (i.e. 1688 cm on the same day of SRTM operation). We also provide pictures taken in the field work on June 28th of 2016 showing the different inundation conditions along the levee complex.

3.4. Results And Discussion

3.4.1. Floodplain Hydro-geomorphology And Units

The lower Amazon River exhibits an anabranching channel patterns (Latrubesse 2008), which is characterized by a low gradient (≈2 cm/km) and stream power (6-12

W/m^2), straight channels belt (sinuosity≈1.07) and dominant in suspended load (Filizola and Guyot 2009). Heavily vegetated levee systems along the channel banks and islands in this region built mostly by the vertical accretion of fine sediments are stable (Rozo et al. 2012). Along the LMF, the levee complex is huge approximately 80 km in longitudinal length with up to 4 km in its width (Figure 3.1C), enough to endure the incoming southeast ward Amazon River flow from extensive bank erosion to maintain the steep channel curvature (arrow in Figure 3.1B). Along some part of this cohesive levee complex, the channel dominated floodplain is episodically formed, which is related to channel lateral shifting over time, and the transference of sediments through spillage processes such as deltaic lateral processes and progradation on floodplain lakes (Latrubesse and Franzinelli 2002; Lewin et al. 2017). At Itacoatiara, the channel becomes narrow due to the local geologic constraints by the Miocene sedimentary rocks (Solimões Formation), but starts to anabranch downstream into two channels.

The LMF is mostly composed of impeded floodplains, where numerous rounded irregular shaped lakes with different sizes and depths are mosaicked on a flat surface. Water levels and extents of the impeded lakes seasonally oscillate according to the hydrologic regimes of the main channel (Figure 3.2). The lakes in LMF are fed mainly by the water from the Madeira River (Abril et al. 2014) through channelized flow or overbank diffusion (Dunne and Aalto 2013a) (Table 3.2). Mortillaro et al. (2011) indicated that a permanent lake in LMF (unit2 in Figure 3.3A) experienced annual depth changes from 4.6 m (low water season) to 10.4 m (high water season) in 2009. Widths of two floodplain channels we measured in the field were 30 m (unit4) and 50 m (unit1

directly connected from river on June 28th of 2016). Although active overbank sedimentation favoring the extensive development of these impeded floodplains, the floodplain is still “incomplete” (Latrubesse 2015) presenting topographic amplitudes mostly with negative features trapping sediments such as rounded or deltaic lakes, and sparsely positive features such as ridges, which are formed by the vertical accretion along floodplain channels those divides individual impeded lakes (ridge heights were lower than levees). Floodplain lakes were defined as a base “geomorphic unit”, which act simultaneously as flow path and as nodal points within the floodplain hydrologic network system, storing water seasonally. Individual lakes are hydrologically interconnected temporally to each other through floodplain channels or breached ridges. Here, 12 individual floodplain geomorphic units were identified within the LMF (Figure 3.3A). Each unit presents different order of inundations (weather flooded directly from the main channel or adjacent units) and hence their water residence times. Identified units are numbered in the order of flooding, i.e. unit1 the first flooded and unit12 the last (Table 3.2).

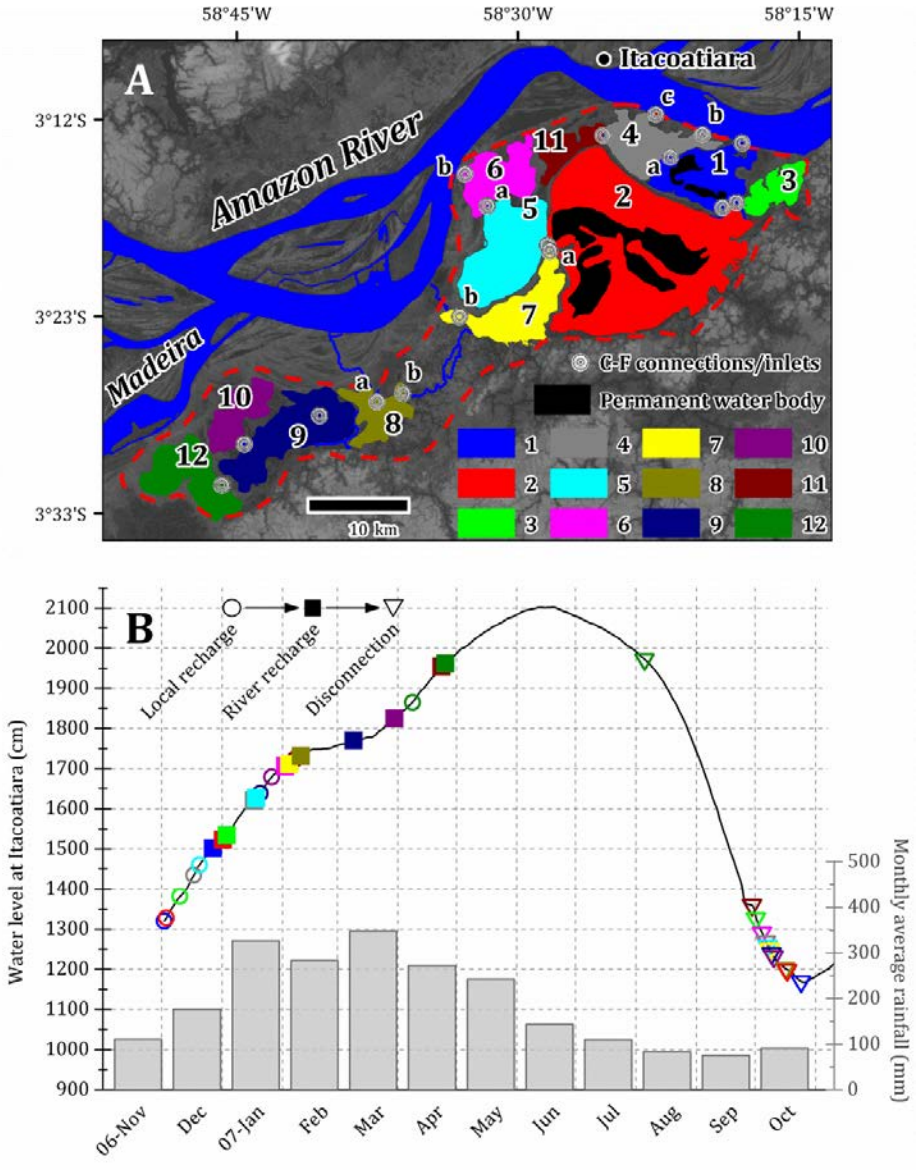

Figure 3.3. A: 12 geomorphic units identified within Lago Miratuba and their inlets (connections to main channel or other units). Units are numbered in the order of flooding. When multiple connecting inlets exist for a unit, then the first connecting inlet is used as a threshold ("a"), however "b" and "c" are still identified when available from remote sensing data. B: Floodplain lake *local-recharge* (○), *river-recharge* (■), and *disconnection* (▽) thresholds for each unit plotted along the hydrograph (2006-2007) and monthly average rainfall data (2000-2012 period from worldweatheronline.com).

3.4.2. Lake Extent Variability And Local-Recharge Thresholds

Vegetation cover in LMF is mainly forest and woodland (Sobrinho et al. 2015). Since the dense vegetation cover and trapped debris interrupt the channelized flows over floodplain at various degrees, it is difficult to calculate the flow rates in the floodplain channels (Alsdorf 2003). Moreover, estimating the morphometric parameters of the network of floodplain channels from currently available remote sensing data is limited due to the small size of the channels. Other diffusive flows, moving laterally at a slow speed over extensive floodplain (Mertes 1997) are also very susceptible to the heterogeneously distributed vegetation, which affects regional hydraulics (i.e. Manning's roughness 0.1-0.14 in the Amazon floodplain) (Rudorff et al. 2014a). In this sense, it is considered that observation-based approach, such as using multi-temporal remote sensing data with field-validations, is more efficient in mapping seasonal hydrological processes over this morphologically complex terrain, rather than traditional process-based modeling focusing on directional flow sources from the river (e.g. Bourgoin et al. 2007; Rudorff et al. 2014b).

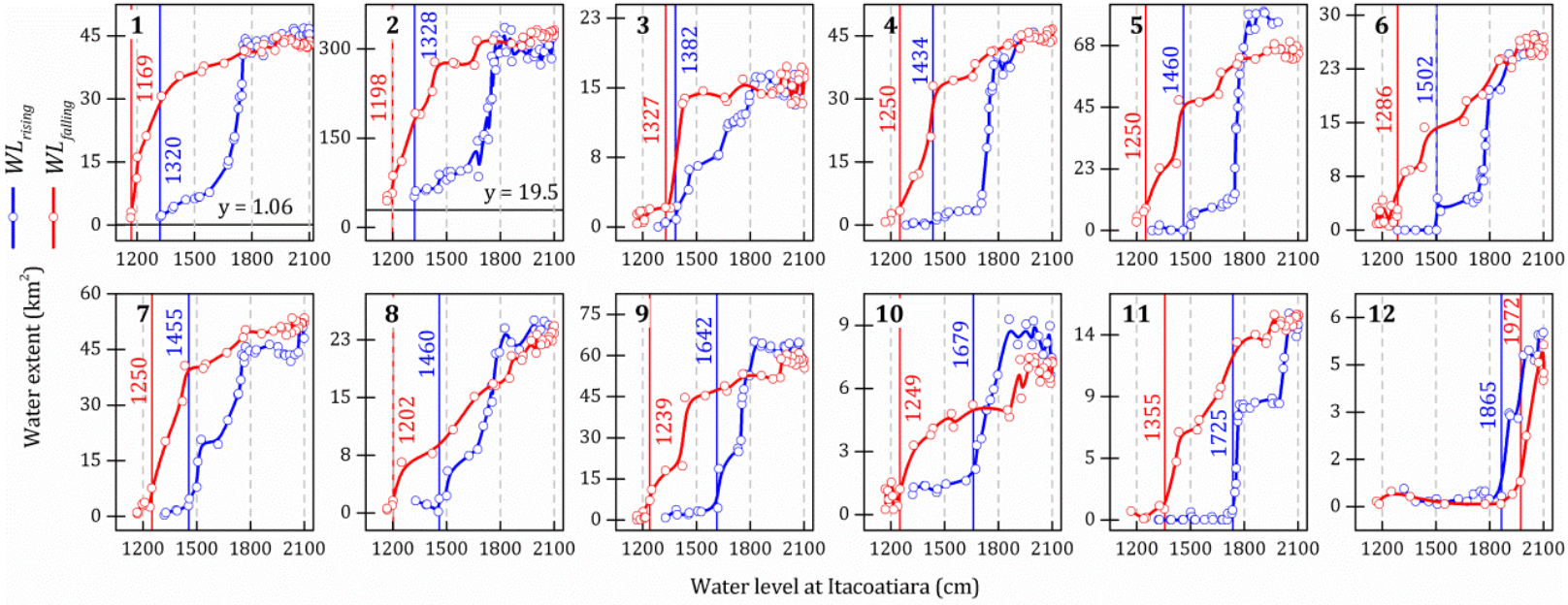
WL_{rising}
$WL_{falling}$
Water extent (km²)
Water level at Itacoatiara (cm)
1
1169
1320
y = 1.06
2
1198
1328
y = 19.5
3
1327
1382
4
1250
1434
5
1250
1460
6
1286
1502
7
1250
1455
8
1202
1460
9
1239
1642
10
1249
1679
11
1355
1725
12
1865
1972

Figure 3.4. Counter-clockwise hysteresis of water extent (flooded area) at different water level at Itacoatiara (2006-2007 hydrological cycle) for 12 identified geomorphic units (lakes) used in this study (black bold numbers in each plot indicate unit #). Blue and red curves indicate water extents changes during WL_{rising} and $WL_{falling}$, respectively. Blue and red vertical lines represent identified *local-recharge* and *disconnection* thresholds (as water level), respectively.

Time series water extents of 12 individual lakes within LMF over 2006-2007 hydrological cycle were plotted against the water level at Itacoatiara to identify the *local-recharge* thresholds (blue lines in Figure 3.4). Since the unit numbers (unit#) are assigned according to the recharging (inundating) order, water level recharge thresholds increase with the unit number (Table 3.2). Permanent lakes exist only in the unit1 and 2, and lakes in other units are completely dry during the WL_{low}. Only the unit1 and 8 are initially recharged directly from the river through floodplain channels, and other units are recharged through channelized flows from the adjacent lakes. Major inlets where recharge flows enter the lakes are identified and if multiple inlets exist for a single unit, the first connecting inlet is used to identify the threshold ("a" in Figure 3.3A).

The mapped water extent results were comparable to that from Hess et al. (2015)'s dual season wetland classification (Figure 3.5A). During the WL_{Low} and WL_{Peak} the flooded areas were 369 and 717 km^2 respectively where the water areas from Hess *et al.* (2015) were 389 and 734 km^2 respectively. Flooded forest areas during WL_{Peak} were 83 and 100 km^2 from my and Hess *et al.* (2015)'s results, respectively, which corresponds to 12 and 14% of the total LMF area.

Recently In the Curuai Lake along the lower Amazon, Arnesen et al. (2013) used a logistic regression model to explain the water extent variability using the water level data on floodplain. Nonlinear regression models separately plotted during the rising (logistic) and falling (polynomial) phases for each unit (each unit N>350) are presented in Figure 3.05B. Average R^2 values for the entire units were 0.83 and 0.76 for WL_{rising} and $WL_{falling}$, respectively, indicating that water extent dynamics in floodplain are highly dependent on the main channel water level. Interestingly, the decreasing trends of R^2 for both the rising and falling phases are evident, when plotted in the order of units (note again that unit# is the order of flooding). This demonstrates that for the lakes those are recharged later, the impacts from the main channel hydrology diminishes gradually.

The hysteresis between water level and water extent in different seasons in the Amazon (as seen in Figure 3.4) has been mentioned in Rudorff et al. (2014a). This hysteresis results in discrepancies in the lake *local-recharge* and *disconnection* thresholds, which makes it difficult to predict the water residence time in floodplain when the recharge threshold is calibrated only during the WL_{rising}. In general, the water extents changes gently during the early stages of WL_{rising} and early $WL_{falling}$. In WL_{rising}, water extent starts to increase at certain *WL* thresholds, when the waters from the local sources or rain fall start to contribute to the units. Once maximum water extent is reached during WL_{rising} for all units around 1800 cm, only except for unit6, 11, and 12 (Table 3.2), water extents stop expanding until the river stage rises to its peak (~2150 cm) (Figure 3.04). This indicates that water extent is not any more sensitive to the changes in the river stage when the maximum water extent in floodplain is reached. However, water volume in the

floodplain is still increasing during this period, as the water from the main channel is continuously being imported, especially at even higher magnitude after the initiation of overbank flooding. In short, even before the bankfull stage in river (i.e. river stage when it starts to overflow), water extent in floodplain is already saturated and fully covered by water. However from this stage, water level still increases more than 3 m without changing water extent. This can be explained by the hydraulic geometry of floodplain, which the levee/ridges confining the lakes are steep. Depth-averaged velocity vectors processed from ADCP data collected on June 28th of 2016 along the floodplain channel connecting river to unit1 also shows that the inflow of the water from the river is still occurring, even after reaching the maximum water extent (water saturated condition) in floodplain (Figure 3.5D). Another factor possibly facilitating this hysteresis is the dense vegetation on the floodplain. Particularly, during the early stage of WL_{rising} when the depth of floodplain channel is still shallow, inflow hydraulics is greatly obstructed due to the relatively higher shear stress induced by vegetation.

Lake areas were not highly dependent on the inundation order (Figure 3.5C and Table 3.2), however were negatively correlated with the water travel distance from the main channel. In Figure 3.5C, we separately plotted two groups (red and green) based on the main channel flooding sources. Unit2 is recharged from unit1 which directly receives water from the main channel. Then up to the unit7 is sequentially recharged from the previously ordered lakes (red). Direct channelized flow from the main channel recharges the unit8, then it again successively feeds up to unit12 (green). In addition to the previous observations in the Amazon floodplain that lakes with longer water travel path

experiences smaller water level fluctuation (Alsdorf 2003) and least water storage changing rates (Alsdorf et al. 2005), our observation indicates that longer water travel path results in smaller lake extent variability.

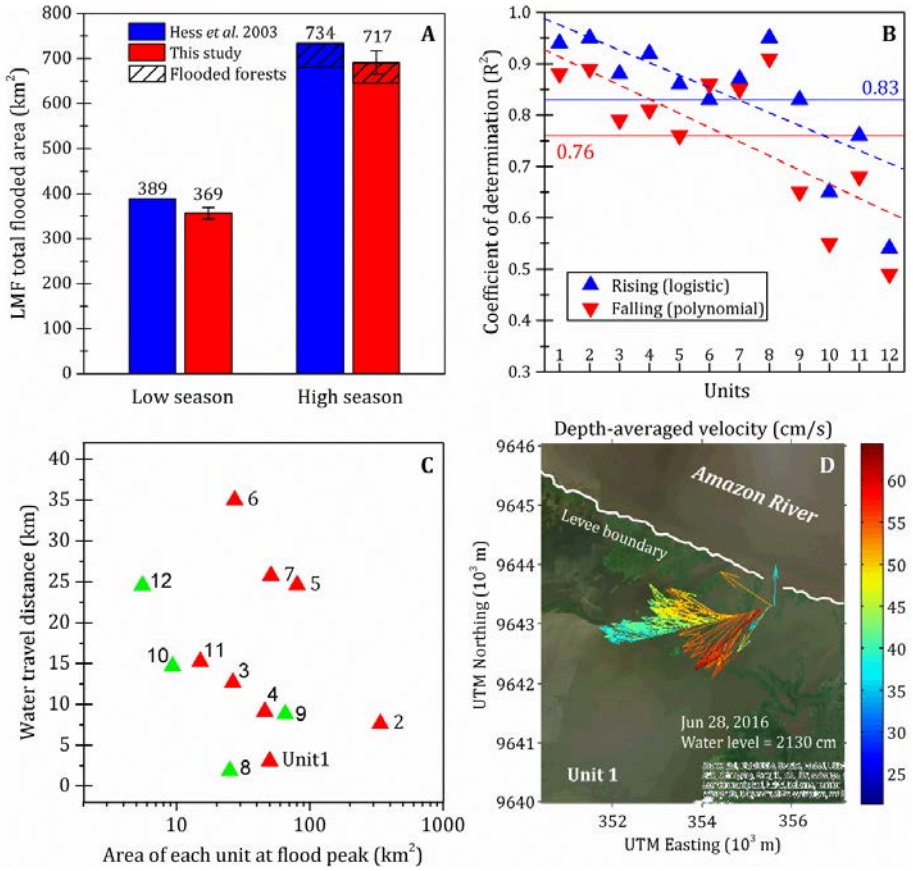

Figure 3.5. A: Comparison of total flooded area with results from Hess et al. (2003)'s dual season (Sept-Oct 1995 and May-June 1996). Two dates during the low and high seasons were chosen, when the water levels were similar to Hess et al. (2003)'s dual season (i.e. 1850±70 and 550±70 cm at Manacapuru corresponding to 2200±60 and 1225±60 cm at Itacoatiara, respectively). Whiskers indicate 2 σ (13 and 26 km^2 for low and high seasons, respectively) of the water extents. B: Decreasing trend of R^2 fitted logistic (rising) and polynomial (falling) models between water level and floodplain water extent, when plotted against units, i.e. in the order of flooding (each unit N≈350). R^2 for the logistic regression is pseudo-R^2. Horizontal lines indicate average R^2 of each stage. C: Water travel distance of each lake plotted as a function of lake areas at flood peak. D: Depth-averaged velocity vectors processed from ADCP data collected on June 28th, 2016 in the floodplain channel connecting river to unit 1. This shows that the inflow of the water from the river is still happening, even after reaching the maximum water extent in floodplain.

3.4.3. Controlling the Known Interferences: Sediment Resuspension and Algae Bloom

During the early WL_{rising} season (December - early February), clear and black waters normally start contributing to the floodplain lakes prior to the recharge from the main channel (Mertes 1997). In this period, the monthly average SSC in the Amazon River at our study area reach the highest values during the year (i.e. 150-180 mg/l). Therefore tracing the high sediment laden plumes in the floodplain lakes with daily temporal resolution MODIS data is an efficient way to detect the channel-floodplain connecting moments (Pavelsky and Smith 2009). In this process, the two following issues were controlled: 1) resuspension of sediment during WL_{Low}, and 2) possible algae blooming over the lakes.

Sediment settled during the $WL_{falling}$ are extensively resuspended due to the strengthened wind over shallow lakes during WL_{low} season (Barbosa et al. 2010), maintaining high level of SSC without new sediment inputs from the river until the early WL_{rising} (~January) (Bonnet et al. 2008). Time series median (and maximum) SSC in unit2 shows that consistently high median SSC (about 110 mg/l) in the lake is maintained until the early-January through resuspension (Figure 3.6). When the lake starts to receive the river input, maximum SSC value soars because as mentioned above, the monthly average SSC in the Amazon River close to LMF during the early WL_{rising} are the highest of the year (i.e. 150-180 mg/l) (Park and Latrubesse 2014). These moments were identified, as when the river inputs reach the lakes. Even after the river connection with the lake in floodplain, fairly similar median SSC values are kept until the end of January

(Figure 3.6). This resuspension issue is considered for the units1-4, which are hydrologically connected before February. Because after February the lakes become deeper and wind speed decreases (Barbosa et al. 2010).

In the Amazon River floodplain, phytoplankton blooms normally occur during the $WL_{falling}$, when the abundant nutrient sources are already delivered to floodplain during WL_{rising} and radiative capacity through the water column is enhanced by reduced turbidity (Novo et al. 2006). However, we observed that, in most of the areas, the maximum Chl-*a* did not reach 30 mg/m^3 during WL_{rising} for each lake. Thus, Chl-*a* effect on the surface reflectance during the WL_{rising} when the river and floodplain lakes are hydrologically connected is disregarded in the analysis. It is observed that Chl-*a* over the lake start to increase in mid-June and reaches the peak in late August-September (i.e. up to 250 mg/m^3) (Figure 3.6).

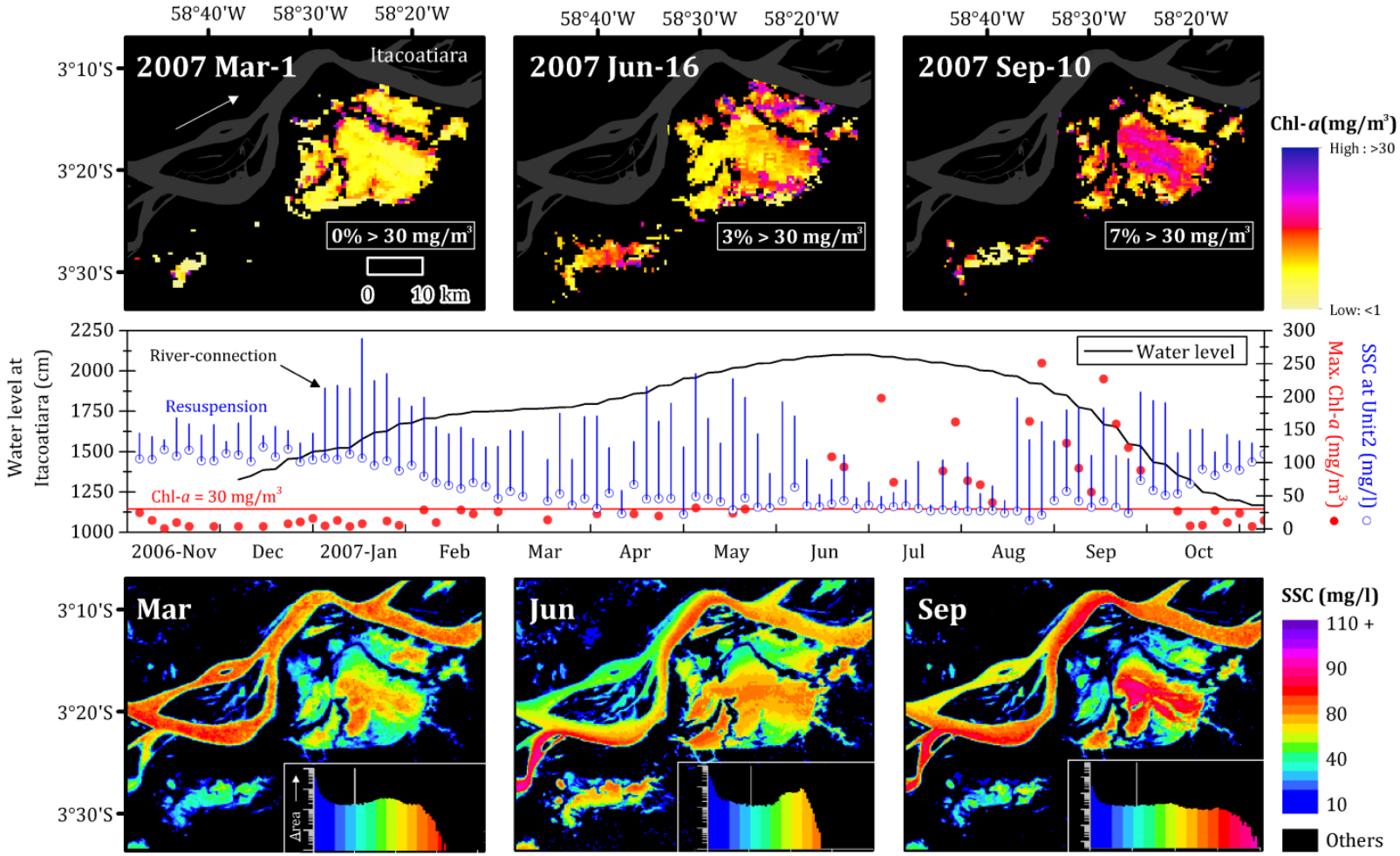
58°40'W
58°30'W
58°20'W
3°10'S
3°20'S
3°30'S
2007 Mar-1
Itacoatiara
0% > 30 mg/m³
0 10 km
2007 Jun-16
3% > 30 mg/m³
2007 Sep-10
7% > 30 mg/m³
Chl-a(mg/m³)
High : >30
Low: <1
Water level at Itacoatiara (cm)
River-connection
Resuspension
Chl-a = 30 mg/m³
Water level
Max. Chl-a (mg/m³)
SSC at Unit2 (mg/l)
2006-Nov
Dec
2007-Jan
Feb
Mar
Apr
May
Jun
Jul
Aug
Sep
Oct
Mar
Jun
Sep
Area
SSC (mg/l)
110 +
90
80
40
10
Others

Figure 3.6. Upper: LMF Chlorophyll-*a* concentration (mg/m^3) images derived from MODIS during different seasons in 2007. Floodplain areas with Chl-*a* less than 30 mg/m^3 were 0, 3, 7% for the water level rising, peak, and falling seasons, respectively. Chl-*a* <1 mg/m^3 were masked out. Middle: Contrasting seasonal dynamics between SSC and Chl-*a* were observed, in that when SSC in LMF is high during the $WL_{falling}$ and WL_{rising}, Chl-*a* tends to be low. However, Chl-*a* start to increase during the WL_{peak} when SSC decreases with water dilution (similar seasonal tendency observed in the lower Amazon by Barbosa et al. (2010). Lower: SSC maps derived from MODIS used to identify the floodplain-channel connectivity thresholds. Note that unlike the channelized flows, river-floodplain connections through overbank diffusion could be observed in the SSC maps (Park and Latrubesse, 2014). Color histograms for LMF are presented for the better understanding of the frequency of pixel values.

3.4.4. River-Floodplain Connectivity and Their Inundation Durations

At the water level of 1502 cm at Itacoatiara, LMF starts to receive the water directly from the river through unit1 (Figure 3.3A). Then until the water level reaches 1710 cm to connect to unit7, all the units2-7 receive the water that comes through the unit1. Unit8 is also directly flooded from the river through a floodplain channel ("a" in Figure 3.3A) and then delivers sediment laden water through unit12. This sequential river recharging thresholds does not have regular intervals (Figure 3.3B), indicating that the connectivity processes for each of units are mainly determined by geomorphic heterogeneity over floodplain. Along the river stage hydrograph (2006-2007), *river-recharge* thresholds (also *local-recharge*) are marked (Figure 3.3B) and thresholds are summarized in Table 3.2.

The sequential hydrological connectivity over 12 geomorphic units varied significantly, as inundations from the river over different units were initiated each at specific river stage thresholds. The *river-recharge* threshold of unit1 was 1502 cm, while unit12 (last connected unit) had that of 1958 cm, indicating that the river stage has to further rise over 4 m to fully hydrologically interconnect the whole floodplain, even after making connection to unit1. Likewise stage durations of connectivity for unit1 and 12 were 73% and 29%, respectively, presenting a great gap (~45%) in their connectivity duration (Figure 3.7A). Thus, we observed huge variability in the temporal continuity of inundation and flood frequency over different units, which depend on the complexity of the floodplain geomorphology.

Understanding this sequential flood pulsing patterns is not only important in regards to geomorphology as they control the heterogeneous sedimentation rates over different floodplain units (Wren et al. 2008), but also critical for floodplain ecology. Because washload (silt and clay) are colloidal particulates mainly absorbing nutrients to sustain broad range of floodplain ecological communities (Tockner et al. 2000). In case of vàrzea in the Amazon, sediment inputs from the river are dominantly silty and clay materials. The grain size analysis of surface sediment samples collected close to WL_{peak} at Itacoatiara, lower Madeira River, and Lago Miratuba also confirmed that surface sediments were composed of 70% silt and 30% clay, on average (Figure 3.7B). Different *disconnections* thresholds happening at a broad range of river stages for different geomorphic units in floodplain were also identified. These hydrological disconnection thresholds are also relevant to understand the effect of “dry” phases when floodplain

ecological communities and their species recruitments experience the maximum stresses (Latrubesse et al. 2013; Neiff 1996).

Geographic locations (proximity with the river) of each unit did not have direct relationship with the order of flooding (Hudson et al. 2012). As a result of physically tracing water travel paths on LMF during WL_{rising}, we observed that this complex mosaic of geomorphic units demonstrated an unexpected circuit of flood routings as seen in Figure 3.3. *River-recharge* connections and floodplain water residence time did not show a clear relationship with the ordinary distance (shortest straight line) from the river (Figure 3.7C). For example, units4 and 6 are proximal to the river, which directly receives water from the river at certain stages through overbank diffusion; however they are connected with river subsequent to the unit2, which is located at even further inner part of the LMF (~7 km further inside from the river).

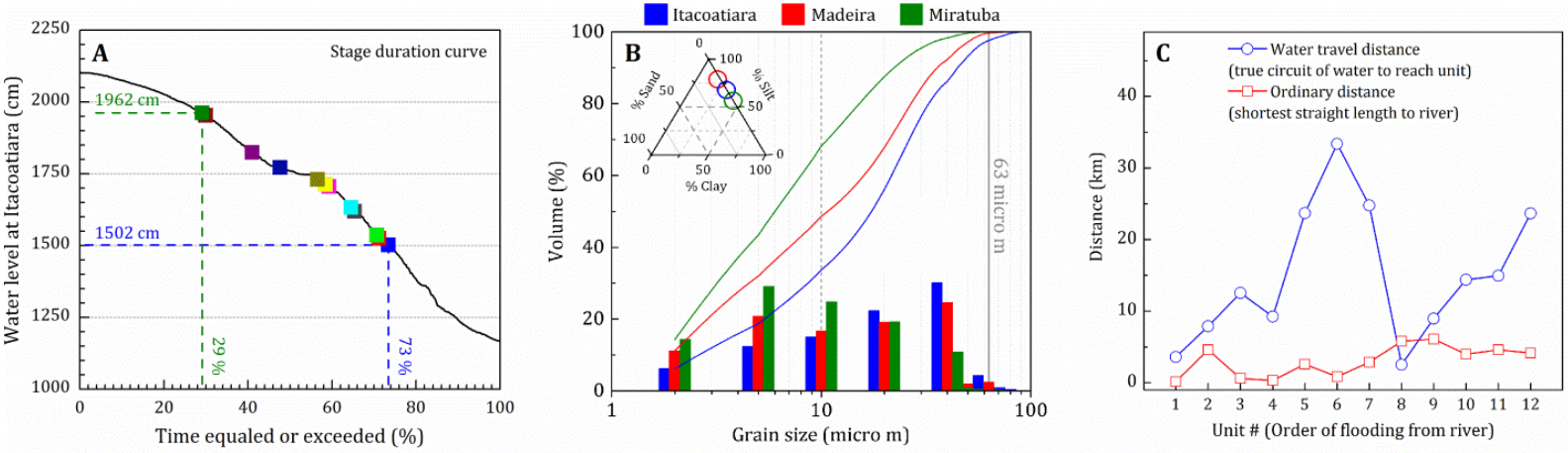
A
Stage duration curve
1962 cm
1502 cm
29 %
73 %
Water level at Itacoatiara (cm)
Time equaled or exceeded (%)
B
Itacoatiara
Madeira
Miratuba
% Sand
% Silt
% Clay
63 micro m
Volume (%)
Grain size (micro m)
C
Water travel distance
(true circuit of water to reach unit)
Ordinary distance
(shortest straight length to river)
Distance (km)
Unit # (Order of flooding from river)

Figure 3.7. A: Stage duration curve showing specific *river-recharge* unit connectivity thresholds. B: Grain size analysis results of surface water samples collected at Itacoatiara, lower Madeira River (immediately upstream the Amazon River confluence), and at Lago Miratuba unit1 in June 2016. C: Water travel distance is measured from main channel to each inlet and ordinary distance is the shortest straight-line distance measured from the river bank to the unit (Figure 3.3A). Note that units are numbered in the order of connections to the river during WL_{rising}.

Table 3.2 Recharge thresholds of geomorphic units.

Unit	Area (km^2) [a]	Threshold water levels at Itacoatiara (cm) *Local recharge - disconnection*	*River-recharge*	Connection process	Maximum extent at	Stage duration (%)
1	49.8 (P)	1320 - 1169	1502	cf-m [b]	1782	73.4
2	335.9 (P)	1328 - 1198	1523	cf-l [c]	1795	71.5
3	26.4	1382 - 1327	1527	cf-l	1805	70.6
4	45.9	1434 - 1250	1620	cf-l	1795	65.4
5	79.9	1460 - 1250	1626	cf-l	1809	64.3
6	27.2	1502 - 1286	1706	cf-l	2007	59.3
7	51	1523 - 1250	1710	cf-l	1804	58.4
8	25.1	1526 - 1202	1731	cf-m	1814	56.2
9	65	1642 - 1239	1770	cf-l	1824	48.2
10	9.3	1679 - 1249	1825	cf-l	1853	40.9
11	15	1725 - 1355	1954	cf-l	2041	29.9
12	5.5	1865 - 1972	1958	cf-l	2017	28.8

[a] at flood peak, P=permanent water body.

[b] channelized flow from the river.

[c] channelized flow from adjacent lake.

3.4.5. Validating River-Floodplain Connectivity Thresholds In The Field

The threshold of initial hydrological connection of LMF with the Amazon River (i.e. connecting unit1) is verified in the field through local geomorphic survey. Average channel width was around 50 m measured from Google Earth (Figure 3.8A red line).

Bathymetry of this channel was quite flat and the depths were around 638 cm on average over the course. We also show two ADCP profiles: one in the floodplain channel (C-1, ~2 km) and the other at the channel delta (C2, ~350 m) (entire survey tracks indicated in Figure 3.08A green line). Water was flowing into the floodplain at low velocities of 27 and 23 cm/s, respectively for C-1 and C-2, which seems to be in favor with the flat bathymetry of the floodplain channel. Since the Sonar transducer fixed at the tethered boat, was 10 cm below the water surface while surveying, the average depth of the floodplain channel is corrected to 648 cm. When this measured floodplain channel depth is subtracted from the water level record of the river on the same day (i.e. 2130 cm on June 28th of 2016), 1482 cm is calculated, which is considered an empirically driven water level threshold required to initiate the water inflow through the floodplain channel. Note that we identified the unit1's *river-recharge* connection threshold as 1502 cm from remote sensing prior to the field work (Table 3.2), which is only 20 cm above the measured threshold from the field. This minor discrepancy may be attributed to the wave conditions in river surface, or small variability in the floodplain channel bathymetry.

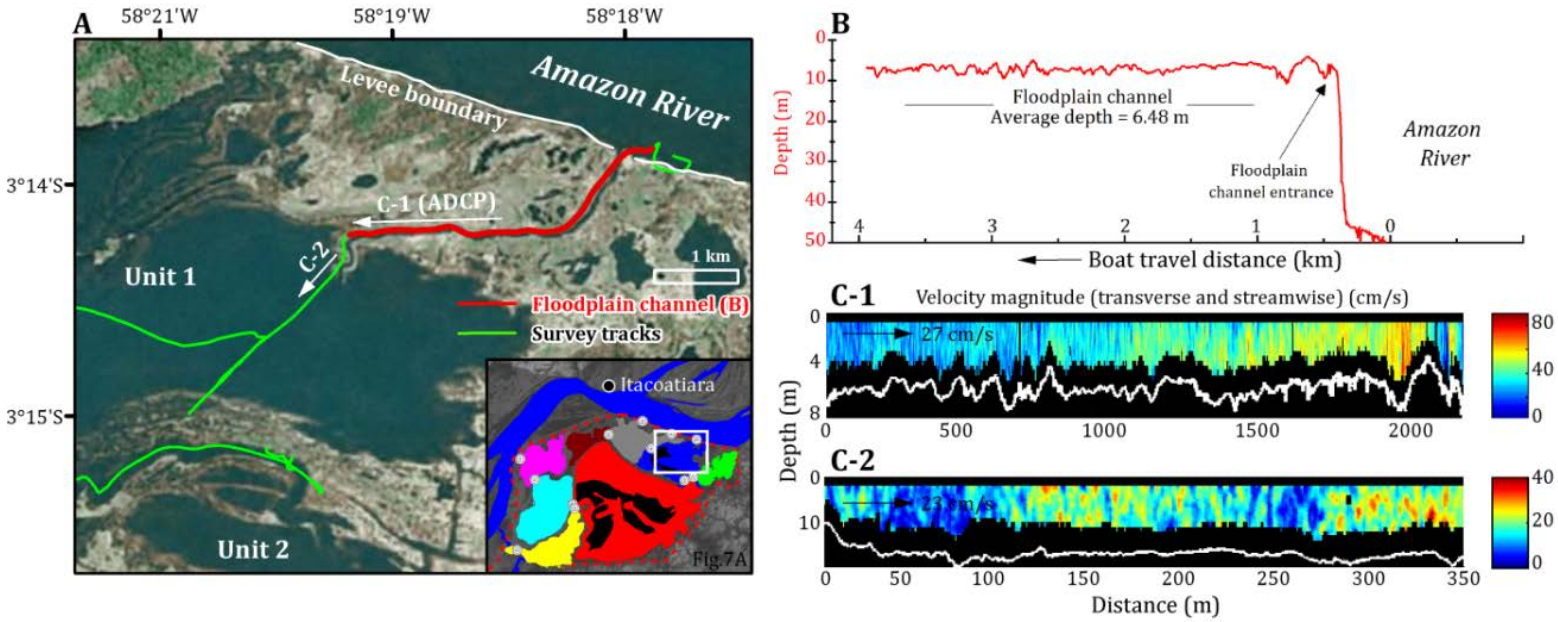
A
58°21'W
58°19'W
58°18'W
3°14'S
3°15'S
Levee boundary
Amazon River
C-1 (ADCP)
C-2
1 km
Unit 1
Unit 2
Floodplain channel (B)
Survey tracks
Itacoatiara
Fig.7A
B
Depth (m)
Floodplain channel
Average depth = 6.48 m
Floodplain
channel entrance
Amazon
River
Boat travel distance (km)
C-1
Velocity magnitude (transverse and streamwise) (cm/s)
27 cm/s
C-2
23 cm/s
Distance (m)

Figure 3.8. A: Our survey tracks in Lago Miratuba Floodplain (LMF) on June 28th of 2016. Average width of this channel is around 50 m and we maintained boat survey track along the channel center line (at every 1 m interval). B: Depth data obtained along the floodplain channel course (Red line in map A and survey direction from Amazon River to unit1). C: ADCP velocity profiles over the major floodplain channel connecting unit1. Survey courses of each profile are shown in map A. Average velocity were 27 and 23 cm/s for C-1 and C-2, respectively.

3.4.6. Decoupling Overbank Diffusion from Channelized Flows

Bank elevation along the LMF (~60 km), which the baseline is calibrated with river stage at Itacoatiara on February 16th of 2000 (i.e. 1688 cm) shows the variability of the bank elevation downstream (Figure 3.9B). In general, bank heights were lower on the northeastern boundary around units2, 3 and 4 (green) than western boundary (blue). Given that the historical maximum water level since 2000 at Itacoatiara did not exceed 2400 cm, it can be assumed that overbank diffusive process is not actively happening along the western boundary (blue in Figure 3.9A and B). Picture a in Figure 3.9 is taken at a bank with lower elevation compared to the surrounding levees, driving downstream close to the right bank of the Amazon River on June 28th of 2016. Although the bank height in this location wasn't measured, the bank seems to be at least 1 m above the river stage through visual inspection, indicating that at least the water level should rise above 2230 cm at Itacoatiara to make the overbank diffusion. Along this western boundary, I could not find field evidences of channelized flows or overbank diffusion, and did not identify channelized landforms. Although we identified a connection with the river along the western boundary using remote sensing prior to the field work (i.e. Figure 3.3A unit6

connection “b”), this connection perhaps has become inactive through sedimentation or vegetation colonization over a short period (~15 years).

River-floodplain connecting point “c” of unit4 (location shown in Figure 3.3A) is shown in Figure 3.9 picture b and c. At the entrance of this connecting point from the river, the bed elevation of the floodplain channel was approximately 1.6 m above the river stage (Figure 3.9 picture b). About 50 m inside this floodplain channel from the river, the channel width became up to 30 m (Figure 3.9 picture c). This floodplain channel was relatively well shaped, flat and perched in relation to the present water level. Although small pond is shown in the picture c, the channel bed was in general dry. We confirmed that unlike normal years, water did not flow this channel in 2016 (personal communication with a local villager). It could also be seen that the bank height of the location where the pictures b and c were taken is slightly above the river stage on the day of field work (Figure 3.9B). At the unit4 river-floodplain connecting point “b” (Figure 3.3A), we verified that the water was still flowing toward the floodplain lake through the flooded forest (vàrzea) (Figure 3.9 picture d). Depth measured at very close to the trees in picture d was 70 cm. Agreeing with my field observations, bank height at this location was a little below the river stage on June 28th of 2016 (Figure 3.9B).

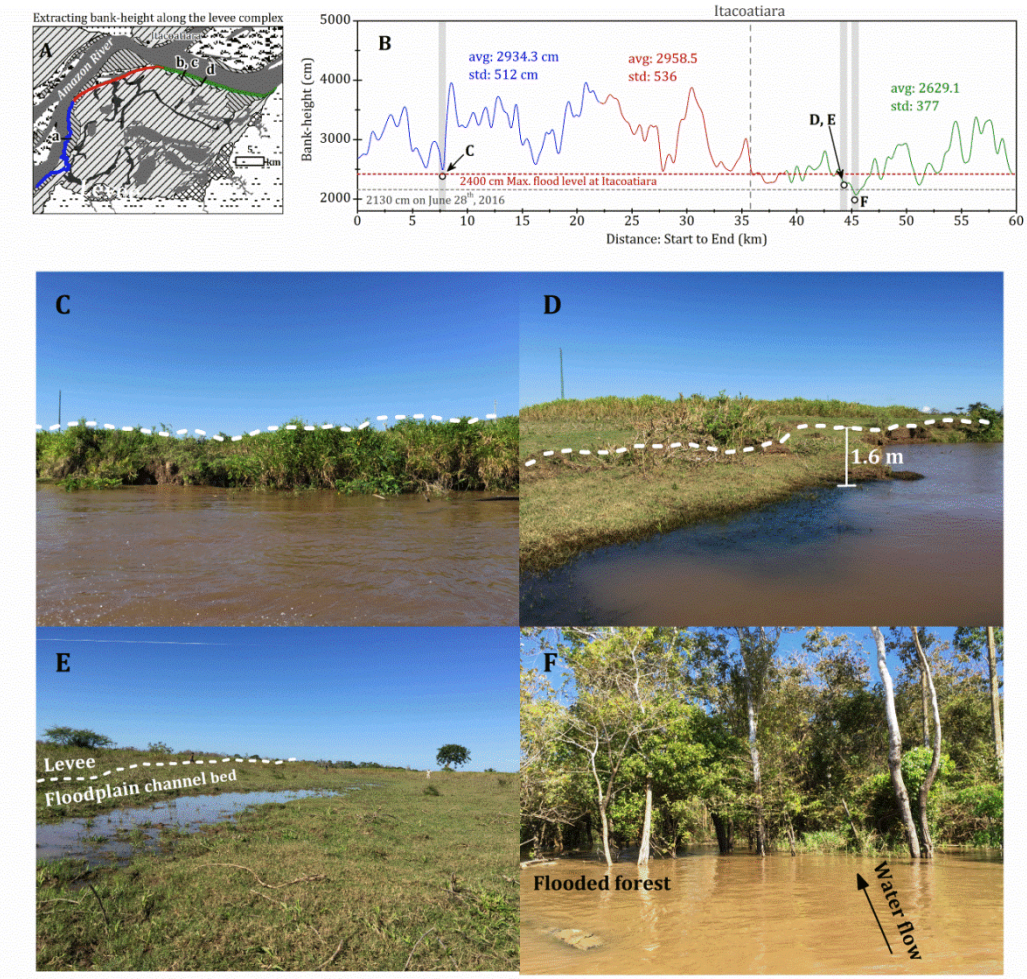

Figure 3.9. A: Levee complex is divided into three reaches (each in different colors). Background is geomorphic map in Figure 3.01C. B: Bank height plotted along the levee distance downstream the river. a-d: Pictures are taken on June 28th 2016 at the locations marked in A and B. Picture a: bank is still more than a meter (visual estimation in the field) above the river stage. Picture b and c: floodplain channel connecting to unit4 (connection point c in Figure 3.03A). Entrance of the floodplain channel from the river (Picture b) and inside the floodplain channel (Picture c, ~50 m inner from river, viewing toward LMF). Picture d: river connection with unit4 through connection point b in Figure 3.03A. Forest on bank is flooded by overbank flows towards the floodplain. Measured depth very close to the flooded forest was approximately 70 cm.

During the field survey along the LMF close to WL_{peak}, river-floodplain connections along the western boundary were not found and overbank diffusion process was observed in the eastern boundary only at a small scale (i.e. Figure 3.9 picture d). Despite the observations of "lack of overbank diffusion", it is considered that overbank diffusion processes are more responsible in water and sediment contributions to floodplain in the Amazon compared to the channelized flows (Table 3.3). For example, based on Dunne et al. (1998a)'s estimations of sedimentation rates in between São José do Amatari and Paura, a 200 km reach including LMF, 87% of sediments were overbank deposits. Along this reach, LMF is practically the only vàrzea floodplain, therefore the sediment influxes through both overbank and channelized processes might be underestimated, however the proportion between overbank vs channelized sedimentations should remain more or less constant. Another example is Rudorff et al. (2014a), where they estimated through hydrodynamic modeling that 93% of the water inflowing to Curuai floodplain is through overbank diffusive processes. Curuai floodplain (a vàrzea) is also located along the right bank of the lower Amazon presenting similar geomorphic style with LMF. In Curuai floodplain, although *river-recharge* or overbank thresholds haven't been calibrated like LMF in our study; however it could be easily confirmed through examination of multi-temporal seasonal SSC distribution maps that overbank diffusion starts several months after the channelized flow (Park and Latrubesse 2014's Figures. 7 and 8). Similarly with LMF (SSC map in June showing inundation of northeastern banks in Figure 3.6), the overbank diffusion occurred only along the eastern boundary of the Curuai floodplain (i.e. less than 50% of the entire floodplain levee

length). Major characteristic processes of channelized and overbank flows in the Amazon are summarized in Table 3.3.

Table 3.3. Comparative summary of the two major recharge flows in large rivers.

	Channelized flows	Overbank diffusions
Determines	Inundation continuity and flood frequency	Major portion of water volume and transport rate
Associated processes	Inundation order, residence time, and recessional process	Overbank flooding after bankfull
Spatial patterns depends on	Floodplain geomorphology	Proximity to the river and bank heights
Initial recharge occurs	Earlier	Later after the channelized flows
Inundation duration	Longer	Shorter
Water and sediment contributions to floodplain	Smaller	Larger

3.5. FINAL REMARKS AND CONCLUSION

Hydrological connectivity for ecologists describes the relationship between flood pulse (as a dominant explanatory variable) and the ecological variables, as it has been conceptualized in terms of water volume and the rate of water transfer from the mainstream (and branches if present) to the floodplain. It has been extensively utilized as a central idea in ecohydrology, especially after the development of the flood pulse

paradigm (Junk et al. 1989; Neiff 1996; Neiff et al. 2003; Pringle 2003; Tockner et al. 2000). Therefore, for floodplain ecologists, lateral connectivity and distance of the floodplain to the active channel have been considered an essential factor in characterizing river-floodplain hydrological connectivity (Amoros and Bornette 2002; Heiler et al. 1995). However in large rivers, as shown in this chapter, the complexity of the floodplain geomorphic mosaic, which results in the wide range of water stage variability over floodplain, different local hydrological inputs, and intricate mechanisms of flow transferences, (Dunne and Aalto 2013a; Latrubesse 2012; Mertes 1997), has to be considered as part of the analysis of hydrological connectivity processes (Drago et al. 2008; Marchetti et al. 2013; Neiff et al. 2003; Stevaux et al. 2013).

In the largest alluvial rivers, which are mostly anabranching (Latrubesse 2015), it is common that hydrological connectivity from the main channel toward the floodplain starts below bank full river stage through channelized flows or by localized overbank flows in the lower geomorphic units (Drago et al. 2003; Lininger and Latrubesse 2016; Mertes et al. 1995b). Using the Lago Miratuba Floodplain in the lower Amazon River as a representative case of incomplete floodplain, 12 morpho-hydrological individual floodplain lakes were identified as base of “geomorphic units” after an extensive geomorphic mapping of the area. These individual geomorphic units simultaneously function as both flow paths in the floodplain hydrological routings and nodal points for the seasonal water storage, and are characterized by different recharging conditions (through sequential river pulses), water residence and recessional periods. We observed that the hydrological connectivity processes along the geomorphic units happen through

complex internal routings of water flows over space and time, mainly by the floodplain channels. These channelized flows, controlling the temporal continuity of inundation and flood frequency, were predominantly dependent on the floodplain geomorphology. Thus, hydrological connectivity of 12 geomorphic units varied significantly, as inundations from the river over different units were initiated each at specific river stage thresholds. For example, the unit1 (first connected unit from the river) had *river-recharge* threshold of 1502 cm, while unit12 (last connected unit) had 1958 cm. Likewise, stage durations of connectivity for unit1 and 12 were 73% and 29%, respectively, presenting a dramatic gap (~45%) in their connectivity durations. Identified connectivity thresholds were validated during the field work conducted in June of 2016.

The connectivity processes over different geomorphic units were not correlated with their distances from the river (Figure 3.7A and Table 3.3) (similar observations by Hudson et al. 2012; Phillips 2013). This implies that, despite the overbank diffusion transports major portion of water volume and largely determines sedimentation rates in the Amazon River floodplain (Table 3.3), the “flood pulse” model (Junk et al. 1989) mainly concerned with the lateral connectivity only partially explains the diverse mechanisms of hydrosedimentary transferences and their spatiotemporal interrelations between different geomorphic units at regional scale. Therefore, specific studies have to be carried out, in reach by reach, to calibrate individual thresholds of hydrological connection-disconnection levels and flood routing paths those are dependent on the internal geomorphic variability of the floodplain.

Given that the largest floodplains are morphologically complex, which their hydrosedimentary functioning is related to the anabranching main channel processes, the methods proposed in this study can be applied to investigate floodplain hydrogeomorphology of other large rivers around the world.

Chapter 4: The Amazon River Rating Curve at Obidos Revisited Incorporating Channel-Floodplain Interrelated Processes

4.1. INTRODUCTION

Obidos, the lowermost gauge station in the Amazon River Basin, represents approximately 80% of the drainage area and hydrology of the basin (Filizola and Guyot 2009) and records the largest fluvial flows in the planet. Located approximately 750 km upstream from the mouth, it is considered the closest station to the Atlantic Ocean free from the tidal effects (Kosuth et al. 2009). Hence river stages (water levels) and annual water fluxes of the Amazon Basin have been estimated at Obidos since 1928 and 1968 respectively by the Brazilian Water Agency (ANA). Locally, Obidos acts as a nodal point (geologic constraint by sedimentary rocks on the left bank) where the Amazon River becomes a single channel, separating anabranching channels up- and downstream (Latrubesse 2008). To produce daily discharge (Q) series at Obidos, ANA adopted the water level-discharge rating curve by Callède et al. (1997) (and in turn Hydrogeodynamics of the Amazon - HYBAM). Since then, the discharge record at Obidos has been widely used for scientific communities over decades to analyze the river hydro-sedimentary regime, run hydrological models, assess floodplain inundations and flood hazards, and estimate the suspended sediment discharge of the Amazon Basin (Bonnet et al. 2008; Bourgoin et al. 2007; Dunne et al. 1998b; Filizola and Guyot 2009;

Lima et al. 2003; Martinez et al. 2009; Park and Latrubesse 2014; Rudorff et al. 2014a, among many others).

However, it has been recently argued by Filizola et al. (2014) that estimating the Amazon discharge at Obidos using the traditional rating curve methods could be problematic, mainly due to the largest water-saturated floodplain existing along the lower Amazon (e.g. Curuai floodplain with inundation area of 2,500 km^2) which actively stores water during the water level rising stage (WL_{rising}). After the initial hydrological connection of the main channel with the surrounding vast floodplain during WL_{rising}, the *Q* and water level (*WL*) relationships is distorted as significant portion of water discharge of the main channel is diverted to floodplain; while *WL* is keep rising. Therefore Filizola et al. (2014) postulated that the historical *Q* at Obidos estimated by *WL* published by ANA, probably are overestimated during flood stages. The level of uncertainty it introduces on the rating curve is yet unknown, however the water discharge data have been used for a variety of applications across the disciplines concerning the Amazonian fluvial environments. For example, results on total sediment fluxes of the Amazon River can be affected by the discharge variability, as suspended sediment concentration (SSC) is high during the WL_{rising} (Park and Latrubesse 2014) and the maximum sediment discharge occurs also during March (Park and Latrubesse in prep.).

In this study, current issue concerned with the misleading of discharge rating curve at Obidos is examined based on series of acoustic Doppler current profiler (ADCP) measurements collected over different seasons, geomorphological and sedimentological

data collected in the lower Amazon through field work, and digital elevation models (DEM). Specifically in this chapter 1) water level thresholds of the river-floodplain hydrological connectivity around Obidos is identified, 2) seasonally varying hydrological patterns in the channel which distort the rating curve is investigated during WL_{rising}, 3) the geomorphologic factors seasonally controlling the *WL-Q* relations were assessed and 4) a revised stage-dependent rating curve at Obidos is proposed.

4.2. DATA AND METHODS

4.2.1. Flow and Bathymetric Surveys around Obidos

Water flows and bathymetric data around Obidos were collected during a field work in June 28th-July 4th, 2016. Surveys were performed both in the main channel and multiple floodplain channels connecting the Amazon River and Curuai floodplain (Figure 4.1). We used GPS-linked ADCP (Teledyne RDI Rio Grande 600 kHz) for the flow measurements at Parintins (1 transect) and Obidos (4 transects) with an interval of one day (June 28th-29th, 2016). Acquired transect data is further processed using Velocity Mapping Toolbox (Parsons et al. 2013) to visualize the asymmetric flow structure (depth-averaged flow velocity and transverse profile) in conjunction with the asymmetric topographic controls derived from SRTM DEM. Depths at nadir and sidescan images of channel bed were acquired using a side-imaging device (Humminbird 899Ci HD) over the floodplain channels. Although floodplain channels could be very shallow (<1 m), this

device (down/side imaging simultaneously) efficiently scans the channel bed in shallow water depth (<20 cm, at 200 kHz beam mode).

4.2.2. Revising the Rating Curve Based on HYBAM ADCP Data

All existing recent ADCP transects at Obidos were compiled (N=534, 1995-2011) archived at HYBAM. In this archive, all measured ADCP transects' metadata is stored in raw format (uncleaned data), which requires filtering processes. First, surveyed channel transects shorter than 2.1 km were regarded as incomplete and excluded. Then, since several measurements were performed (more than four times according to the general ADCP protocol) in a given surveyed day, discharge values outside the 5% error after correlation analysis were also removed. Remaining sets of ADCP *Q* values were averaged by dates and then superimposed over the existing Obidos rating curve (Callède et al. 1997). Timing and magnitude of deviation of ADCP *Q* over the Callède et al. (1997)'s rating curve is visualized. Here, daily *WL* data both at Obidos (an explanatory variable) and Curuai gauge stations were also supplied from HYBAM.

4.2.3. Incorporating Overbank Diffusive Flows and Bank Stability

Overbank diffusion process, which happens after the channelized flows is mainly controlled by the bank height along the river (Mertes et al. 1995a). Therefore, information on bank height along the levee complex, integrated with our field observations provides clues not only on the locations, but also the timing of the overbank processes. This further elucidate the deviation of the ADCP *Q* points from the Callède et al. (1997)'s rating curve after the initial hydrological connection through channelized

flows. Vegetation-removed SRTM DEM at 90-m (O'Loughlin et al. 2016) was used to extract bank elevations at every 90 m interval longitudinally along the natural levee of the Curuai floodplain. Although SRTM DEM does not provide accurate topography of levees due to the flatness of the landscape, it is useful in assessing the relative elevation variability of the relief along neighboring points (Park and Latrubesse 2017). For that reason, field control of bank heights is fundamental. During field work on July 4th of 2016, bank heights along the levee were measured. Elevation at river surface is calibrated with water level data collected at Obidos on February 16th of 2000 (i.e. 429 cm on same day of SRTM operation) and also corrected for the channel slope (i.e. 2 cm/km) (Hudson et al. 2013).

Migration rates (as channel-width per year, ch-w/yr) for the Amazon River around Obidos and Parintins were also calculated to assess their bank stability. We digitized channel banks based on Landsat 5-7 images (during low water seasons throughout 1985-2005) at a longitudinal spacing of approximately 100 m. Then difference polygons were generated induced by net erosion or deposition to calculate the average channel migration rates (Further details in Latrubesse et al. (2017).

To illuminate the water storage role of floodplain, we also produced inundation frequency map by converting 16 years (2001-2016) of MODIS 8-day composite image (MOD09Q1) to water masks using density slicing (NIR<1) and then averaging them (Figure 1a).

4.3. RESULTS AND DISCUSSION

4.3.1. Downstream Decrease in the Amazon River Discharge Due to Floodplain Water Storage

In contrast to the geomorphological recognition of floodplain as sediment sink in the lower Amazon (downstream Madeira confluence) (e.g. Dunne et al. 1998b; Latrubesse 2015), yet the role of these extensive floodplains on downstream river discharge variability hasn't been adequately studied. Alsdorf et al. (2010) estimated the volume of seasonal water stored in floodplain along the different reaches of the Amazon using satellite altimetry, but its influence on the main channel discharge and stage hasn't been explored. In this section, the results on the role of floodplain as water storage on the downstream decrease of the river discharge is presented based on the ADCP measurements during the field work conducted in June-July 2016 (WL_{peak}-$WL_{falling}$) (Figure 4.1a).

At Obidos same cross-section was measured 4 times. Due to logistic and time constraints in the field, a single ADCP transect has been measured close to Parintins (Figure 4.1a). Hence to account the natural and technical uncertainties associated with the *Q* measurments at Parintins, possible error range of ±5% are reported (general ADCP protocol) and confirmed that all measurements had "%bad bins=0%" in its metadata. Although good part of water-saturated floodplain is well developed downstream of the Madeira conflunce (Mertes et al. 1996a), the largest floodplain lakes in the Amazon River appears downstream of Parintins. In this reach, the rivers is confined by well-

developed continuous levees and the floodlain is characterized by large lakes, floodplain channels, splays and fluvial deltas (Latrubesse 2012; Lewin et al. 2017). Along the 180 km reach in the lower Amazon in between Parintins and Obidos, there is no major tributary inputs other than Trombetas River from the left banks. However, interestingly, the difference between the upstream ($Q_{Parintins}$ (205) + $Q_{Trombetas}$ (2) =$207 \cdot 10^3$ m^3/s) and downstream (Q_{Obidos}=$192 \cdot 10^3$ m^3/s) discharges of this reach measured with one day interval was $15 \cdot 10^3$ m^3/s. That is, from Parintins to Obidos, $15 \cdot 10^3$ m^3/s of discharge has been lost to floodplain (Figure 4.01a). This value is approximately 8% of the Q_{Obidos} on the same day, which is outside the error range of ADCP. Therefore it is relevant to consider that this observed downstream decrease in discharge indicates a water loss over to the floodplain. Thus, we can contemplate the effect of the seasonal flooding over these vast floodplain (role of floodplain storage) on river water discharge. It has been postulated that in large rivers, negatively skewed hydrographs with slower rising than falling limbs are the consequence of floodplain storage (Fleischmann et al. 2016). In the case of Obidos, I assume that the slightly negatively skewed hydrograph (Figure 4.02d) is due to the flooding and storage processes along the floodplain.

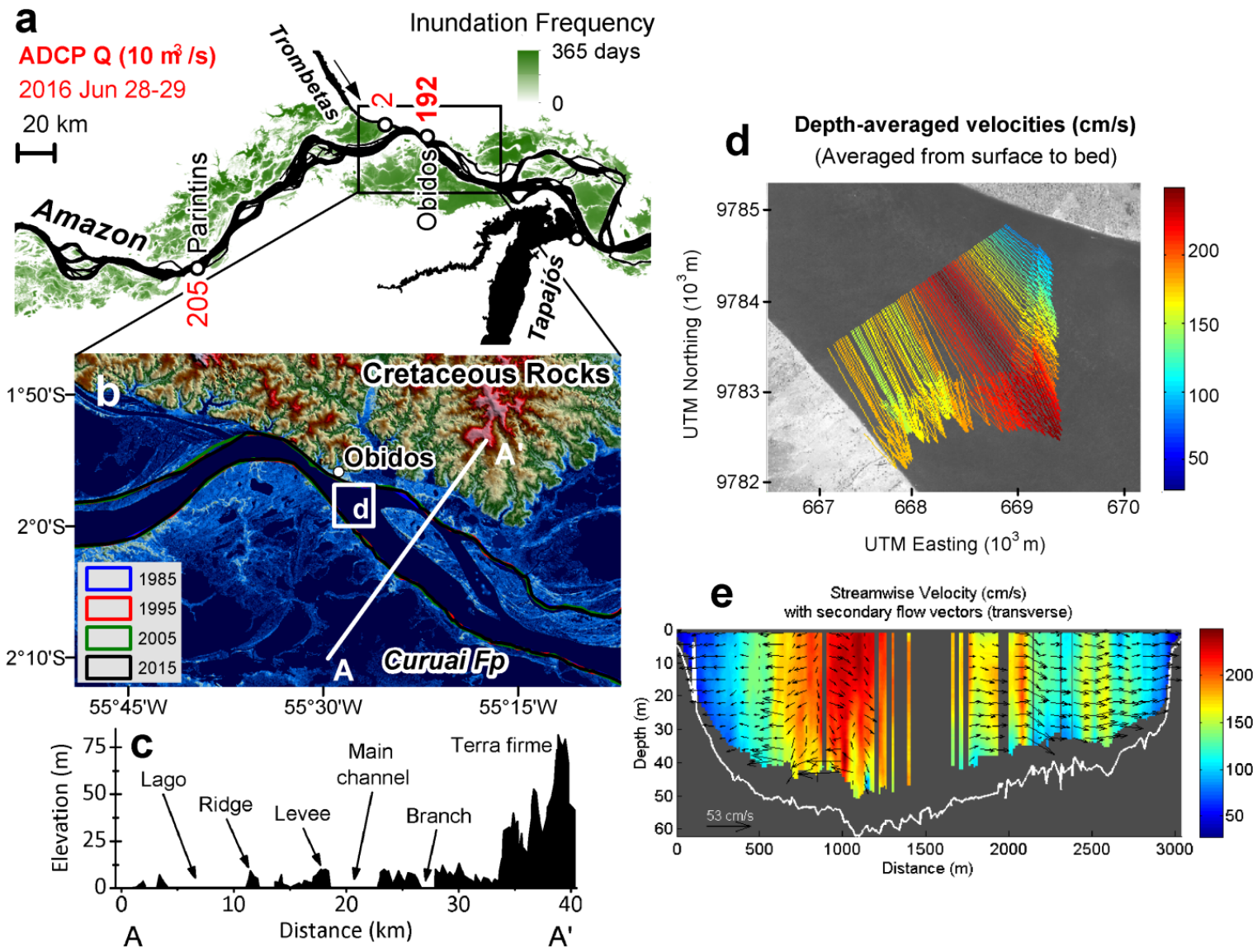
a
ADCP Q (10 m³/s)
2016 Jun 28-29
20 km
Inundation Frequency
365 days
0
Trombetas
Amazon
Parintins
Obidos
Tapajós
205
2
192
b
Cretaceous Rocks
Obidos
d
A
A'
Curuai Fp
1985
1995
2005
2015
1°50'S
2°0'S
2°10'S
55°45'W
55°30'W
55°15'W
c
Elevation (m)
Lago
Ridge
Levee
Main channel
Branch
Terra firme
Distance (km)
d
Depth-averaged velocities (cm/s)
(Averaged from surface to bed)
UTM Northing (10³ m)
UTM Easting (10³ m)
e
Streamwise Velocity (cm/s)
with secondary flow vectors (transverse)
Depth (m)
53 cm/s
Distance (m)

Figure 4.1. (a) Lower reach of the Amazon River including Parintins (-2.63333°, -56.75195°), Obidos (-1.94722°, -55.51111°) and Tapajós confluence. ADCP measured discharge values during the June 2016 are in red color indicating the downstream decrease from Parintins to Obidos. Floodplain inundation frequency (0-365 days) is shown in green while the Amazon River main channel and tributaries are in black. (b) SRTM DEM showing the contrasting geomorphologic-geologic characteristics between left (Cretaceous sedimentary rock-Alter do Chao Formation) and right (well-developed alluvial floodplain, Lago do Curuai) banks along the Amazon River around Obidos. Channel bank edges changes through 1985-2015 are shown to assess the migration rates (stability). (c) Elevation profile of A-A' indicated in b. (d) Depth-averaged velocity processed using VMT from ADCP transect data (extent indicated in b). (e) Velocity profile with secondary vectors showing complex flow structure over asymmetric bathymetry of the transect at Obidos.

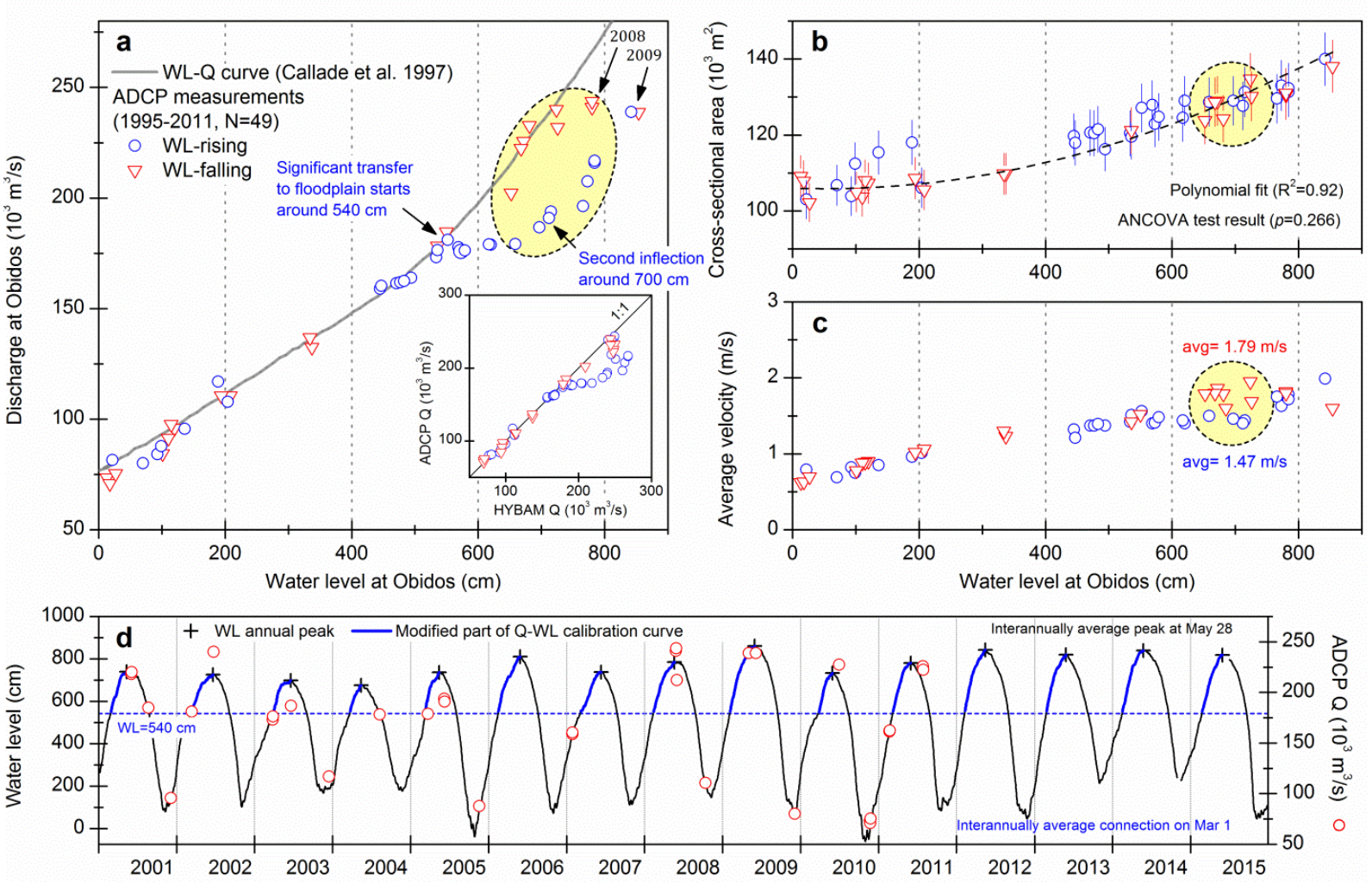
a
WL-Q curve (Callade et al. 1997)
ADCP measurements
(1995-2011, N=49)
WL-rising
WL-falling
Significant transfer
to floodplain starts
around 540 cm
Second inflection
around 700 cm
2008
2009
1:1
ADCP Q (10^3 m^3/s)
HYBAM Q (10^3 m^3/s)
Discharge at Obidos (10^3 m^3/s)
Water level at Obidos (cm)
b
Cross-sectional area (10^3 m^2)
Polynomial fit (R^2=0.92)
ANCOVA test result (p=0.266)
c
avg= 1.79 m/s
avg= 1.47 m/s
Average velocity (m/s)
Water level at Obidos (cm)
d
WL annual peak
Modified part of Q-WL calibration curve
Interannually average peak at May 28
WL=540 cm
Interannually average connection on Mar 1
Water level (cm)
ADCP Q (10^3 m^3/s)

Figure 4.2. (a) Discharge rating curve by Callede et al. (1997) superimposed by the ADCP measurements (N=49, HYBAM database) at corresponding water stages. It can be seen that, after the water level of 540 cm at Obidos during the Q_{rising}, measured discharge starts to deviate from the rating curve. Zone of dispersion (Yellow circle) is indicated where measured discharge largely varies at similar water levels depending on seasons. Inset plot shows the cross validation results between discharge estimated and measured by HYBAM and ADCP, respectively. (b) Cross-sectional area (ADCP) plotted with water level showing no significant differences between rising and falling limbs. (c) However, average velocity, within the zone of dispersion, shows faster flows during the falling limb than the rising limb at similar water levels. (d) 15 years water level record (ANA database) at Obidos with the identified water level threshold starting to deviate from the rating curve indicated (540 cm). Overlaid blue line represents period between threshold water level and peak discharge, where the estimated discharge necessitates new calibration with ADCP data. ADCP Q records (red dots) are to show the temporal availability of the data.

4.3.2. General Characteristics of the Obidos Cross Section

Obidos cross sections is geologically and geomorphologically composite with an erosional left bank developed on resistant Tertiary–Cretaceous sedimentary rocks of the Alter do Chão Formation, while the right banks developed on alluvial materials that conform a long natural and stable levee (Figure 4.1b and c). The mean width of Obidos cross section is 2.35 km and the mean depth is 46.4 m. Mean annual *Q* of the Amazon at Obidos is 176,000 m^3/s with annual water level fluctuation of ≈7m, calculated based on HYBAM dataset (1968-2015). Peak water level of 794 cm is attained around May 28th on inter-annual average (2001-2015) (Figure 4.2d). However, the channel cross-section is asymmetric and concentrates higher velocity

and flows toward the right bank (Figure 4.1d and e). Average flow velocity can be low as 0.55 during WL_{low} to 1.95 m/s during WL_{peak}.

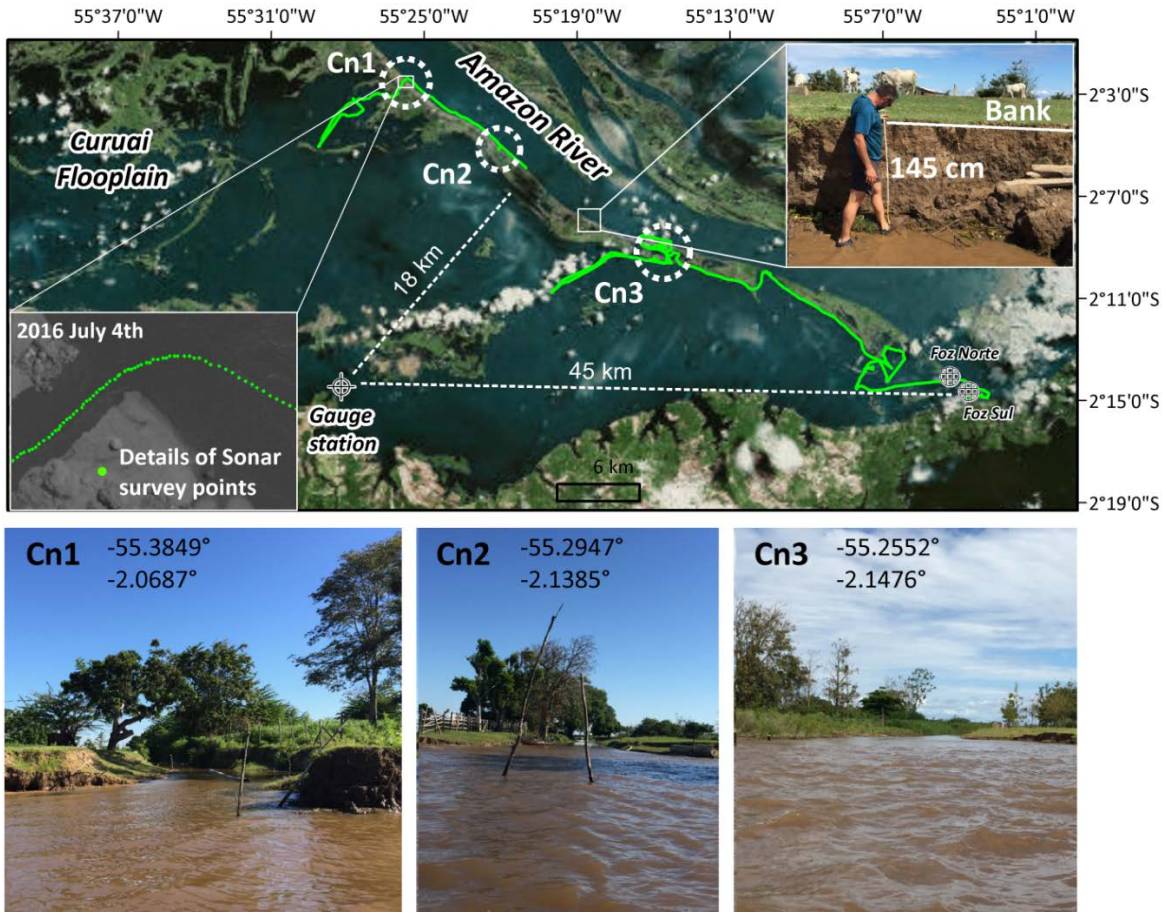

Figure 4.3. Verifying the channel-floodplain connectivity water level threshold (540 cm) at Obidos identified in Figure 4.02a. Sonar bathymetric survey routes along the Amazon River right bank on July 4th, 2016. Three channel-floodplain hydrological connections (Cn1-3, indicated as white dashed-circles) are identified, where the pictures of their entrances from the river are also shown. Inset picture shows Maxi Bayer measuring the bank height above water level during the field work.

4.3.3. Stage-Discharge at Obidos: Channel Stability, Channelized Flow and Overbank Diffusion

Filizola et al. (2014) pointed out that the existence of the vast floodplain around Obidos (e.g. Curuai floodplain) is the major factor introducing the distortion of *Q*-*WL* relations during flood season, which could overestimate peak discharge by 10-20%. Another probable factor they mentioned to affect the rating curve includes the steep curvature of the channel immediately upstream the gauge station, which might produce the local backwater effect and asymmetric flow structure (i.e. flows concentrated toward left bank) (Figure 4.1b-e). By using ADCP data, here we address the following issues: 1) in what period the rating curve start to overestimate discharge? Thus, what is the channel-floodplain connectivity threshold?; and 2) during this flooding period, how the hydrogeomorphic behaviors change? After addressing these questions, we verified the identified connectivity threshold (as river stage) during the field work in 2016, and modified the existing rating curve at Obidos station.

4.3.3.1. Channelized connectivity thresholds at WL_{rising}

When ADCP *Q* points are plotted along with the *WL* at Obidos, deviations of these ADCP points during WL_{rising} start to occur when the *WL* is close to 540 cm (Figure 4.2a). The hydro-geomorphological significance of this identified threshold is assessed, i.e. *WL*=540 cm, and confirmed that it is related to the channel-floodplain connectivity processes. At this threshold water level, *Q* increments start to significantly decrease, flattening the rating curve because at this moment, the river stage is sufficiently high to

make hydrological connection to the floodplain, and to start water transference and storage through channelized flows.

The threshold stage of 540 cm is verified through bathymetric survey in the three floodplain channels connecting river and floodplain, and measurements of the levee heights along Curuai floodplain (Figures 4.3 and 6). Average widths of the three identified floodplain channels along the Curuai eastern boundary ranged from 5 to 20 m. Bathymetry of the channels was very flat and measured depths were 62 - 65 cm. When the average depth over the floodplain channels (i.e. around 64 cm for convenience) is subtracted from the water level record at Obidos on the same day (i.e. 612 cm on July 4th, 2016), 548 cm stage is calculated. From here 10 cm is further subtracted as the Sonar transducer fixed at the tethered boat was submerged while surveying. Finally 538 cm as the hydrological connectivity threshold is retrieved, which is considered an empirically driven water level threshold required to initiate the water flow through channelized flows from the river.

Using water surface slopes between Obidos and Curuai gauge stations, we also assessed the hydrological connectivity processes in Curuai through different seasons during 2006-2007 (standard hydrological year of the Amazon (Park and Latrubesse 2015). To compare water level data from the stations with different stage baseline, we normalized water levels at each station by their mean annual water levels (Figure 4.4). Differences in the normalized water levels of the two stations indicate the water surface slope between the main channel and floodplain, providing information on the initiation of

the different stage-dependent connectivity processes over time. At Curuai, there are two permanent connections: *Foz Norte* and *Foz Sul* along the east-end (Bonnet et al. 2008) (Figure 4.3). Water influx through these permanent connections starts around late October and relatively small slopes are maintained through late February (Figure 4.4b). In early March, when the river becomes hydrologically connected to the floodplain through Cn1-3 (Figure 4.3), the slope abruptly increases. Because before these connections, the water surface slope between the Amazon River and Curuai gauge station was adjusted to the *Foz Norte* and *Foz Sul*, which is about 45 km (denominator of slope) away from the Curuai station. However, with the initiation of the channelized flows from the river to floodplain through Cn1-3, the slope has been readjusted to them, which are about 18 km away, increasing the slope. Note again that on inter-annual average, these connections were initiated around March 1st (Figure 4.2d). Slope starts to decrease during July and becomes zero, an equilibrium state.

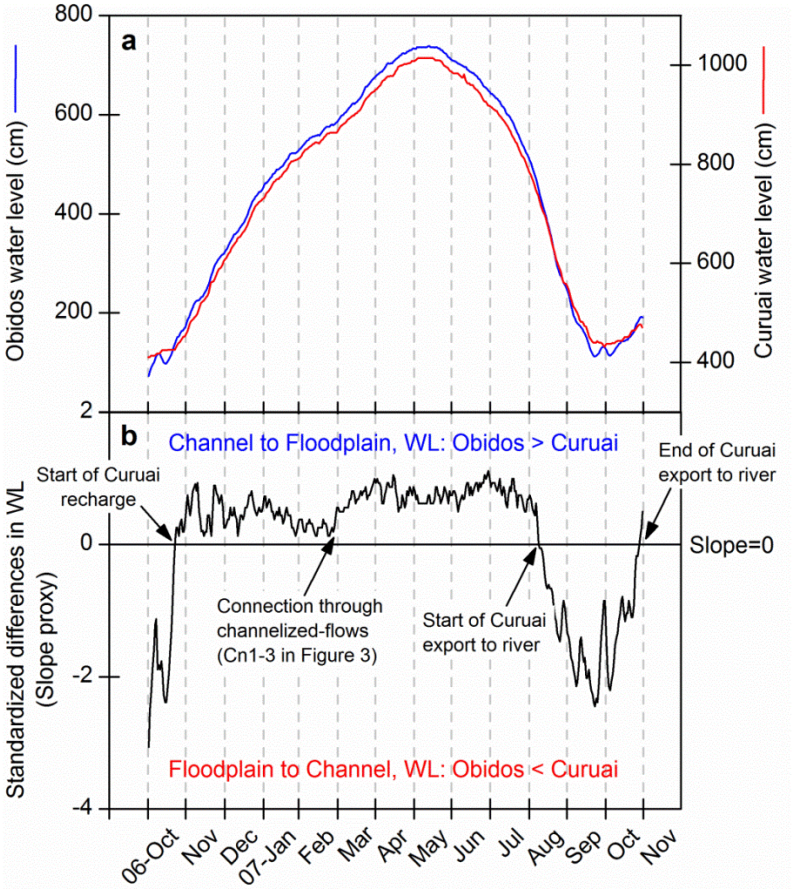

Figure 4.4. (a) Water level at Obidos and Curuai through 2006-2007. Location of Curuai gauge station is shown in Figure 4.3. (b) Standardized (by mean annual water levels) difference in water level between Obidos and Curuai, as they have different baselines.

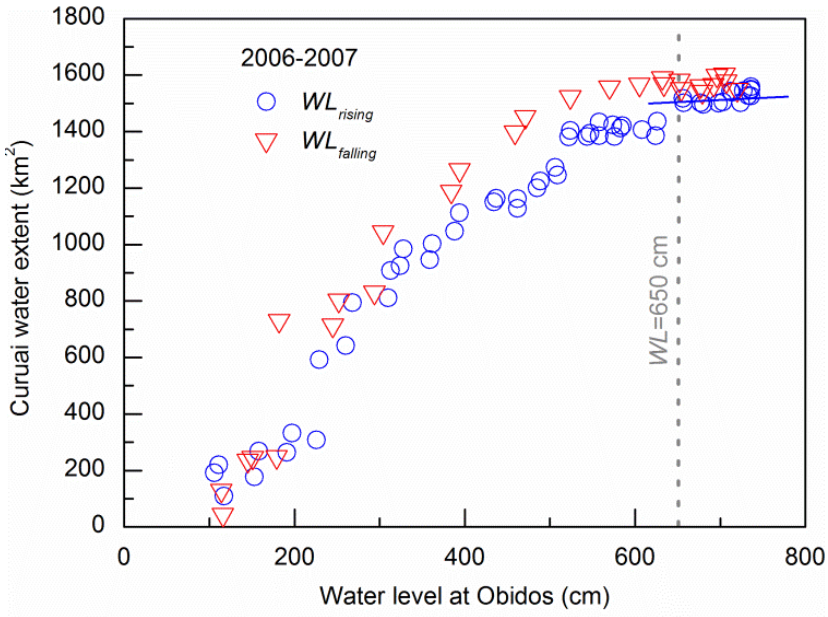

Figure 4.5. Counter-clockwise hysteresis of water extent (flooded area) at different water level at Obidos during 2006-2007 hydrological cycle for the Curuai Floodplain. Blue and red colors indicate water extent changes during WL_{rising} and $WL_{falling}$, respectively. Note that before WL=700 cm during WL_{rising}, water extent becomes constant while water level is still increasing. Water extent data are retrieved by calculating modified Normalized Difference Water Index (MNDWI) from MODIS 8-day composite images (500 m) (Xu 2006).

4.3.3.2. Overbank diffusive flooding connectivity at WL_{rising}

After the initial hydrological connection through channelized flows around *WL* at 540 cm, another inflection moment of ADCP points can be observed around 700 cm (Figure 4.2a). Above the *WL* of 700 cm at Obidos, the *Q*-*WL* slope suddenly becomes steep. Therefore, at some moment in between the river stages of 540 and 700 cm, the river attains bankfull level and starts the overbank flooding into the floodplain.

When Curuai's water extent seasonal variability in 2006-2007 is investigated, the floodplain becomes completely covered by water around *WL*=650 cm (Figure 4.5). After this stage, water extent becomes constant while water level is still increasing, until it reaches WL_{peak}. To cover up such a huge Curuai floodplain with water by only 110 cm increment in the river stage (i.e. from 540 to 650 cm) in ≈50 days, significant water influx rate through overbank diffusion seems to be necessary. Rudorff et al. (2014b) estimated an influx discharge rate as low as 300 m^3/s in early March (i.e. through channelized flows), and a significant increase with the initiation of overbank diffusion to as much as 3,000 m^3/s.

Bank heights were measured in the field at several locations along the Curuai and some representative cases are shown in Figure 4.6b-e. In 2016, the maximum recorded *WL* at Obidos was 629 cm, which was the lowest annual peak *WL* after 2001 (Figure 4.02d). During our field survey on July 4th, 2016 when the *WL* was 612 cm, good part of the natural levees used to overbank flood were above the river surface as much as 180 cm (Figure 4.6b-e). We witnessed that many of the channel banks were only a few tens of centimeters above the water stage (e.g. Figure 4.6c and e) and surveyed floodplain channels were also very low in their depth (≈63 cm, see previous section). This observation supports the argument in this chapter that both the channelized and over flows happen within relatively short periods during WL_{rising}. Bank elevation along the eastern boundary of the Curuai floodplain (red color in Figure 4.6a) is lower than that of the western boundary (blue color) on average. Majority of the levee-banks on the eastern boundary of the Curuai floodplain (where levee height is lower than western side) are

exposed at 540 cm (Figure 4.6a) but become totally inundated when the river stage reach 700 cm (as observed in Park and Latrubesse 2014 during May and June).

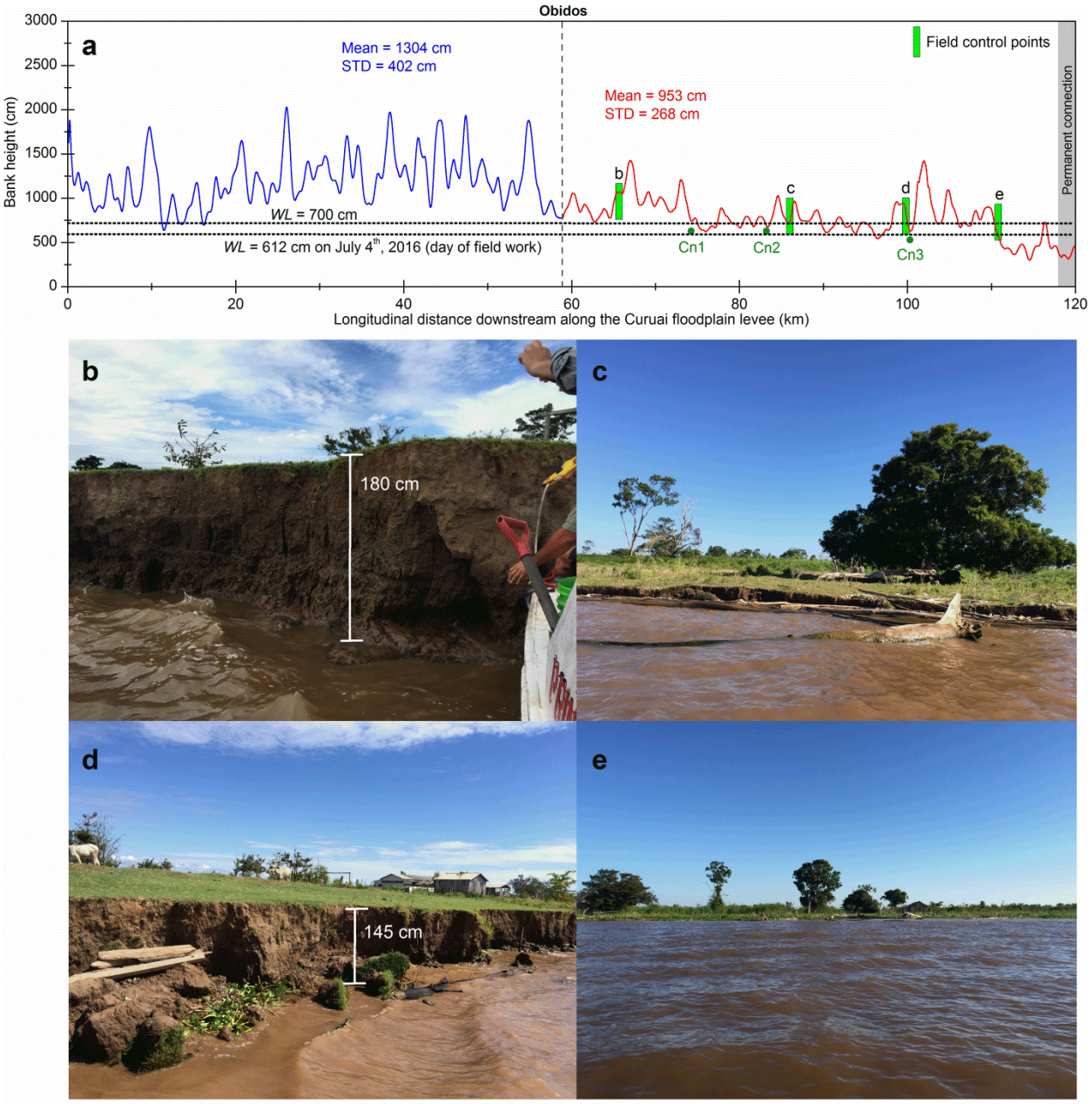

Figure 4.6. (a) Longitudinal profile of the natural levee (channel slope corrected) plotted along the Curuai floodplain downstream (120 km). Separated by Obidos, up- and downstream reaches' mean bank elevation and variability are presented. Two horizontal dashed-lines represent estimated WL=700 cm at the floodplain water-saturated moment and calibrated WL=612 cm, the measured water level at Obidos on the day of field work. Several field control points of bank elevation (b-e), and identified channel-floodplain connections are

marked (Cn1-3 in Figure 4.3). (b-e) Pictures of the natural levee of the Curuai floodplain along the right bank of the Amazon River. Levee heights are measured for b and d (locations indicated in a).

4.3.3.3. Assessing the impact of channel migration at decadal scale:

Because Callède et al. (1997)‘s curve in Obidos have been used for several decades, channel lateral migration rate has to be also considered which can potentially introduce anomalies on the rating curve. It can happen through migration of the channel that can trigger changes in the cross section or create additional connections to the large floodplain lakes on the right bank by generating levee breaching, enlarging floodplain channels and developing splay delta. To assess this factor, we calculated channel migration rates along the whole Curuai (1985-2005) (Figure 4.1a). Analysis in this chapter demonstrates that the migration rate of the Amazon is as low as 0.0011 ch-w/yr, indicating the high stability of the levee complex on the right bank at Obidos over decadal scale. Indeed, the rates of migration in this area are smaller than that of the upper middle Amazon in between Manaus and Madeira confluence (Rozo et al. 2012). Thus, it is concluded that the river lateral migration did not create new ways for channel-floodplain storage over the past several decades and that it did not affect the rating curve at Obidos during that interval of time.

4.3.4. Flood Peaks and Season-Dependent Average Velocity Introducing Hysteresis on the Rating Curve

Unlike WL_{rising}, ADCP Q well conforms to the Callède et al. (1997)'s rating curve during the $WL_{falling}$ (Figure 4.2a). However, the curves also fail to estimate Q during the flood peaks (WL_{peak}) because the stage can vary significantly without remarkable changes in peak discharges. For example, during the extreme flood of 2009 when the river flooded the whole city of Obidos, the river stage reached 842 cm at the Obidos gauge station, a value higher than the previous largest flood of 1953 when the river reached 822 cm (Filizola et al. 2014). However, despite the extreme high water level reached that year, the peak water discharge in 2009 was smaller than those of 2008 and 2012, when, curiously reached lower water levels at Obidos.

Because of the flatness of the WL hydrograph at peak discharges (as can be seen in Figure 4.2d and 4a), we calculated the derivative (slope) of daily change to differentiate WL_{rising} from $WL_{falling}$ (Figure 4.7a). The slope of WL decreases as it gets toward the WL_{peak}, however the WL becomes very smooth within the zones of WL_{peak}, which can last for near a month. This period of flatness in the hydrograph at close to WL_{peak} is characterized by very low derivative values of W. When integrated the whole cycle, we observed that above the connectivity water stage thresholds (540 cm), Q for the same WL during WL_{rising} is substantially lower than that of $WL_{falling}$ (Figure 4.2a yellow panel). However after WL_{peak}, WL start to decrease while Q can remain almost constant (Figure 4.2a). The decoupling of stage and discharge at flood peaks results in a counter clock hysteresis. To address the possible factor inducing this observed discrepancy of Q at similar WL over different seasons, we analyzed the seasonal dependency of the

hydraulic geometry of the cross section (Figure 4.2b and c) and channel roughness and slope (Figure 4.7).

The results after the Analysis of Covariance test indicate that the relationships between cross-sectional area and *WL* did not present seasonal effects (*p*-value=0.266) (Figure 4.2b). This indicates that cross-sectional area at certain *WL* is similar regardless of seasons, as speculated by Filizola et al. (2014). However, it is observed that the average velocity of the ADCP transects measured at similar *WL* were different between WL_{rising} and $WL_{falling}$ (Figure 4.2c). At the similar *WL* (and also when cross-sectional areas are similar), the average velocity during the WL_{rising} (1.47 m/s) was lower than that of $WL_{falling}$ (1.79 m/s) as much as ≈20%. Along the Amazon River, faster velocity during $WL_{falling}$ compared to WL_{rising} have been reported through the river routing simulation based on GRACE data (Han et al. 2009). This dichotomy between *Q*-*WL* data and the increased velocity at $WL_{falling}$ can be related to hydraulic factors such as seasonal changes in water surface slope and roughness. Actually, higher water surface gradient in the Amazon at Obidos during $WL_{falling}$ than WL_{rising} has been observed (Birkett et al. 2002).

By using an estimated channel roughness at Obidos we estimated water slope (*S*) by applying Manning's equation:

$$S = \frac{v^2 \cdot n^2}{R^{\frac{2}{3}}}$$

where *v* denotes average velocity (supplied from ADCP), *n* is roughness estimated as n=-0.0018·d+0.1273 (d supplied from ADCP) (Strasser et al. 2005) and *R* denotes

hydraulic radius which we substituted with mean depth (d). The values of n ranged from 0.035 to 0.02 for a dataset of mean depths at Obidos ranging from 50 to 58 m.

The calculated values of slope range from almost zero (0.0000058) to 0.000017 during the WL_{rising} and from 0.0000041 to 0.000035 during $WL_{falling}$ (Figure 4.7b). Using satellite altimetry, Birkett et al. (2002) demonstrated that seasonal water surface gradient have counter-clockwise hysteresis behavior (versus Q) as function of differential timing of inflows of major tributaries. Despite the very low values of slope, potential limitations of the Manning's equation and possible errors in ADCP measurements, the hysteresis with slightly higher water surface slope at $WL_{falling}$ than WL_{rising} is also detected in our calculations.

Other indirect evidence for this hysteresis that more energy is available during $WL_{falling}$ includes the analysis of the field suspended sediment data in different seasons by Meade (1985). His particle size analysis results showed that suspended sediment in Obidos tends to be coarser grained in $WL_{falling}$ than in WL_{rising}, implying that channel sediment transport capacity is even increased during $WL_{falling}$. This seasonal variability is also detected in the bedload dynamics, and the sandy bedload transport. Despite the size of the sandy dunes is still relatively constant at different water stages (i.e. height around 4.55 m or smaller), the migration rate of the dunes and bedload transport are higher at the beginning of the $WL_{falling}$ where they can reach a maximum migration speed of 6 m per day compared to the similar water levels during WL_{rising} (1.87 to 1.4 m per day). Also the maximum bedload transport is reached at the lower limb of the $WL_{falling}$, during August,

where it can reach ~38,500 tons per day (Strasser et al. 2002; Strasser 2008; Strasser et al. 2005). Thus, bedload transport seems to be in phase with the distribution of velocity and water slope detected by our analysis during WL_{rising} and $WL_{falling}$.

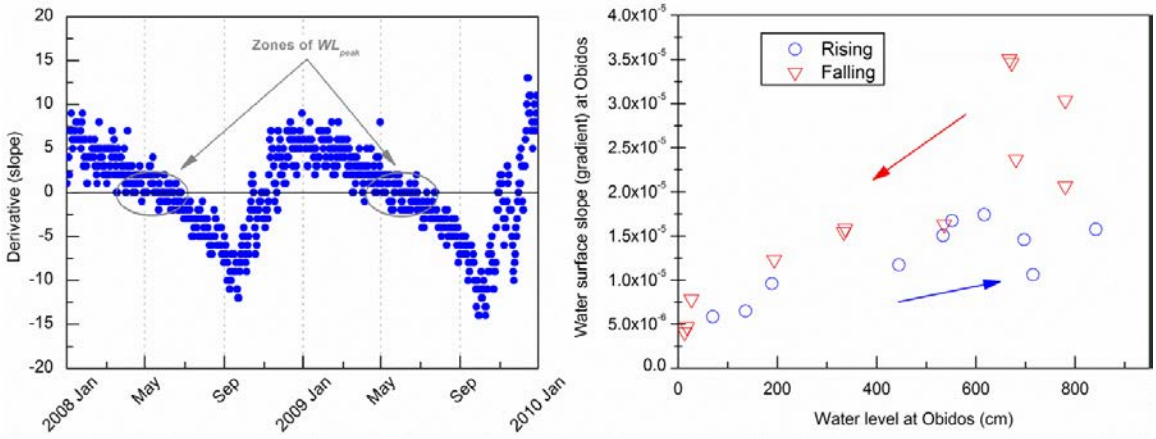

Figure 4.7. (a) Slope (derivative) of the *WL* in 2008-2009. (b) Seasonal variations in the water surface slope (gradient) calculated from Manning's equation using parameters obtained from ADCP (2000-2011).

4.3.5. Revised Discharge Hydrographs

On average over 15 years (2001-2015), water level of 540 cm, the critical stage when connectivity with the floodplain starts, was usually reached around March 1 (Figure 4.2d and 4) and the flood peaks were reached around May 28. Thus, the rating curve during the WL_{rising} is recalculated when the water stage at Obidos is above 540 cm until flood peak in May or June (Figure 4.8).

The partially revised curve was used to calculate new estimates of *Q* at Obidos during the influenced period by integrating the data derived from Callède et al. (1997)'s curve and our corrected curve for stages above 540cm (Figure 4.8a). The revised mean annual discharge (MAD) of the Amazon at Obidos is $168 \cdot 10^3$ m^3/s (Figure 4.8b), 4.6% less than the mean annual discharge calculated using the daily *Q* series from HYBAM over 48 years (1968-2015) which is $176 \cdot 10^3$ m^3/s. However when considered only the influenced period (i.e. *Q* revised months usually March-June, Figure 4.2d), the total difference in *Q* is 11.8%. The hydro-geomorphologic implications of these differences can be significant because flood stage is responsible also for the majority of sediment load transport in the Amazon as high suspended sediment concentration around Obidos is maintained during the WL_{rising} (Park and Latrubesse 2014). Particularly in March when hydrological connection to the floodplain is usually initiated, SSC in the Amazon River increases approximately to 150 mg/l, close to the peak values of the year, and thus the highest washload transport fluxes of the year at Obidos is attained as well (Park and Latrubesse in prep.). The revised rating curve provides, in addition to sediment transport, useful implications in regards to the flood hazards (Filizola et al. 2014), river-floodplain connectivity (Park and Latrubesse 2017), and hydrological modeling (Paiva et al. 2013).

The revised hydrograph at Obidos station presented as mean monthly discharge (MMD) to announce the seasonal behavior is shown in Figure 4.08a, along with other stations located at major upstream tributaries: Fazenda Vista Alegre at lower Madeira, Manacapuru at lower Solimoes, and Manaus at lower Negro. MMD of these upstream gauge stations are are also calculated from HYBAM over the same 15 years to assess the

seaonsal floodplain water storage budgets in the reach in between Madeira confluence and Obidos. We calculated mean monthly *Q* net budgets of the reach in between Madeira confluence and Obidos as Q_{OBI}-(Q_{FVA}+Q_{MAN}+Q_{MAO}) (Figure 4.9). Although hydrological connection of the river with floodplain begins usually in March around Obidos, net *Q* budget of this reach becomes negative in April on average (-16.8·10^3 m^3/s) due to substantial water storage in floodplain. Further loss of water to floodplain in May (-17.9·10^3 m^3/s) as approaching WL_{peak} is possibly related to the initiation of overbank diffusive processes. In June when WL_{peak} is usually reached, *Q* net budget of the reach is the smallest of the year, i.e. even close to zero (-80 m^3/s). During this period, channel-floodplain water balance reaches the equilibrium condition as floodplain stores water at its maximum capacity. During the $WL_{falling}$, remarkable positive *Q* net budget (net gain in channel) in this reach is observed, especially in August (25.7·10^3 m^3/s) and September (29.6·10^3 m^3/s) which lasts until October (16.2·10^3 m^3/s). These monthly gains are related to the return of water stored in floodplain to the main channel. As demonstrated, thus *Q* seasonality through the Amazon River main channel should be understood with respect to the seasonal water storage dynamics of floodplain.

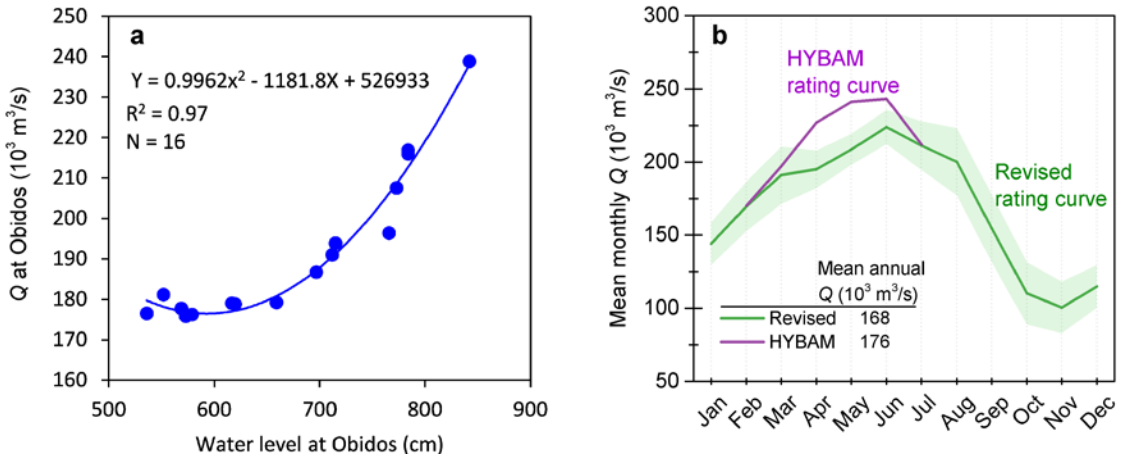

Figure 4.8. (a) Revised *Q* rating curve during the WL_{rising} when the water stage at Obidos is above 540 cm until flood peak in June. This revised curve was used to calculate new estimates of *Q* at Obidos during this period. This portion graph is shown in Figure 4.02a. (b) Mean monthly discharge and variability (standard devation) calculated over 15 years (2001-2015, from HYBAM) for the gauge stations at Obidos. Both the revised rating curve during flood stage (green) and Callede et al. (1997)'s HYBAM curve (purple) are presented.

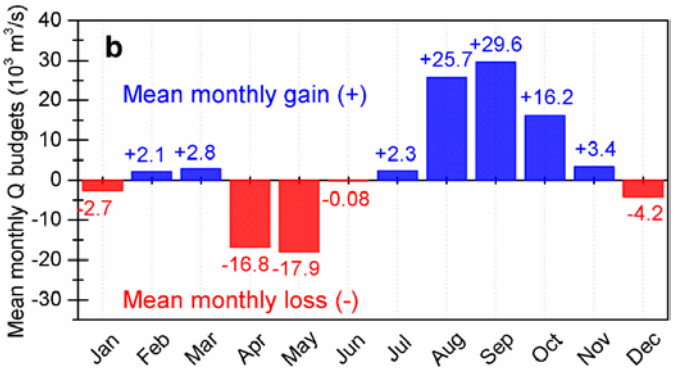

Figure 4.9. Mean monthly discharge budget of the reach in between Manacapuru and Obidos. Positive (blue) and negative (red) indicate monthly gain of water in channel and monthly loss of water to floodplain, respectively.

4.3.6. Parintins: A Recommended Gauge Station

As previously mentioned, a downstream loss of water discharge (i.e. $15 \cdot 10^3$ m^3/s) is observed in between Parintins and Obidos, along a 180 km reach along the lower Amazon due to the floodplain seasonal water storage. Based on my preliminary results we consider that Parintins (Figure 4.10) probably captures and represents better the total channelized fluxes of the Amazon River than Obidos. Thus, it is suggested that Parintins can be officially deliberated and carefully assessed by ANA and HYBAM to potentially become a complementary gauge station for water discharge estimation using the rating curve method that could provide even higher values of water discharge than Obidos. The location of the potential gauge station we recommend is approximately 12 km downstream from the existing HYBAM gauge station (code: 16350002, -2.63056°, -

56.75195°) (Figure 4.10b). This station is downstream the confluence with the Madeira River and thus incorporate *Q* of both the Madeira and the Amazon's atypical long branch, the Parana do Ramos.

At Parintins, hysteresis between *Q*-*WL* during the flood season as in Obidos, was not observed (Figure 4.10a). That is, although channel-floodplain connectivity processes around Parintins haven't been assessed, when assumed that the channel-floodplain connectivity will be developed around March 1st (the period of the connection at Obidos inter-annually), seasonal dependency on *Q*-*WL* relation after hydrological connection was not present. This simply indicates that, unlike Obidos where *Q* is overestimated as much as 11% above the floodplain connection threshold, *Q* at Parintins could probably be estimated with higher confidence from *WL* during WL_{rising} through the rating curve method.

Another basis for our recommendation is the high channel stability in the reach around Parintins. Although the river cross section at Parintins is asymmetric, it could be inferred from the SRTM DEM and the field observations that the right banks are old rocks (Cenozoic sedimentary rocks), and the left banks are very well developed and stable levee covered by fine sediments (Figure 4.10). Historical channel migration rates assessed along the 60 km reach around Parintins is 0.0032 ch-w/yr, which is much smaller than that of the entire Amazon River main channel (0.01 ch-w/yr) (Latrubesse et al. 2017) or even than the Amazon tributaries draining cratonic settings (0.0075 ch-w/yr, such as Negro, Tapajos, or Xingu Rivers) (Constantine et al. 2014). Therefore the levee

complex on the left bank confining the Amazon River around Parintins is very stable and persistent over decades.

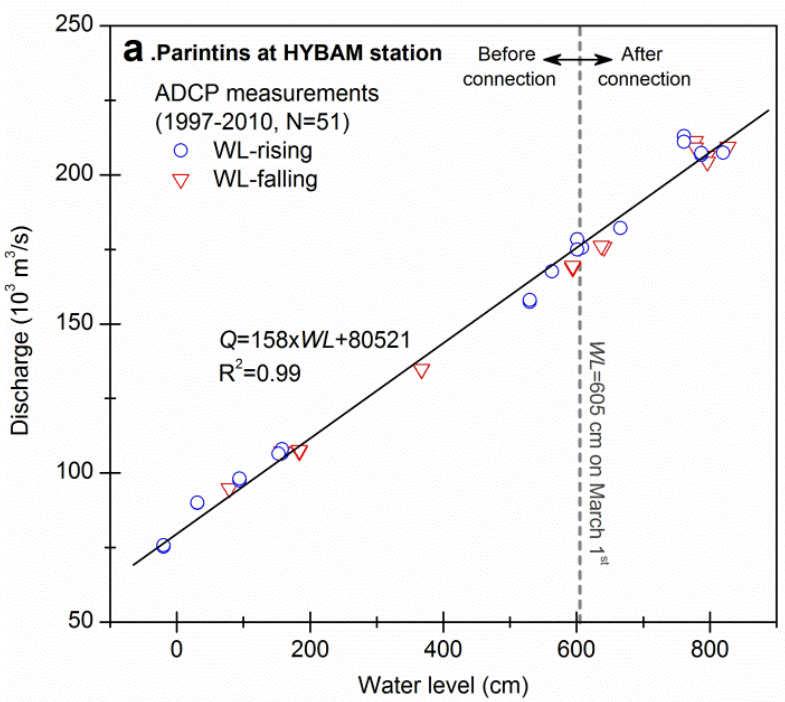
a .Parintins at HYBAM station
Before connection
After connection
ADCP measurements
(1997-2010, N=51)
WL-rising
WL-falling
Q=158xWL+80521
R2=0.99
WL=605 cm on March 1st
Discharge (10^3 m^3/s)
Water level (cm)
250
200
150
100
50
0
200
400
600
800

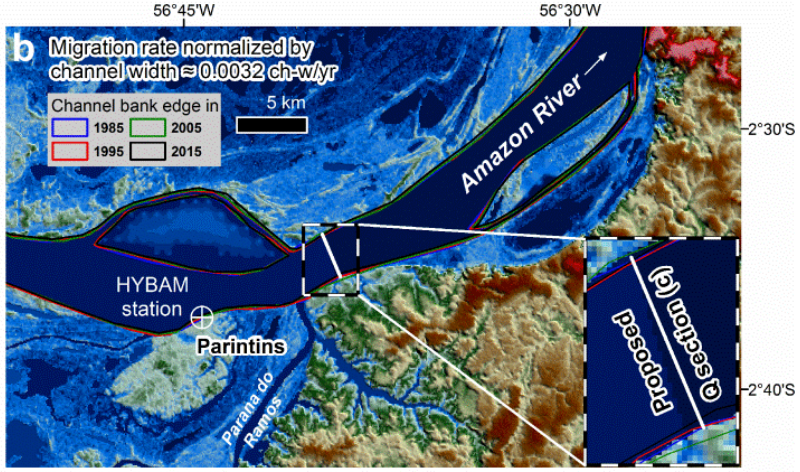
56°45'W
56°30'W
b Migration rate normalized by channel width ≈ 0.0032 ch-w/yr
Channel bank edge in
1985
2005
1995
2015
5 km
Amazon River
HYBAM station
Parintins
Parana do Ramos
Proposed Q section (c)
2°30'S
2°40'S

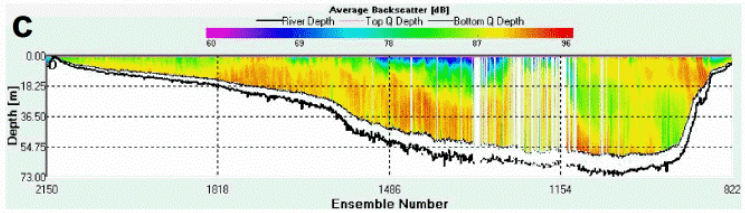
c
Average Backscatter [dB]
River Depth
Top Q Depth
Bottom Q Depth
60
69
78
87
96
Depth [m]
0.00
18.25
36.50
54.75
73.00
2150
1818
1486
1154
822
Ensemble Number

Figure 4.10. (a) ADCP Q data point (N=51 after filtering from the 106 original raw data, using the same protocol as Obidos). (b) HYBAM station at Parintins (code: 16350002, -2.63333°, -56.75195°) and our proposed *Q* section immediatley downstream of the Parana do Ramos. Average channel migration rate of the ~60 km reach shown in the map over 30 years (1985-2015) is 12 m/yr, average channel width is 3.8 km, and the normalized migration rate is 0.0032 ch-w/yr. Background is SRTM DEM. (c) ADCP transect collected on June 28th, 2016 ($Q=205 \cdot 10^3$ m^3/s) at our proposed *Q* section shown in b.

4.4. FINAL REMARKS

In this chapter, it is shown that there is seasonal storage of the water in vast floodplain in the lower Amazon during WL_{rising}. This floodplain storage introduce a slightly negatively skewed hydrograph downstream at Obidos as described by Fleischmann et al. (2016). Therefore, applying a simple rating curve may not be appropriate for estimating discharge from the water level data, particularly during the flood stage. *Q*-*WL* rating curve at Obidos is revised based on series of ADCP measurements collected at different seasons, incorporating the hydrological connectivity processes between channel and floodplain.

Based on the revised *Q* rating curve, MAD is $168 \cdot 10^3$ m^3/s, which is 4.6% less than the calculated MAD over 48 years (1968-2015) using daily *Q* data from HYBAM estimated using the existing rating curve by Callède et al. (1997). The revised MMD particularly over the modified period (usually March-June) is even 11.8% less. This could provide relevant implications for the sediment transport fluxes and floodplain budgets, given that the highest suspended sediment transport at Obidos is observed during March.

In this chapter, it is demonstrated that *Q-WL* rating curve approach as used in the Amazon can be vulnerable to the overestimation of the river discharge during WL_{rising}. Because, through at least one of the banks, seasonal hydrological connections can be developed to the large lakes beyond the levee along the Amazon River. For example, there isn't any reach along the Amazon where both sides of banks are confined by older terraces or rocks. Given that the channel-floodplain connectivity is a major factor triggering the failure of the rating curve, the proposed method in this chapter examining the interrelated processes between channel and floodplain, can not only be applied to the Amazon but also to other large river systems containing long and wide floodplain system. This approach can also be used to identify the potential gauge station such as Parintins along the Amazon River that would representatively capture the hydrological fluxes of a river basin.

Chapter 5: Spatiotemporal Distribution of Floodplain Sediment Sinks in the Lower Amazon River: A Geomorphological Assessments Using *In Situ* Gauge Stations

5.1. BACKGROUNDS: "IMPEDED" FLOODPLAIN IN THE LOWER AMAZON

The Amazon River carries an enormous amount of suspended sediment loads to the ocean each year, which is estimated to range between 500-1,300 million tons (Mt) at Obidos, the lowermost gauge station (e.g. Filizola and Guyot 2009; Mangiarotti et al. 2013; Martinez et al. 2009; Meade et al. 1979; Wittmann et al. 2011). Along the downstream sediment transport processes through a 3,000 km course (Iquitos-mouth), the fine suspended sediment fluxes are significantly affected by the exchange of sediments between the extensively developed floodplain (Dunne et al. 1998b). Floodplain in the Amazon River has been recognized and documented not only as an active water storage (Bonnet et al. 2008; Meade et al. 1985; Richey et al. 1989), but also as an important sink of sediment (Dunne et al. 1998b; Latrubesse 2015; Meade et al. 1985; Richey et al. 1989). Floodplain experiences continuous exchange of water and sediment with the river, that the annual water storage and sediment net deposit in floodplain are estimated to reach 235 km^3 (Alsdorf et al. 2010) and 500 Mt (Dunne et al. 1998b), respectively along the Brazilian Amazon. However the most remarkable sediment sinks are developed

downstream of the Madeira confluence (here defined as “lower Amazon”) where massive accumulations of silt and clay occur inter-annually.

The major floodplain style responsible for storing water and trapping sediment in the lower Amazon is “impeded floodplain” that contains large-rounded lakes (Latrubesse 2012; Mertes et al. 1996a). Mosaicked with numerous rounded lakes in different sizes and depths over a flat surface, water level and flood extents of these lakes seasonally oscillate in phase with the seasonal flooding of the main channel (Park and Latrubesse 2017). Construction of the impeded floodplain in the lower Amazon is fundamentally related to the nonlinear geomorphic evolution through longitudinal profile since the Last Glacial Maximum. Due to the lagged geomorphic response to the Holocene climatic change along the Amazon River, infilling of the valley with fine sediments is “still to be completed” along the lower Amazon River (Latrubesse 2015). These geomorphologically “incomplete” floodplain (i.e. still under dynamic equilibrium stage) allows space to accommodate impeded floodplain with large lakes, which becomes water-saturated condition during the typical flood season. Present-day flood dynamics of the anabranching channel are also an essential process for the impeded floodplain development (Latrubesse 2008). Stable levee system is constantly built through vertical accretion of fine sediments along the river and recurrent overbank flooding of fine sediments in flood basins gradually buries negative topography such as scrollbars and refine the shape of the rounded lakes (Latrubesse and Franzinelli 2002; Mertes et al. 1996a).

Along the lower Amazon, this impeded floodplain, however are not homogeneously distributed. In fact, the magnitudes of reach-scale sediment loss in the floodplain (sediment sinks) over different seasons in relation to the floodplain geomorphologic style haven't been assessed yet. In this paper, we aim to identify the floodplain sediment sinks in the lower Amazon River in between Manacapuru and Obidos, approximately 1,000 km reach, by analyzing the fine suspended sediment (washload) fluxes at the five *in situ* gauge stations from different rivers in the Basin: Fazenda Vista Alegre on Madeira, Manacapuru on Solimões, Obidos on Amazon, Manaus on Negro, and Itaituba on Tapajós, based on extensive sets of remote sensing data and recent field measurements. Identified key areas of sediment sinks and their channel-floodplain sedimentary interactions are further characterized by incorporating the floodplain geomorphic styles, flood dynamics, and washload distribution patterns over the floodplain. Here we use the term "washloads", representatively clay and silt in size < 63 μm, to indicate fine clastic sediments in a permanent suspension and assumed to be relatively uniformly distributed vertically through the water column (Colby 1963; Meade 1988). Thus, washload should be distinguished from the "suspended sediment" which includes fine sandy materials those could be in temporary suspension from the channel bed.

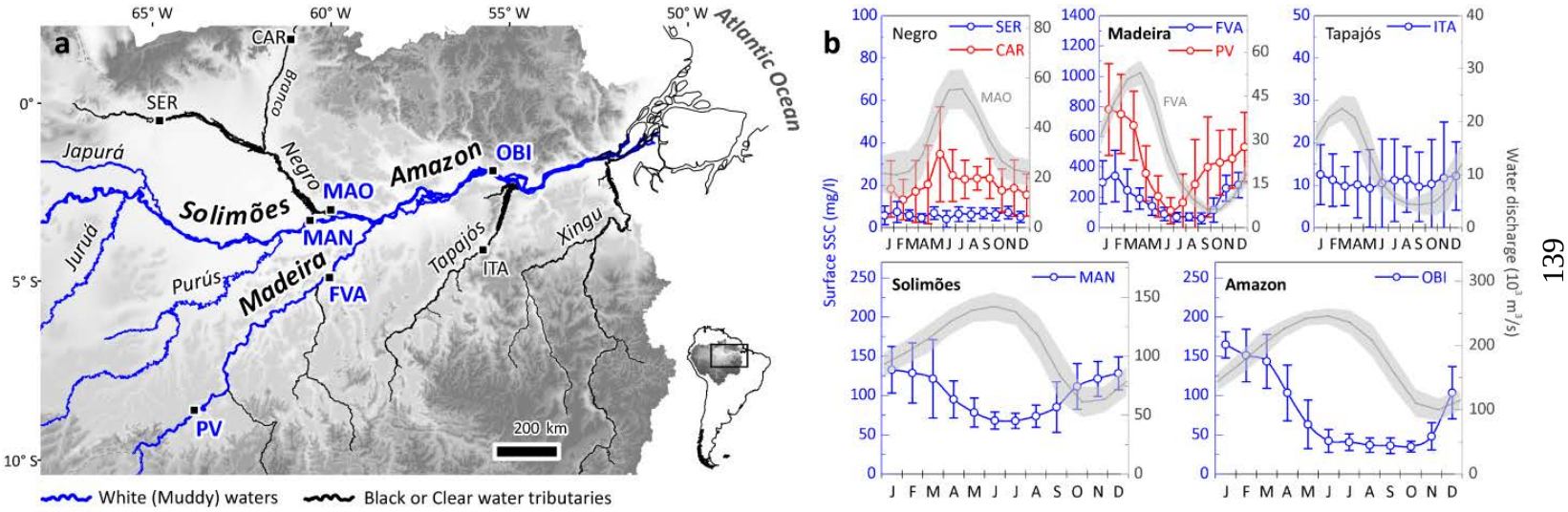
a
65° W
60° W
55° W
50° W
0°
5° S
10° S
CAR
SER
Branco
Negro
Japurá
Amazon
OBI
MAO
Solimões
MAN
Juruá
Purús
Madeira
FVA
Tapajós
ITA
Xingu
PV
200 km
Atlantic Ocean
White (Muddy) waters
Black or Clear water tributaries
b
Negro
SER
CAR
MAO
Madeira
FVA
PV
Tapajós
ITA
Solimões
MAN
Amazon
OBI
J FMAMJ J A SOND
J F M A M J J A S O N D
Surface SSC (mg/l)
Water discharge (10³ m³/s)

Figure 5.1. (a) Solimões-Amazon River map showing the entire gauge stations used in this study (SRTM background). (b) Mean monthly suspended sediment concentration (SSC) and variability (standard deviation) over 15 years (2001-2015) computed from MODIS data (for PV, FVA, MAN, and OBI), and from all available HYBAM field data (for SER N=237, CAR N=498, and ITA N=313). Mean monthly water discharge (Q) and variability computed from HYBAM field data over the same periods are presented in grey line and shade. Q at Manaus (MAO) and FVA are shown for Negro and Madeira Rivers plots, respectively.

5.2. WASHLOAD SOURCING ALONG THE AMAZON RIVER: ANDES AND TRIBUTARIES

Most of the sediment loads carried by the Amazon River are sourced from the Andean headwater regions where intensive erosional processes are dominant due to the heavy rainfalls over erodible rocks. Sediment loads of the Ucayali and Maranon Rivers, where the Amazon River is born, are estimated to be 205 and 103 Mt/yr, respectively (Guyot et al. 2007). Sediment yields of the Andean catchments can reach, as high as 18,000 tons per km^2 (Latrubesse and Restrepo 2014). For example, the Madeira River draining Bolivian and Peruvian Andes carries about 250 Mt/yr of suspended sediment loads to the Amazon River, which may contribute up to 50% of the Amazon River's annual suspended sediment budget (Filizola and Guyot 2009). Sediment inputs from other tributaries draining lowlands such as Purus and Jurua Rivers can also reach around 100 Mt/yr (Dunne et al. 1998b; Filizola and Guyot 2009). Other large black water

tributaries draining cratons, such as Negro and Tapajós Rivers, supply very low suspended sediment loads to the main stream, typically below 10 Mt/yr. Therefore, the suspended sediment concentrations and fluxes of the Amazon River main channel are substantially influenced by the water and sediment inputs from the different tributaries (Park and Latrubesse 2015).

5.3. DATA AND METHODS

5.3.1. Field hydro-sedimentological data acquisition and analysis

5.3.1.1. Discharge and suspended sediment data at gauge stations

We used two gauge stations along the Solimões-Amazon River: Manacapuru (MAN) and Obidos (OBI), and three lowermost stations from the major tributaries: Fazenda Vista Alegre (FVA) in Madeira River, Manaus (MAO) in Negro River, and Itaituba (ITA) in Tapajós River (Figure 5.01). Daily water discharge (*Q*) and surface suspended sediment concentration (*SSSC*) data at approximately every 10 days since 1960s and 1990s, respectively were supplied from the Hydrogeodynamics of the Amazon (HYBAM) for these gauge stations (Table 5.1). Due to backwater effect at the lower Negro, *Q* is not regularly measured at Manaus (Meade et al. 1991), thus we used *Q* and *SSSC* data at the two upstream gauge stations: Serrinha (SER) and Caracarai (CAR) to calculate sediment discharge (*Qs*). Discharge at MAO (Q_{MAO}) is calculated as sum of *Q* at Jatuarana and Careiro subtracted by Q_{MAN} (Ronchail et al. 2006). Monthly mean and

variability of both *Q* and *SSSC* for each gauge station are plotted in Figure 5.1b (sample sizes in caption). Gauge station hydrographs show similar trends with distinct rising (Q_{rising}), falling ($Q_{falling}$), and low (Q_{low}) limbs with slight temporal lags in their flood peaks (Q_{peak}) (e.g. Madeira in April, Amazon in June, and Negro in July).

Table 5.1. Summary of *Q* and *SSSC* field data at gauge stations used in this study.

Station (code)	River	Drainage area (10^3 km^2) [a]	Mean annual *Q* (m^3/s) [a]	*Q* data period (daily)	*SSSC* data period/ sample size	Dominant geotectonic [e]
Fazenda Vista Alegre (FVA)	Madeira	1325	2600	1967-2015	1997-2014/ 488	Andean foreland, lowland
Manacapuru (MAN)	Amazon	2148	105000	1972-2015	1995-2014[c]/ 518	Andean foreland, lowland
Obidos (OBI)	Amazon	4619	168000	1968-2015	1994-2014[c]/ 558	Andean foreland, lowland
Itaituba (ITA)	Tapajós	490	13500	1968-2015	1997-2013[d]/ 316	Cratonic (shields)
Manaus (MAO)	Negro	712	34000	1970-2014	-	Cratonic
-Serrinha (SER)	Negro	280	17000[b]	1967-2015	1996-2008[d]/ 239	Cratonic
-Caracarai (CAR)	Branco	125	3000[b]	1967-2015	1996-2014[d]/ 500	Cratonic

[a] Dataset from Filizola and Guyot (2009) and Latrubesse et al. (2005)

[b] Calculated in this study

[c] These field *SSSC* samples are used only for MODIS data calibration purpose

[d] For the black water tributaries, these field *SSSC* data is used for *Qs* calculation

[e] Amazon Basin geotectonic settings classification based on hydrosedimentologic regimes by Latrubesse et al. (2017)

5.3.1.2. Surface suspended sediment sampling and flow velocity measurements in river and floodplain

Besides HYBAM data collected only at gauge stations, 121 *SSSC* samples were additionally collected along the river and floodplain through two field campaigns: 1) 40 samples during August 27th – September 2nd, 2015 – reach in between the Manacapuru and Itacoatiara; and 2) 81 samples during June 26th- July 10th, 2016 – reach in between the Negro and Tapajós confluences. These surface water samples are collected using 500 ml bottle along the river at different locations within channel transects and in floodplain. Cellulose acetate membranes (0.45 μm) is used to filter sediments (Merck Millipore) and weighted after drying 24 hours to retrieve *SSSC*. Also, 23 bucket of surface water samples (20 liters) along the channel and in floodplain lakes were collected during 2016 field work to analyze the sediment grain size distribution of surface water. Collected bucket water samples were settled over 20 hours before removing 80% of the upper layer and then completely dried. We used laser particle scanner (Fritsch Analysette-22) to obtain grain size distribution of each sample. Analysis of collected sediment samples are performed at the University of Texas at Austin *Soils and Sediments Laboratory*.

We collected water flows velocity data in six large floodplain lakes (Miratuba, Canacari, Madaba, Paru, Curuai, and Monte Alegre) along the lower Amazon during a

field work in June 28th-July 4th, 2016 (Figure 5.8). Surveys were performed at the at least 3 km inner part of the floodplain lakes from the floodplain channel-formed crevasse delta. GPS-linked ADCP (Teledyne RDI Rio Grande 600 kHz) was used for the flow measurements.

5.3.2. Remote sensing data, processing and analysis

5.3.2.1. Estimating SSSC at gauge stations

SSSC since 2000 at each gauge station were obtained from remote sensing data. We utilized MODIS 8-day composite (MOD/MYD09Q1, L3) product both from Terra and Aqua satellites, which are atmospherically and geometrically corrected to yield surface reflectance at two bands: band 1 (620-670 nm) and band 2 (841-876 nm) (Vermote and Vermeulen 1999). Total of 2,944 MODIS HDF data covering the entire lower Amazon (tiles h11v09 and h12v09) were downloaded from LPDAAC using DAAK2Disk interface. Previously published regionally calibrated regression models based on field *SSSC* data collected by HYBAM (N=1,054) were separately applied to three gauge stations: MAN and OBI by Park and Latrubesse (2014), and FVA by Villar et al. (2013) and Latrubesse et al. (2017) (Table 5.2). All slopes of the regression models were statistically significant at 95% confidence level. Time series *SSSC* since 2000 to 2016 were extracted from a 5x5 median window over each gauge station (Ozesmi and Bauer 2002) to calculate the washload discharges. These at-gauge station estimations of

SSSC from remote sensing data are thoroughly validated both using HYBAM and our field data.

Table 5.2. MODIS calibration models to estimate *SSSC* used in this study.

Calibrated at (gauge station)	Model	RMSE (mg/l)[a]	R^2	Sample size	Mean/Max *SSSC* (mg/l)[b]	References
Manacapuru (MAN)	$SSSC=27.05\cdot e^{7.83\cdot R1}$	6.2	0.88	232		Park and Latrubesse (2014)
Porte Velho (PV)[c]	$SSSC=1020\cdot(R2/R1)^{2.94}$ (Dec-Jul)	34.1	0.92	282		Villar et al. (2013)
	$SSSC=355.3\cdot(R2/R1)^{1.39}$ (Aug-Nov)	28.9	0.81	105		Latrubesse et al. (2017)
Obidos (OBI)	$SSSC=649.99\cdot R1+3.42$ (Dec-Jun)	9.8	0.83	106		Park and Latrubesse (2014)
	$SSSC=631.68\cdot R1+1.55$ (Jul-Nov)	6.5	0.79	207		

R1 and *R2* denote reflectance and band 1 and 2, respectively.

[a] Root mean square error calculated as cross-validation from original field data.

[b] Calculated as mean annual values from MODIS-estimates (2001-2015).

[c] Models calibrated at PV are used to estimate SSSC at Fazenda Vista Alegre (FVA), because there is no major inputs or loss of sediment downstream PV until FVA.

5.3.2.2. Generating SSSC and inundation frequency maps

Regionally calibrated regression models along the Amazon (i.e. MAN and OBI) are applied to the MODIS images to generate *SSSC* maps. The MODIS composite image, that is produced with the best quality pixels out of successive acquisition periods using constrained-view angle maximum value method (Huete et al. 2002b) are efficient in generating spatially continuous maps in the Amazon Basin where heavy cloud cover is

frequently present (Mertes and Magadzire 2007). A total of 1,472 SSSC maps (at every 8 days) were created along the Amazon River reach including floodplain between Manacapuru and Obidos (Park and Latrubesse 2014). Further image processing methods including classification and water mask extraction, controlling pixel quality, and interpolating unqualified pixels can be found in Park and Latrubesse (2014). *SSSC* maps over both channel and floodplain enable quantitative assessments of the spatiotemporal distribution patterns of the *SSSC*. Moreover, imaging of the water coverage over the levee complex and sediment plumes through the splay delta in the impeded rounded lakes in floodplain from remote sensing provide direct observations of the overbank diffusive processes. We also produced inundation frequency map by converting 16 years (2001-2016) of MODIS composite image to water masks using density slicing (NIR<1) and then averaging them.

5.3.2.3. Analyzing channel migration rates (1985-2015) using Landsat

Bank stability is an important factor to analyze in assessing sediment discharge of the river. Because if the river is laterally active (e.g. abandoning branches or generating new connections to the floodplain), the Amazon River's sediment discharge might be inter-annually variable due to the local controls on the transferences and storages of suspended sediments. For this we assessed the channel migration rates (as channel-width per year, ch-w/yr) for the whole lower Amazon in between Manacapuru and Monte Alegre (MAL) over 30 years (1985-2015) to examine the channel bank stability. First, Amazon channel banks were digitized based on Landsat 5-7 images (30 m resolution at

100 m longitudinal spacing) during low water season at every 5 years interval. Then we generated difference polygons induced by erosion or deposition to calculate the average channel migration rates. Our calculated rates were compared to the published migration rates of the further upstream Amazon (Constantine et al. 2014) and the Amazon's other large tributaries (Latrubesse et al. 2017).

5.3.3. Calculating sediment discharges at gauge stations and floodplain budgets

Washload fluxes ($Qs_{washload}$) at the three gauge stations (MAN, FVA, and OBI) over every 8 days were calculated as $Q_s = SSSC_T \cdot Q_T \cdot k$, where $SSSC_T$ and Q_T are the *SSSC* and *Q* values at date *T*, and *k* is conversion constant of 0.6912. In OBI, we used revised rating curve to calculate *Qs* (Park and Latrubesse Submitted). *Qs* of the Negro River at MAO was estimated as sum of *Qs* at Serrinha and Caracarai, while *Qs* of Tapajós River was calculated at Itaituba station (Figure 5.1). Along both black water tributaries, *Q* and *SSSC* data have been sufficiently collected by National Water Agency of Brazil (ANA) and HYBAM since 1990s to calculate relevant *Qs* annual discharges. Based on *Qs* in 8-day intervals, monthly and annual *Qs* were computed. Floodplain sediment storage along the lower Amazon River in between MAN and OBI were calculated as differences between sum of *Qs* at MAN, MAO and FVA, and *Qs* at OBI. Only washload budget is considered in calculating the channel-floodplain interactions, because floods are related to nearby surface water in the main channel and branches (Junk et al. 1989; Mertes 1994) (Further explanations in the Results section). We also

verified through grain size analyses over channel and different floodplain lakes that suspended sediments at water surface were exhaustively washload.

5.3.4. Incorporating floodplain geomorphology and reaches

Geomorphic map of the study reach was generated by using the following three classes: 1) impeded floodplain, 2) channel-dominated floodplain, and 3) levee complex (Latrubesse 2012; Latrubesse and Franzinelli 2002). Each geomorphic class is digitized mainly based on the interpretation of 30-m resampled SRTM (c-band) aided by high resolution true color images such as Google Earth and Landsat TM data, and field control of some localities. Here impeded floodplain includes rounded lakes covering splay delta that progradates through the breached floodplain channel and also deltaic sediments (Latrubesse and Franzinelli 2002). As mentioned in the introduction, impeded floodplain is playing a major role in trapping sediments.

Floodplain extent and inundation area were mapped to understand their linkages between washload losses over the floodplain. When mapping the floodplain extent, we adopted the geomorphic definition of floodplain (Latrubesse and Park 2017) that includes older geomorphic units of alluvial materials those are not always inundated through typical seasonal flooding (Iriondo 1982). Width of the floodplain is measured as line perpendicular to the Amazon channel centerline touching each limit. At flood stage, overbank diffusive processes happens after the water stage exceeds the banks height. Therefore, information on bank heights integrated with our field observations provide clues on the timing and the location of these processes, which will also illuminate

identifying and characterizing the sediment sinks along the Amazon floodplain with different geomorphic styles. We conducted field surveys between August 25th and September 5th 2015 and June 24th and July 6th 2016 to identify different inundation conditions along the levee complex along the lower Amazon River reach in between Negro confluence and Monte Alegre (≈750 km). We also used vegetation removed SRTM DEM (O'Loughlin et al. 2016) to extract bank elevations at every 90 m longitudinal interval to assess the bank height distribution along the lower Amazon reach. We divided the Amazon River in between Manacapuru and Monte Alegre (≈1,000 km) into four reaches with similar river lengths to assess the heterogeneously distributed sediment sinks linked to the different floodplain geomorphic styles: Reach 1 - Manacapuru to Madeira confluence, Reach 2 – to Parintins, Reach 3 – to Obidos, and Reach 4 – to Monte Alegre (Figure 5.8 and Table 5.5). To compare the geomorphic characteristics (such as floodplain area) between different reaches, we standardized each of the parameters based on the river lengths of each reach.

5.4. Results And Discussion

5.4.1. Suspended sediment concentration data availability and remote sensing model validation

The purpose of this study is to characterize the heterogeneously distributed sediment sinks along the lower Amazon River (over 1,000 km) in relation to the geomorphic styles of floodplain. For that floodplain sediment deposition budgets based

on *SSSC* estimated using remote sensing at gauge stations were first calculated. Therefore thorough validations of the remote sensing models' utility in estimating *SSSC* is an indispensable step. In this section, we assessed the temporal availability of the remote sensing data and validated remote sensing driven *SSSC* data with field data.

Adequate coverage of *SSSC* data in relevant temporal resolution is critical in calculating sediment fluxes of a river basin with distinct hydroclimatic seasonality like in the Amazon (Martinez et al. 2009). Annual temporal coverage (data availability) of MODIS data surpasses the field collected *SSSC* data by 20% at FVA to 42% at Obidos over 14 years (2001-2014) (Figure 5.2a). Throughout this period, the field *SSSC* showed consistently lower annual data availability than MODIS-driven *SSSC*. Field data also presents irregular annual data availability over different years compared to MODIS data, implying its vulnerability to the different inter-annual hydrological conditions. Calculation of the annual coverage is provided in Figure 5.2a caption.

Cross-validation results of MODIS-driven *SSSC* with HYBAM data indicate high coefficient of determination values over gauge stations from different rivers (all R^2>93, total N=932 field samples) (Figure 5.2b). Additionally, remote sensing models are further validated with our field data collected from channel and floodplains along the Amazon River during field works conducted in August 2015 (≈170 km reach in between Manaus-Madeira confluence) and June-July 2016 (≈760 km reach in between Manaus-Monte Alegre) (Figure 5.2c). *SSSC* samples collected in 2016 were used to separately validate the MODIS-driven *SSSC* for the channel (including branches) and floodplain (N=51).

Grain size distribution characteristics of surface sediments over the river and floodplain could vary over different seasons and might affect the surface reflectance (Kirk 1989; Kirk 1994). Previously developed associations between *SSSC* and remote sensing surface reflectance in the Amazon Basin documented washload (silt and clay, grain size <63 μm) as a predominant particle type (Mertes et al. 1993a; Villar et al. 2012), which conforms to the general agreement that washload is the dominant sediments in suspension at surface in the Amazon River system (Filizola and Guyot 2009). Grain size distribution analysis of surface waters samples collected both in Madeira River (≈30 km upstream the confluence) and along the Amazon River are shown in Figure 5.03. Here we confirmed that all surface suspended sediments those were collected close to Q_{peak} were exhaustively silt and clay with almost no sand. During $Q_{falling}$ when suspended sediment tends to become coarser grained in the water column around Obidos (Meade 1985), it is possible that fine sand might occasionally reach the surface. However, the remote sensing model that we used to estimate *SSSC* at Obidos has been separately calibrated for the $Q_{falling}$ using 207 field samples collected during $Q_{falling}$, acquired over 10 year (2000-2012) (Park and Latrubesse 2014). Therefore this potential effect of grain size variations in water surface over seasons on surface reflectance is already accounted in our remote sensing model.

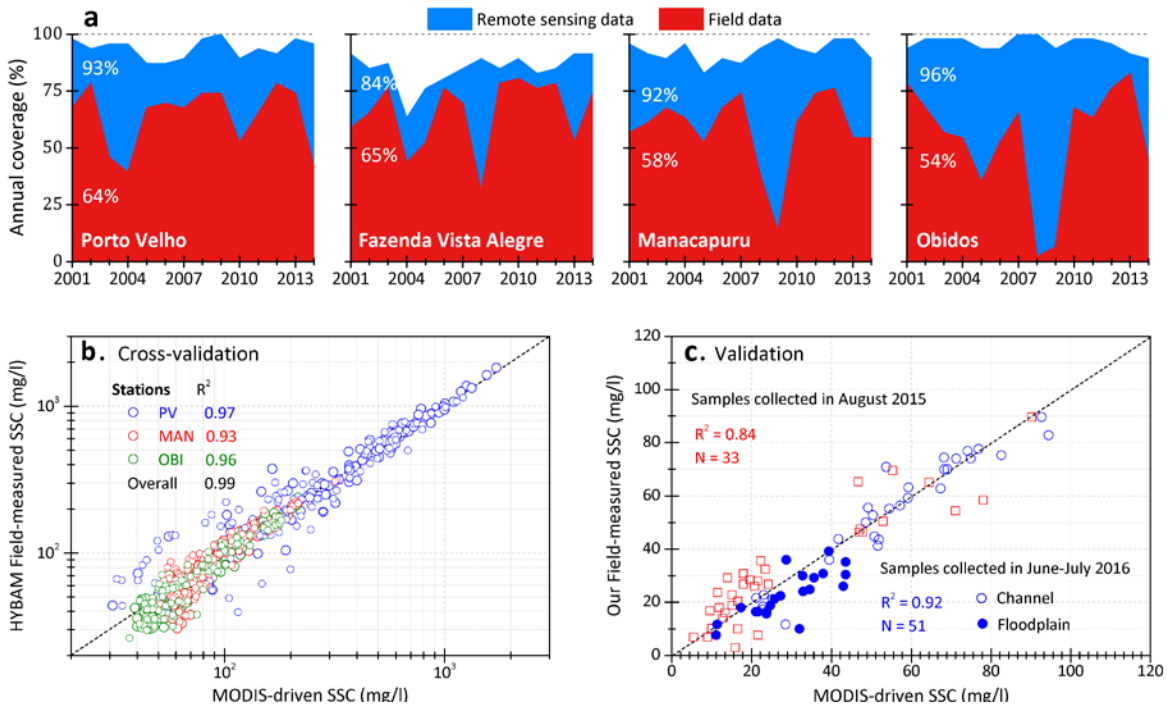

Figure 5.2. (a) Comparison of annual temporal coverages (data availability) between remote sensing and field data necessary to calculate the annual sediment fluxes (Qs). Since MODIS data product is available at every 8 days interval, the annual coverage (blue) is calculated as portion of the available scenes out of total 46 scenes per year. Similarly, HYBAM follows protocol to collect field SSC data at each gauge station on every 1st, 10th, and 20th days in of the month. Thus, the annual field data coverage (red) is calcualted as number of available field samples out of 36 total possible samples per year. Average annual temporal coverage values over 14 years (2001-2014) are also given. Martinez et al. (2009) explained the lower temporal coverage and irregular variability of field data could be due to variability in sampling location, operator reliability or loss of samples. (b) Cross-validation results of the SSC-reflectance calibration models used in this study (Table 5.2) with HYBAM field SSC data and (c) additional validation results using our field SSC data collected during falling and peak limbs of 2015 (reach in between Manaus-Madeira confluence) and 2016 (reach in between Manaus-Monte Alegre). 2016 collected samples are separately plotted between channel (including branches) and floodplain. Samples collected in floodplain channels and black water tributaries are excluded.

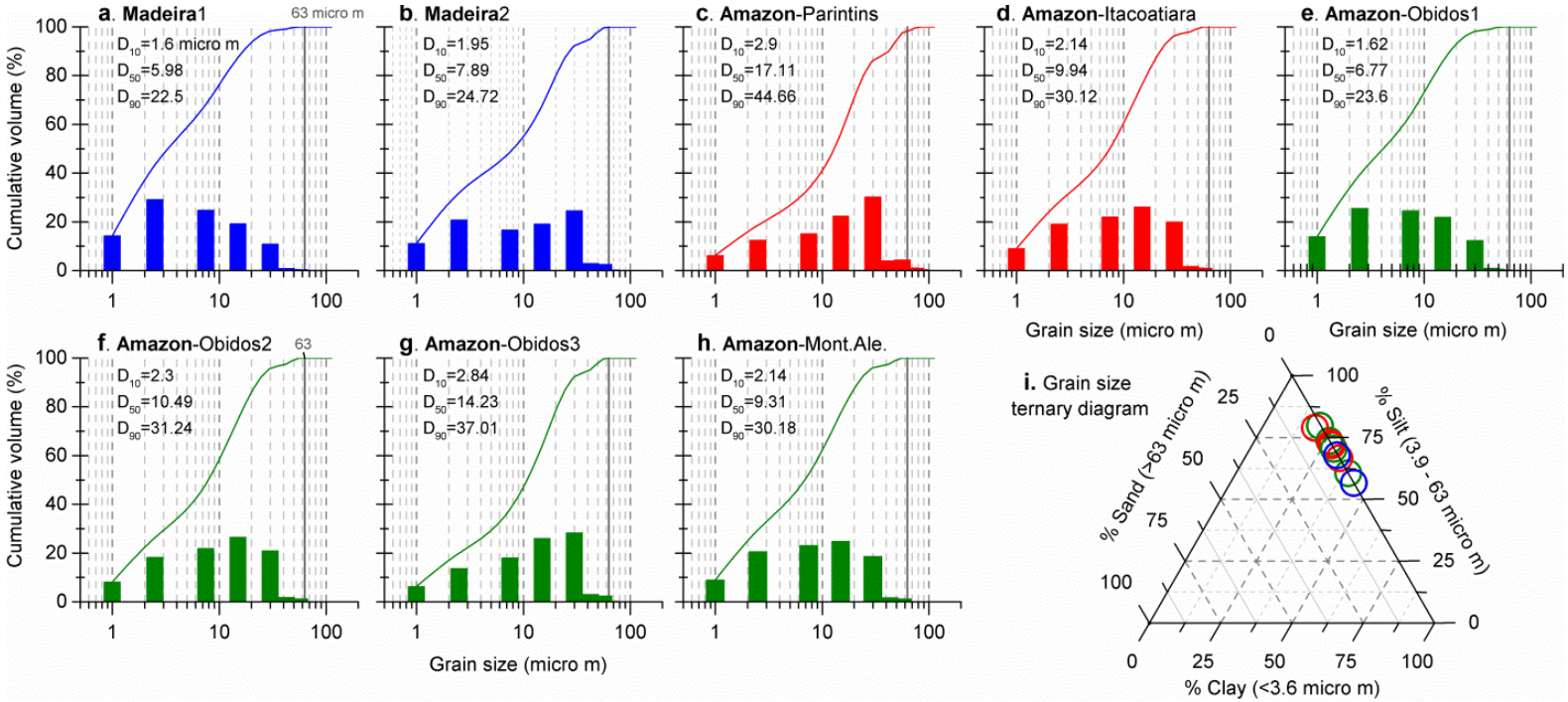
a. Madeira1
63 micro m
D10=1.6 micro m
D50=5.98
D90=22.5
b. Madeira2
D10=1.95
D50=7.89
D90=24.72
c. Amazon-Parintins
D10=2.9
D50=17.11
D90=44.66
d. Amazon-Itacoatiara
D10=2.14
D50=9.94
D90=30.12
e. Amazon-Obidos1
D10=1.62
D50=6.77
D90=23.6
f. Amazon-Obidos2
63
D10=2.3
D50=10.49
D90=31.24
g. Amazon-Obidos3
D10=2.84
D50=14.23
D90=37.01
h. Amazon-Mont.Ale.
D10=2.14
D50=9.31
D90=30.18
Cumulative volume (%)
Grain size (micro m)
i. Grain size ternary diagram
% Sand (>63 micro m)
% Silt (3.9 - 63 micro m)
% Clay (<3.6 micro m)

Figure 5.3. Grain size distribution results of the suspended sediment samples collected using 20 liter buckets during June-July field work in 2016. Locations of the samples: (a) -3.420947°, -58.788019°; (b) -3.503443°, -58.88593°; (c) -2.57016°, -56.608162°; (d) -3.157276°, -58.448858°; (e) -1.938752°, -55.504502°; (f) -1.940992°, -55.503997°; (g) -1.941706°, -55.510791°; (h) -2.462679°, -54.548152°.

5.4.2. Washload fluxes at gauge stations

To maintain consistency on the field data characteristics in terms of basin coverage upstream of the station and data acquisition frequency with recent studies on the Amazon washload discharge ($Qs_{washload}$), we decided to focus on existing stations in calculating $Qs_{washload}$. Among five investigated stations in this study, three of them (MAN, FVA, and OBI) from white water rivers are considered the most important, as they account for most of the suspended sediment transport of the Amazon Basin and gauge more than 80% of basin area at OBI (Filizola and Guyot 2009) (Figure 5.4). The MAN station on Solimões River, which the upstream station area occupies approximately 35% of the Amazon Basin represents the water drainage and sediment loads of the Andean-forelands characterized by high sediment yields (Latrubesse and Restrepo 2014) and central lowlands. Mean annual Q at MAN is around 101,000 m^3/s which is close to half of the total Amazon River Q at OBI (Molinier et al. 1995). Q_{peak} at MAN occurs during June, as other typical reaches along the middle and lower Amazon River. It is also the lowermost gauge station on the Solimões River, about 85 km upstream from the confluence with the Negro River. Our estimated average washload discharge at MAN is 298 Mt/yr calculated over 15 years. In MAN, clear triangle-shaped hysteresis is observed

for both the *SSSC* and $Qs_{washload}$ in relation to *Q* (Figure 5.4). Period of maximum *SSSC* happens in January which coincides with month of the maximum $Qs_{washload}$ of a year (43 Mt/month). However, the minimum *SSSC* occurs during Q_{peak} (June) due to dilution with increased volume of water, while the minimum *Qs* occurs during October (14 Mt/month) when the *Q* is the lowest of the year.

Madeira River is the largest tributary of the Amazon in terms of basin size (≈25% of the Amazon Basin), discharge (MAD ≈ 32,000 m^3/s) and also sediment loads. FVA is the lowermost gauge station on Madeira River located at about 250 km upstream from the confluence with the Amazon River, integrating over 95% of its basin area. In FVA, *Q* reaches its peak usually during April, about two months prior to the peak of the Amazon River (Figure 5.1b). We used MODIS calibration model in PV to estimate *SSSC* at FVA (Table 5.2), because there is no major input or loss of sediments between the two stations. Hydrological and sedimentological regimes in this river are, in general in phase with each other in that, normally mean monthly *SSSC* and *Qs* are the lowest during August to October when *Q* is also the lowest of year. Also the maximum $Qs_{washload}$ of 33 Mt is transported during March, usually one month before the Q_{peak} (Figure 5.4). In contrast, as low as only 1.5 Mt of $Qs_{washload}$ is being transported during September, presenting a huge seasonally varying contribution of washload to the Amazon River. Our estimated total annual $Qs_{washload}$ of the Madeira River at FVA is 171 Mt/yr.

OBI gauge station representing the lower reach of the Amazon River is located immediately upstream the confluence with Tapajós River (Figure 5.1). It is the lowermost

gauge station of the Amazon River, which the hydrometric data has been systematically collected over a long period (since early 1990s) that encompasses nearly 80% of the entire basin area, as well as discharge (Filizola and Guyot 2009). Located at ≈700 km upstream from the Atlantic Coast, this station is also considered the lowermost station in the Amazon not affected by the tidal effects (Kosuth et al. 2009). Seasonal behaviors of the *SSSC* and *Q*, and in turn *Qs* are altered from MAN mainly due to the influence from the two largest tributaries: Negro and Madeira Rivers. Lowered mean monthly *SSSC* during the $Q_{falling}$ season (August-September) at OBI compared to MAN perhaps should be the most obvious change (Figure 5.04), which is related to the different hydrological seasonal patterns of the two tributaries in between the stations. During this period of the year, Amazon River's *Q* contribution from the Negro and Madeira Rivers are close to their highest and the lowest, respectively (Figure 5.1b and 5.4). Increased black water input from the Negro and low input of muddy water from Madeira during this season results in dramatic decrease in *SSSC* at OBI.

When calculating the $Qs_{washload}$, we used the revised rating curve at Obidos (Park and Latrubesse Submitted). The maximum $Qs_{washload}$ discharging month has been shifted from January at MAN to March at OBI (i.e. 64 Mt/month), which coincides the *Qs* peak at FVA. According to Richey et al. (1986) based on the Carbon in the Amazon project (CAMREX), *Qs* peak was considered to occur in February. However considering that change of the mean monthly *SSSC* from February to March (i.e. 132 to 114 mg/l) is not much of difference (-8.6%), while increase of the mean monthly *Q* from February (171,000) to March (201,000 m^3/s) is more dramatic (+17.5%), we expect that our result

is more relevant. Moreover CAMREX had a limited number of samples with *SSSC* acquisition at approximately every four months, while our washload discharge is calculated based on field and remote sensing data systematically acquired in a denser temporal scale to covers entire seasons over a sufficiently long period (2001-2015). Our estimated annual washload flux at OBI is 403 Mt/yr. As seen in this section, monthly $Qs_{washload}$ transport patterns along the Amazon River are function of both *SSSC* and *Q* seasonal dynamics from different tributaries.

Washload fluxes are also calculated in the two black water tributaries along the Amazon River: Negro and Tapajós Rivers (Figure 5.5). In these rivers, monthly and annual *Qs* are estimated solely based on field data because *SSSC* could not be estimated efficiently from remote sensing over black waters (Park and Latrubesse 2015). At the three stations used to calculate $Qs_{washlaod}$, HYBAM have already collected sufficient *Q* and *SSSC* data over time in order to relevantly estimate the annual washload budgets (Figure 5.1 and Table 5.1). In MAO, *Q* and *SSSC* data are not regularly collected and only available episodically, due to the backwater effect (Meade et al. 1991). Hence we calculated $Qs_{washload}$ individually at the two upstream stations: Serrinha on Negro River and Caracarai on Branco River (a tributary of Negro). They were added together to retrieve the $Qs_{washload}$ of Negro River at MAO assuming the sediment loss to the floodplain will be minimal downstream from the two stations. Although $Qs_{washload}$ budgets of these black water tributaries were very low as they drain dominantly cratonic regions, they show distinct seasonal variations with the highest $Qs_{washload}$ discharges

during June-July and February for the Negro and Tapajós Basins, respectively. Annual $Qs_{washload}$ of Negro and Tapajós Rivers are calculated as 5.4 and 4.1 Mt/yr, respectively.

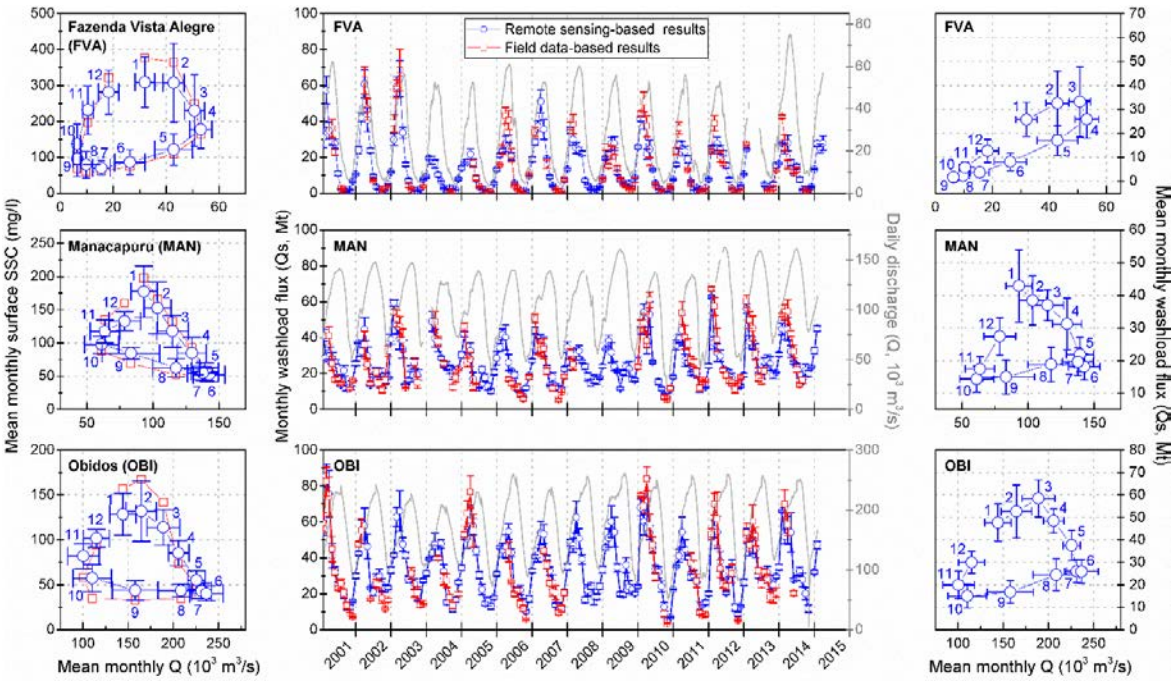

Figure 5.4. Seasonal variability of suspended sediment concentration (SSC, left) and fluxes (Q_s, right) in relation with monthly water discharge, and time series monthly Qs (center) are plotted at three gauge stations along the white water rivers: Fazenda Vista Alegre (FVA), Manacapuru (MAN) and Obidos (OBI). Field data-based calculations of SSC and Qs are also provided (red) using every available field data from HYBAM, which presents high correlations with our remote sensing-based estimates. Monthly average and variability (standard deviation) of sediment and discharge values are plotted in order to announce their seasonal tendency and visually enhance the comparison between months. Numbers in plots indicate month.

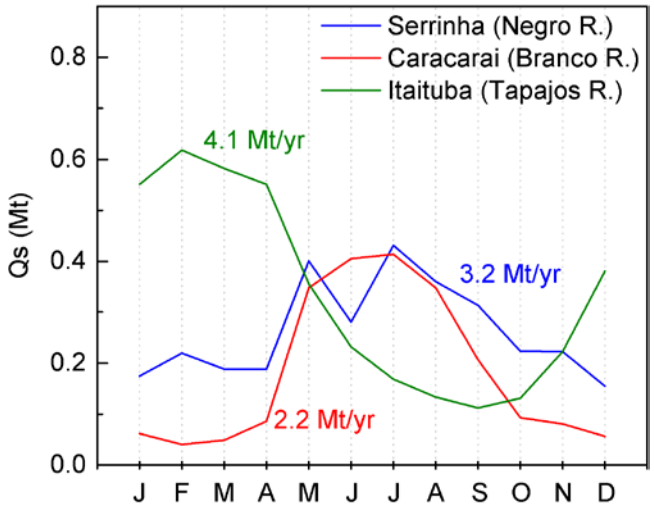

Figure 5.5. Mean monthly suspended sediment fluxes of black (Negro and Branco Rivers) and clear (Tapajos River) water tributaries. Total annual sediment fluxes at each station are sum of monthly fluxes. These calculations were made based on every available field SSC and Q data from HYBAM. SSC sample sizes are provided in Figure 5.1.

Table 5.3. Summary of inter-annually (2001-2015) averaged *Qs* budgets estimated in this study

Station (code)	$Qs_{washload}$ (Mt) Max. month (budget)/Min.	$Qs_{washload}$ (Mt) Annual budget
FVA	Mar (33)/Sep (1.5)	171
MAN	Jan (43)/Oct (14)	298
OBI	Mar (58)/Oct (15)	403
ITA	Feb (0.6)/Sep (0.1)	4.1
MAO	Jul (0.8)/Dec (0.2)	5.4
-SER	Jul (0.4)/Dec (0.2)	3.2
-CAR	Jul (0.4)/ Feb (0.04)	2.2

[a] Includes $Qs_{washload}$ of Tapajós and Negro Rivers.

5.4.3. Floodplain suspended sediment sinks along the lower Amazon

By differencing the mean monthly $Qs_{washload}$ curves of Obidos by combined $Qs_{washload}$ of the Amazon River upstream (i.e. Qs_{MAN}+Qs_{FVA}+Qs_{MAO}), suspended sediment loss over floodplain along the lower Amazon reach in between Manacapuru and Obidos is determined.

Fine suspended sediment, i.e. washloads were only considered when estimating floodplain suspended sediment budgets. According to Bouchez et al. (2011), vertical profiles of suspended sediment concentration at Manacapuru, Foz Madeira (immediately upstream from the confluence) and Obidos during March and June were relatively constant from the water surface to approximately 10 m in depth. In March, hydrological connectivity between channel and floodplain is usually initiated in the lower Amazon through channelized flows (and then overbank diffusion within a few weeks) (Park and Latrubesse 2017, Submitted). These floodplain influxes are maintained until June (Q_{peak}). During this period (after the floodplain connectivity), water stage range until its peak is less than 4 m, even in case of Obidos where the water stage seasonal variability can be up to 9 m. That is, water stage above 4 m from the mean elevation of the levees in the lower Amazon is hardly reached and thus, it is concluded that only fine sediments (washloads) are exclusively transferred to floodplain during the Q_{rising}. Our field observations and grain size distribution analysis results from the surface water samples collected in the several floodplain lakes along the Amazon also indicate the lack of sandy materials and presence of fine suspended sediments in floodplain (Figure 5.6).

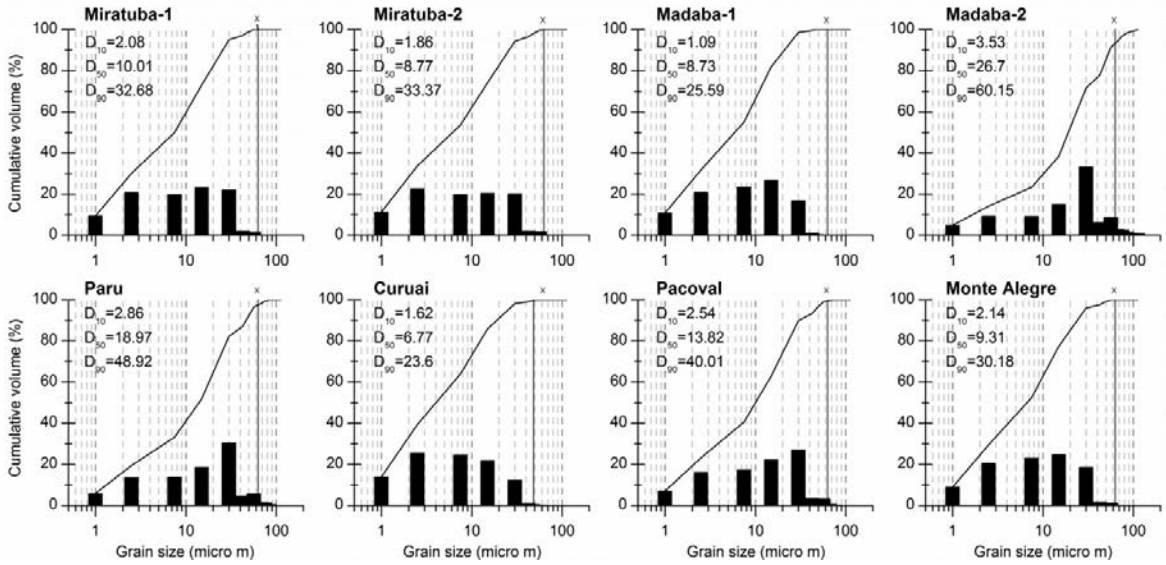

Figure 5.6. Grain size distribution results of the suspended sediment samples collected using 20 liter buckets in the Amazon River floodplain during June-July field work in 2016. Location of the floodplains is in Figure 5.8.

Channel lateral migration rate was also considered that can potentially introduce anomalies on the floodplain sediment budgets by triggering erosion of bank or creation of additional connections to the large floodplain lakes beyond the banks by generating levee breaching, enlarging floodplain channels and developing splay delta. Historical channel migration rates assessed along the 1,000 km reach along the lower Amazon is 0.0064 ch-w/yr, which is much smaller than that of the entire Amazon River main channel (0.01 ch-w/yr) (Latrubesse et al. 2017) or even lower than some alluvial reaches of the Amazon tributaries draining cratonic settings (0.0075 ch-w/yr, such as Negro, Tapajos, or Xingu Rivers) (Constantine et al. 2014). Therefore the banks confining the lower Amazon River is very stable and have been considered persistent over decades, and thus keeping our estimated *Qs* valid over decadal scale applied in this study.

5.4.3.1. Mega-scale assessments along the reach in between Manacapuru and Obidos

Our results indicate that net sedimentation in floodplain starts in late $Q_{falling}$ (September-) then the highest rate of floodplain sedimentation takes place in January (≈19.7 Mt) when Qs_{MAN} is also the highest of the year (Figure 5.7b and d). High rate of washload loss is maintained until March when $Qs_{washload}$ both at FVA and OBI are on their peaks. Net monthly washload loss to floodplain gradually decreases over Q_{rising} and in Q_{peak} when water budget balance between channel and floodplain is close to the equilibrium condition, channel-floodplain hydrologic interactions slow down and in turn washload is no more lost to floodplain (Figure 5.7d). In June when both the *Q* and water levels are at their peaks, strong backwater effect blocking inflow from the Madeira to the Amazon River dramatically decreases both the *Q* and in turn $Qs_{washload}$ at FVA (Figures 5.1b and 5.7b). Even after June at Obidos, throughout $Q_{falling}$ (from July to October) $Qs_{washload}$ contribution of Madeira to the Amazon is as low as 3 Mt/month on average. Correspondingly, during $Q_{falling}$, only July and August present net gain of washload, in very low degrees (1.3 and 2.3 Mt/month, respectively) (Figure 5.7d). The inter-annual net gain of washload was 3.6 Mt/yr. Overall, our estimation of the mean annual net loss of washload to floodplain in this reach is 76 Mt.

Similar mass balance approach has been used to estimate floodplain sedimentation rates by Filizola and Guyot (2009) using the *Q* and *SSSC* data collected at MAN (*SSSC* N=47), FVA (N=43), and OBI (N=53) during 1980s-2000. They calculated mean monthly *Qs* and estimated the annual sedimentation budget over the floodplain in

the same reach along the Amazon to be around 160 Mt. According to their analysis, however contrasting with ours, major loss of washload occurred between March and October, which the period encompassing the second half of Q_{rising} (i.e. March-early June) and the entire $Q_{falling}$ (Figure 5.7a and c). We consider our results are relevant due to the following reason. Most importantly, the period that the net loss of washload over to the floodplain coincide with Q_{rising}, when the river water level rises to make hydrologic connections to floodplain whether through channelized or overbank diffusive flows (Park and Latrubesse 2017). Previous studies on sediment budget in the lower Amazon also support our results. For example, Dunne et al. (1998b) considered only Q_{rising} in calculating sediment influxes of floodplain in their reach-scale mass balance analysis. Bourgoin et al. (2007) also drew conclusion that net sedimentation in the Curuai floodplain is positive only during November to June, i.e. during Q_{rising}. We consider that Qs_{MAN} during $Q_{falling}$ (June-October) by Filizola and Guyot (2009) is overestimated (Figure 5.7a).

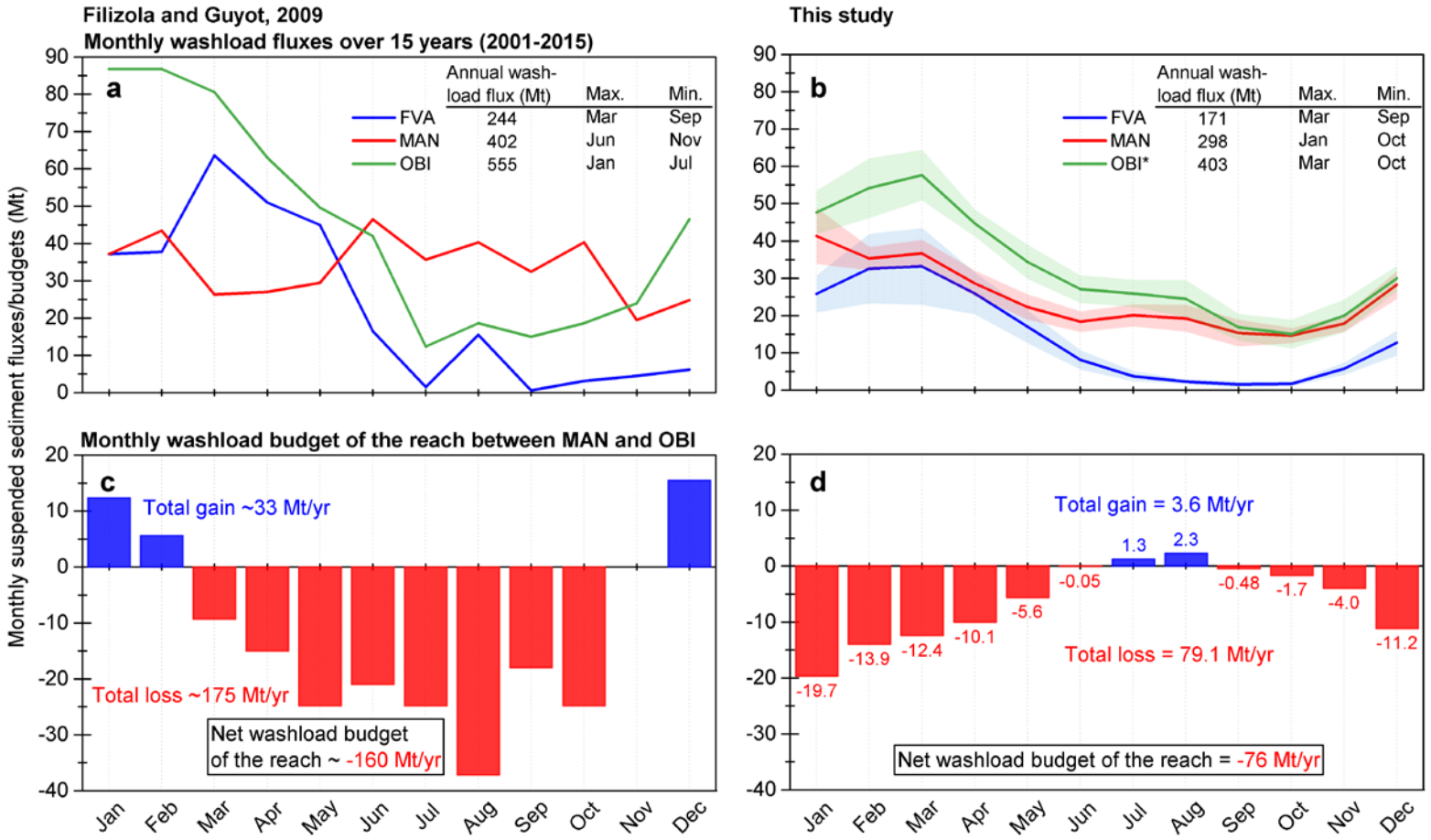
Filizola and Guyot, 2009
Monthly washload fluxes over 15 years (2001-2015)
This study
a
b
c
d
Annual wash-load flux (Mt)
Max.
Min.
FVA 244 Mar Sep
MAN 402 Jun Nov
OBI 555 Jan Jul
FVA 171 Mar Sep
MAN 298 Jan Oct
OBI* 403 Mar Oct
Monthly suspended sediment fluxes/budgets (Mt)
Monthly washload budget of the reach between MAN and OBI
Total gain ~33 Mt/yr
Total loss ~175 Mt/yr
Net washload budget of the reach ~ -160 Mt/yr
Total gain = 3.6 Mt/yr
Total loss = 79.1 Mt/yr
Net washload budget of the reach = -76 Mt/yr
-19.7
-13.9
-12.4
-10.1
-5.6
-0.05
1.3
2.3
-0.48
-1.7
-4.0
-11.2
Jan
Feb
Mar
Apr
May
Jun
Jul
Aug
Sep
Oct
Nov
Dec

Figure 5.7. Monthly suspended sediment fluxes at FVA, MAN, and OBI gauge stations and its floodplain deposition budget of the reach in between the Madeira confluence and OBI. Results from Filizola and Guyot (2009) (left, a and c) are compared with ours (right, b and d). (a) Mean monthly suspended sediment fluxes and variability at FVA, MAN, and OBI are calculated over 15 years (2001-2014). Monthly net sediment budget of the reach (after interaction with floodplains) in between MAN and OBI are calculated by differences in their monthly budget. Annual Qs of Negro River at MAO (5.4 Mt/yr) is included in the calculation.

5.4.3.2. Heterogeneous spatial distribution of floodplain sediment sinks: Reach-by-reach analysis

To map the heterogeneously distributed floodplain sediment sinks along the lower Amazon, we divided approximately 1,000 km reach between Manacapuru and Monte Alegre into four reaches (Figure 5.8). We used important geomorphic break-points such confluence or size of floodplain when dividing the reaches and the reach lengths span 200 km (reach 3) to 325 km (reach 2). We incorporate inundation dynamics, *SSSC* distribution patterns and geomorphic styles with spatial distribution of sediment sinks.

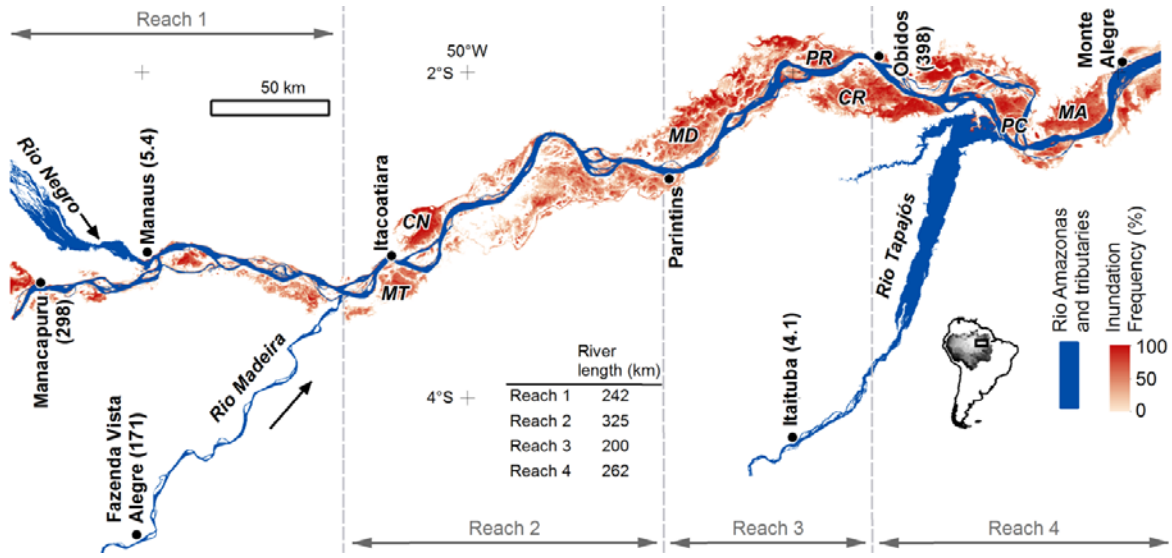

Figure 5.8. Map of the Lower Amazon River and inundation frequency over floodplain. Gauge stations used in this study are also shown with their annual fluxes (Mt/yr) given in parentheses next to each station. Floodplain names are abbreviated: Miratuba (*MT*), Canacari (*CN*) Madaba (*MD*), Paru (*PR*), Curuai (*CR*), Pacoval (*PC*), and Monte Alegre (*MA*).

When investigated floodplain width, we detected generally downstream widening patterns (Figure 5.9a). Average widths of reaches gradually increase downstream from 18.6 km in Reach 1 to 40.7 km in Reach 4. Width of floodplain is not only related to the channel lateral activity and inundation dynamics of the river, but also to the structural features of the region. In Reach 1, neotectonic lineaments those are generally in NE-SW and E-W directions confining the fluvial belt are documented by Latrubesse and Franzinelli (2002). They mention that the fluvial belt can be locally narrow or wider oscillating between 7 to 20 km controlling the location and appearance of the alluvial plain in this region. In Reach 2-4, floodplain lies over “trough” confined by Guyana and

Brazilian shields, however the fluvial belt becomes larger as well as floodplain extents. Although downstream widening patterns were observed, width itself alone does not efficiently explain the distribution of sediment sinks, because as stated above it can be determined by local geologic controls and also development of water-saturated floodplain was not necessarily related to the floodplain width (Mertes et al. 1996a).

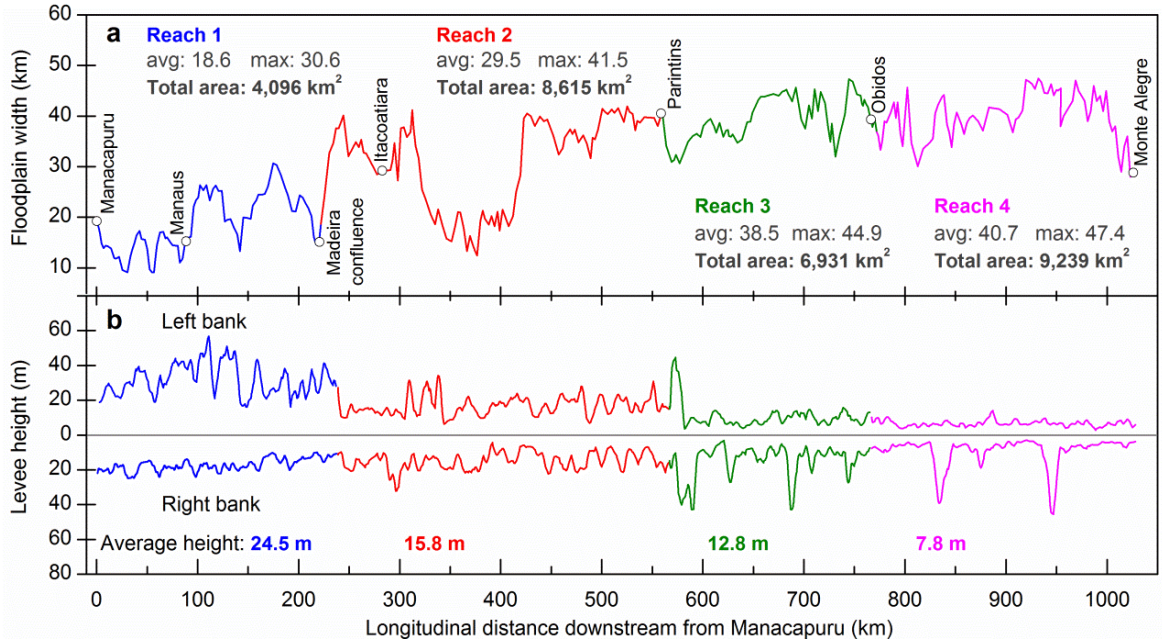

Figure 5.9. Floodplain width (a) and bank height (b) longitudinally downstream along the lower Amazon are calculated.

Water-saturated floodplain area may indicate the space availability to accommodate sediments which generally increase downstream direction in the lower Amazon River. This water-saturated floodplain, that is geomorphologically "incomplete" acts as sediment sink and can spread over thousands of kilometers in length and tens of

kilometers in their widths (Latrubesse 2015). When we mapped the inundation extents and their frequency, both of the extents of the impounded water during the dry season (when frequency=0%) and floodplain area under the influence of seasonal flooding became larger downstream direction from reach 1 to reach 4 (Figure 5.10). Inundated area divided by the length of each reach indicates the size of flood extent (km^2) per unit km, which then enables the comparison between different reaches (Figure 5.11) (as like in Dunne et al. 1998b). The difference in the inundation area was notable between different reaches. As expected, Reach 4 present the largest flood extent per unit km, with the highest extent achieved in June. Other reaches, with inundation area per unit km less than that of Reach 4, achieved their inundation area peak during May, due to the lag time of the Amazon flood wave transmission.

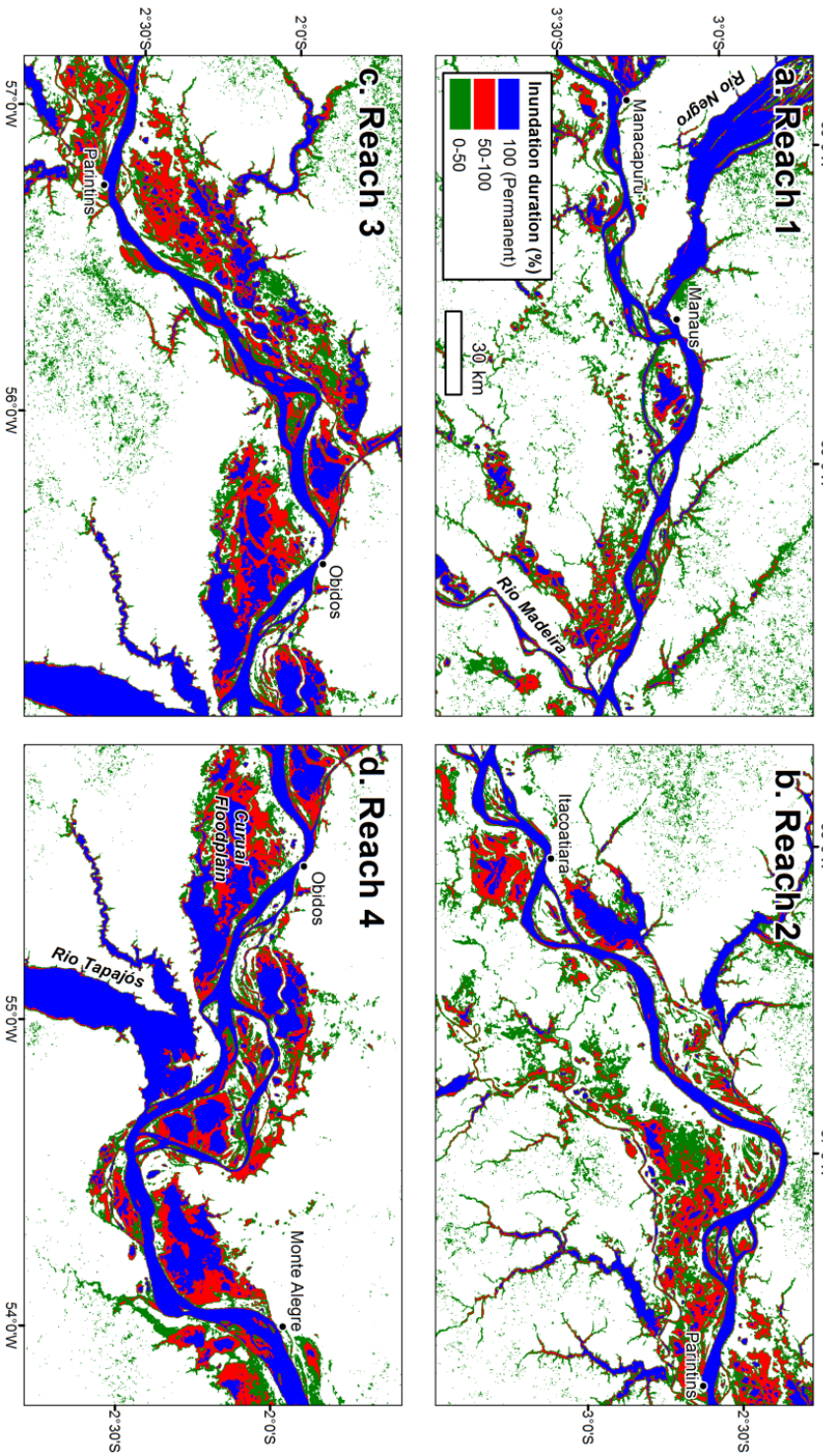

Figure 5.10. Inundation frequency (0-100 %) map along the lower Amazon (Reach 1-4). All inset maps are in the same scale.

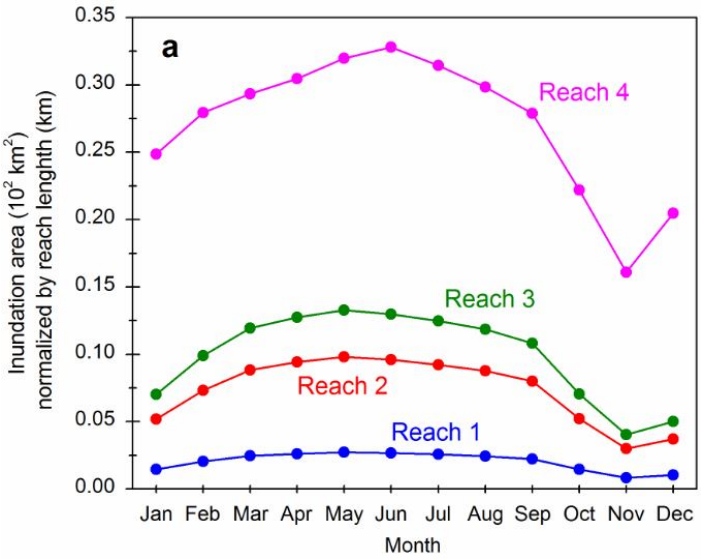

Figure 5.11. Total inundated area of each month for each unit is divided by total length of the reach, in order to derive area (km^2) per unit km, that enables the comparison between reaches.

In reach 1, there is not sufficient space accommodation for the sedimentations along the left bank, as it is confined by sedimentary rocks along the left bank. Black waters draining the craton directly joins the Amazon main channel without being impounded in floodplain (Park and Latrubesse 2015). Although Rozo et al. (2012) mentioned the high stability of the channel banks in reach 1, right banks and large islands in this reach are mostly channel-dominated floodplain that are mainly formed by the lateral migration of anabranching channels (Figure 5.12a), not favoring much of the overbank diffusive sedimentations. According to the alluvial plain evolution model of this reach by Latrubesse and Franzinelli (2002), this channel-dominated floodplain became active through reworking impeded floodplain that is developed during the earliest stage of the late Holocene. This indicates that floodplain in Reach 1 is relatively older

and is at the later stage of dynamic equilibrium compared to the downstream reaches (Reach 2-4) where water-saturated floodplain is extensively developed.

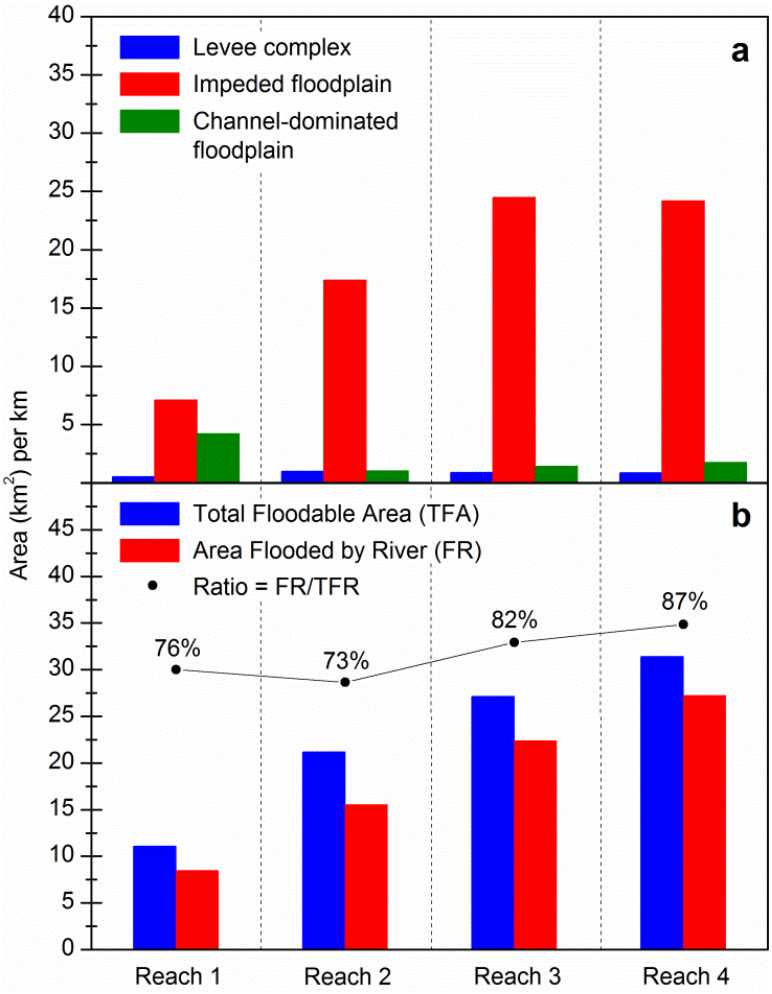

Figure 5.12. (a) Composition of floodplain geomorphic units for each reach along the lower Amazon. (b) Floodable area and those flooded by the river, as well as ratio between the two are presented. Area (km^2) per unit km is calculated for comparison between reaches.

Downstream the Madeira confluence (Reach 2-) are where the wider water-saturated floodplain start to appear (Figures 5.08 and 5.10). In contrast to the Reach 1, impeded floodplain and its component rounded lakes are the dominant floodplain style along the Reach 2-4. The impeded floodplain that stores the water and sediment delivered from the river is the substantive definition of active sediment sinks along the Amazon River. Here, overbank diffusion is the process delivering majority of water and sediments influxes (Dunne et al. 1998b; Rudorff et al. 2014a). When we compared the area of the impeded rounded lakes per unit km between the four different reaches, it showed a downstream increasing trend, while that of the levee complex remained relatively constant throughout the reaches (Figure 5.12a). Channel-dominated floodplain decreased from Reach 1 to 2, and remained constant through Reach 2-4. That is, floodplain style that is capable to store and trap sediment increase downstream and this could provide implications of up- to downstream transfer of sediment infilling processes, a nonlinear system response to the late Holocene climatic change stated in Latrubesse and Franzinelli (2002).

Although, increase in impeded floodplain is related to the potential sediment accommodation of floodplain, to understand the distribution of modern sediment sinks, it is necessary to assess the present day flooding dynamics. For this, two variables are considered for reaches: 1) total floodable area (TFA) and 2) flooded area by river (FR) (Figure 5.12b). Total floodable area is the water extent over floodplain that contains also the different water sources other than white water from river, e.g. black water from local tributaries draining uplands and clear water from rainfall. Therefore sediment laden water

(muddy water from the river) extent from the river is further classified, which contributes to the floodplain sedimentation. Both the TFA and FR showed increasing trend downstream, as absolute area of water-saturated floodplain increase. However, we also detected that the ratio between FR and TFA also increased downstream (from 76% at Reach 1 to 87% at Reach 2), showing that areal contribution of water sourced from river out of total floodable area increased downstream. This indicates that the influence of the river inflow over floodplain inundation becomes larger and thus more washload will be potentially accumulated in the downstream reaches.

Field-calibrated *SSSC* maps are used to further characterize the sedimentary sinks, because they enable the identification of the sedimentation hotspots over floodplain. By using the *SSSC* maps averaged over 15 years (2001-2015), we show a reach-by-reach surface sediment distribution patterns over the complex mosaic of different geomorphic units (Figure 5.13). We select two months to show, i.e. March and June, when *Qs* and *Q* at Obidos is the highest of the year, respectively. Here, the impact of sediment inputs from the river toward the floodplain is clearly detectable. Also, larger impounded water area with generally higher *SSSC* can be observed downstream (i.e. from Reach 1 to Reach 4) for both months (Figure 5.13). In March when Amazon River's *SSSC* is typically highest of the year, *SSSC* in floodplain in Reach 1 and 2 rarely increase above 100 mg/l. However, in floodplain lakes along the reach 3 around Obidos and reach 4 the *SSSC* are generally above 120 mg/l even reaching 150 mg/l in some parts of the Curuai Lake. In June, along with the maximum discharge in river, typically floodplain also stores water at its maximum capacity. During this period good parts of floodplain lakes in Reach 1 and

2, *SSSC* is below 50 mg/l (except for Miratuba Lake which is flooded by water from Madeira), and even below 30 mg/l for the Canacari Lake on average, the largest floodplain lake along Reach 1 and 2. In contrast, *SSSC* of good parts of the lakes in Reach 3 and 4 are over 60 mg/l, and even reaching close to 100 mg/l in Monte Alegre Lake during this period.

Thus, *SSSC* over floodplain clearly presents higher values over a larger area in the downstream reaches. This can be considered as a direct indicator for the spatial distribution of sediment sink hotspots, because they are susceptible to sedimentation in floodplain. Inferred from the velocity profiles collected linearly in different floodplains along the lower Amazon using ADCP around Q_{peak}, impounded waters in floodplain were practically stagnant and were not capable to move or keep fine sediments in suspension but to deposit there. The depth-averaged velocities measured in different floodplain lakes over Reach 1-4 ranged from 0.022 to 0.186 m/s with average velocity of entire floodplain of 0.12 m/s (Figure 5.14) (Table 5.4). The flows did not have specific flow directions but were scattered over all directions. The surface temperature of this impounded lake can increase to 29.76 °C (in Curuai Lake), while it was 28.06 °C in the Amazon River around Obidos on the same day (July 4th, 2016).

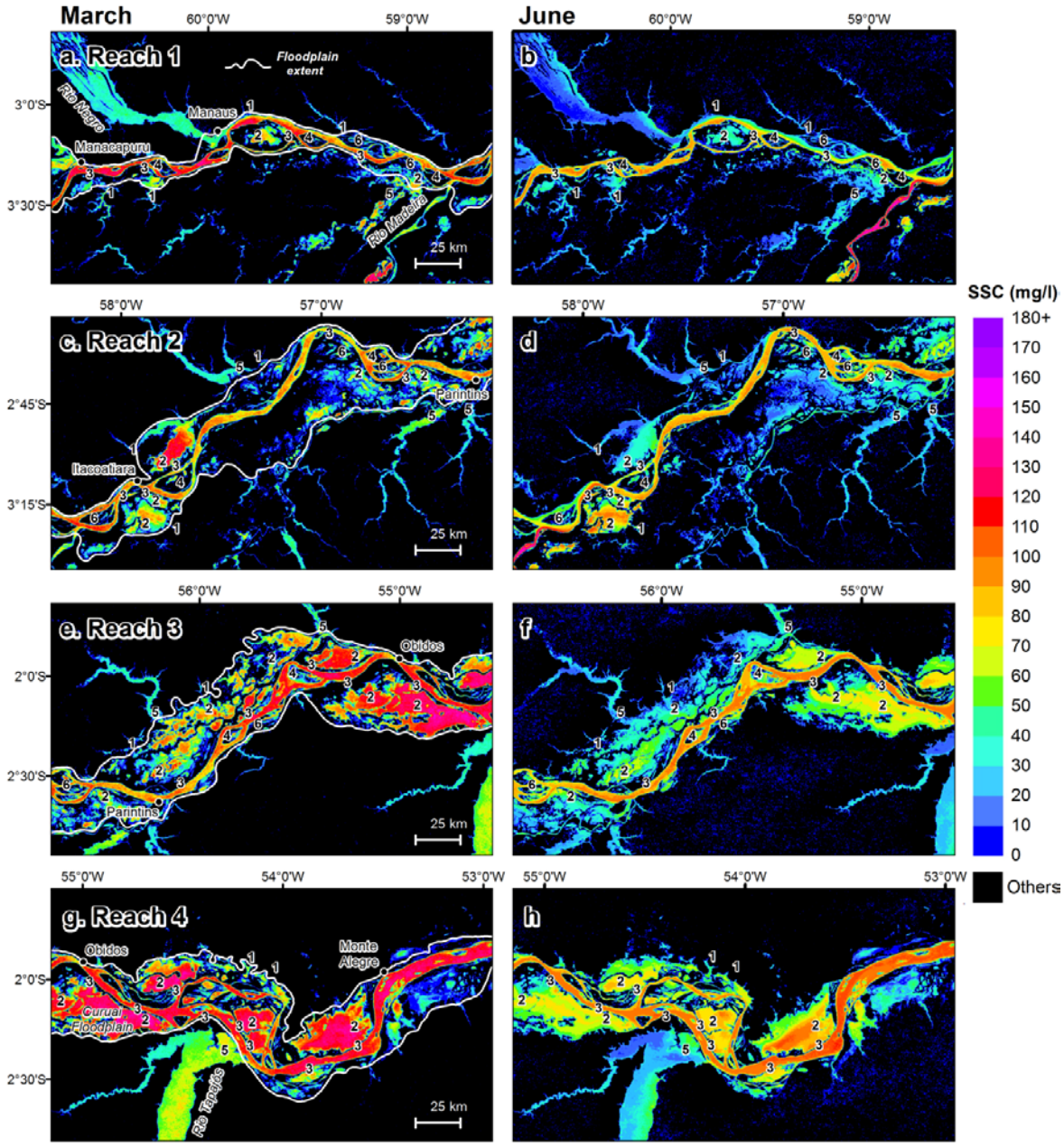

Figure 5.13. Monthly surface sediment concentration maps averaged over 15 years (2001-2015) along the lower Amazon (Reach 1-4) (Park and Latrubesse, 2014). All inset maps are in the same scale. Floodplain in the lower Amazon is mosaic of different geomorphic units and each geomorphic unit is indicated as numbers following the classification by Latrubesse (2012): (1) blocked valley, (2) impeded rounded lake, (3) levee complex, (4) island, (5) deltaic impeded lake, and (6) channel-dominated floodplain units.

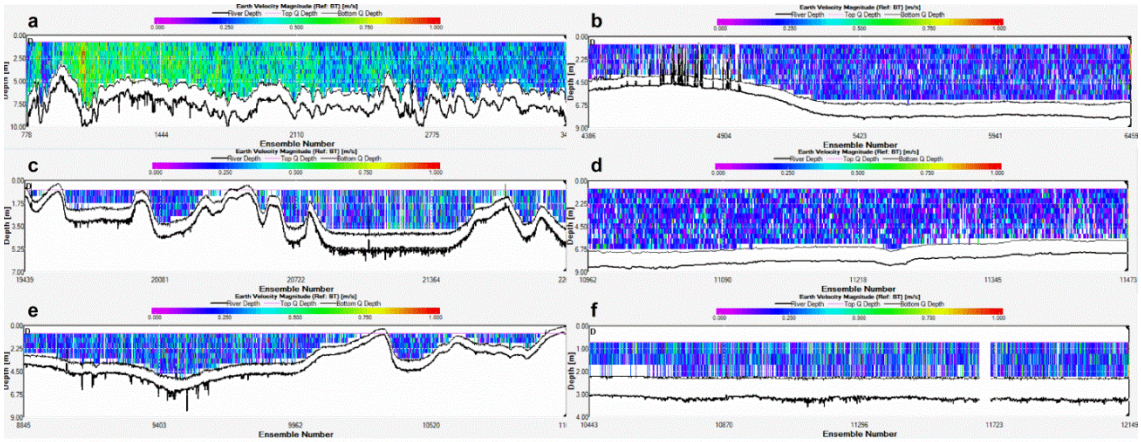

Figure 5.14. Collected ADCP profiles in the floodplain lakes along the Amazon during June 28th-July 6th, 2016. Floodplain lakes: (a) Miratuba, (b) Canacari, (c) Madaba, (d) Paru, (e) Curuai, and (f) Monte Alegre

Table 5.4. Summary of ADCP data collected in floodplain along the lower Amazon (Figure 5.14).

Reaches	Floodplain lakes	Date	Survey length (m)	Average velocity (m/s)	Average depth (m)	Temperature (°C)
Reach 2	Miratuba	June 28th, 2016	3620.8	0.173	8.99	29.26
	Canacari	July 6th, 2016	1554.7	0.071	7.98	32.78
Reach 3	Madaba	July 4th, 2016	1903.4	0.123	5.21	29.86
	Paru	June 28th, 2016	546.7	0.022	7.17	31.42
Reach 4	Curuai	July 4th, 2016	1514.9	0.117	0.9	29.76
	Monte Alegre	July 2nd, 2016	1155.7	0.186	3.18	30.48

As noted earlier, overbank diffusion is responsible for the majority of the sediment delivered in the floodplain. In June around Reach 3 and 4, channel-floodplain connections through overbank diffusion, which can spread longitudinally over a few kilometers is notable, especially along the Curuai floodplain (Figure 5.13) (Park and Latrubesse 2014). This direct observation of overbank process during the Q_{peak} in upstream reaches is, however less pronounced with wide levee complex still extensively exposed. When we further assessed the bank height, downstream decrease in bank height

is also detectable (Figure 5.09b). The difference in average bank height downstream was quite remarkable, that average bank height in Reach 1 is 24.5 m while that of Reach 4 is 7.8 m. Given that the overbank diffusion is controlled by the levee height, generally lowering bank height downstream along the Amazon River indicate the increased susceptibility to the overbank flooding, hence more suspended sediment influxes in floodplain.

Table 5.5. Floodplain morphometric characteristics of the reaches

	Longitudinal length (km)	Average width (km)	Average bank height (m) [a]	Total floodplain extent (km^2)	Total floodable area (km^2/km)[b]	Area flooded by river (km^2/km)[b]	Impeded floodplain area (km^2/km)[b]
Reach 1	242	18.6	24.5	4096	11.1	8.4	8.5
Reach 2	325	29.5	15.8	8615	21.2	15.5	17.4
Reach 3	200	38.5	12.8	6931	27.1	22.4	24.5
Reach 4	262	40.7	7.8	9239	31.4	27.2	24.2

[a] calculated from SRTM

[b] value per unit km allows comparison between different reaches

5.4.3.3. More sedimentary sinks downstream?

Downstream of Obidos in the Amazon River, gauge stations are lacking the development of discharge rating curves due to the tidal effect. From geomorphologic and sediment budgetary perspective, this might be problematic to estimate the total *Qs* export of the basin to the ocean. Because vast floodplain system of the Amazon River ends even

~250 km further downstream of Obidos, around Monte Alegre (MAL) (Figure 5.08) and that Nittrouer et al. (1995) estimated about 30% of suspended sediment could be further deposited in the reach between Obidos and mouth. Moreover it has been recently reported that about 20 Mt of fine sediment from the Amazon River is deposited at rias valleys of Tapajos and Xingu Rivers annually (Fricke et al. 2017). Downstream MAL are terraces dominated older riverine landscapes, where we assume that the sediment loss to floodplain is negligible.

The water-saturated floodplain in this reach between OBI and MAL is such immense that the width of the floodplain is even larger than that of the reach between MAN and OBI by more than 10 km on average (Figure 5.9a). Floodplain area of this reach (OBI-MAL) is huge as much as 75% of that for the MAN-OBI reach. Given that longitudinal river distance of this reach is only 34% of that of reach in between MAN-OBI, it is not difficult to presume the extensive spatial scale of the floodplain along this relatively short reach, and thus the role as sedimentary sink can be substantial. To quantify *Qs* downstream OBI using the approach used in this paper, however there are several limitations. First, it is difficult to estimate the *Q* around MAL, because *Q* should not only be under the strong backwater effect from the ocean, but also substantially influenced by the dynamic connectivity processes with huge surrounding floodplains during Q_{rising}. Since the timing of connectivity with different floodplain units and their individual seasonal storage capacities are not well-known as well as backwater impacts from the ocean, simple rating curve method to estimate *Q* from the water level downstream OBI is yet unsuitable. Moreover tidal impacts alter the *SSSC* vertical

distribution in the water column (toward non-uniform vertical distribution of washloads) (Kosuth et al. 2009) that will add further complications toward the washload budgeting in this place. Thus, to estimate the total *Qs* of the Amazon basin, rather than empirical approaches based on series of *Q* and *SSSC* data (as in this study), modeling approach incorporating the physical dynamics of both the discharge and suspended sediments should be necessary.

5.5. SUMMARY AND CONCLUSION

In this chapter, floodplain sediment storage budget is examined along the 1,000 km reach of the lower Amazon River based on extensive sets of remote sensing data and field measurements. Incorporating the washload discharges at gauge stations at the main channel and major tributaries, we analyzed the roles of vast floodplain on the Amazon River seasonal variability in water and sediment discharges. Annual washload accumulation rate on floodplain along the reach in between Manacapuru and Obidos is estimated to be 79 Mt over inter-annual average. Period that the net loss over to the floodplain of washload coincide with Q_{rising}, when the river water level rises to make hydrologic connections to floodplain. In Q_{peak} when water budget balance between channel and floodplain is in an equilibrium condition (as floodplain becomes totally water-saturated), channel-floodplain hydrologic interactions slow down and in turn washload is no more lost to floodplain. Only during the early $Q_{falling}$, 3.6 Mt of washload

net gain occurred in a year, which was even less than 5% of the annual net loss to the floodplain.

To assess the spatial distribution of sediment sinks along the lower Amazon, we incorporated various hydro-geomorphic factors regarding floodplain geomorphic styles and morphometric parameters, such floodplain width, levee heights, water-saturated area, *SSSC* distribution over floodplain and distribution of impeded floodplain. Impeded floodplain that contains numerous large rounded lakes is the definition of active sediment sinks along the lower Amazon, which seasonally stores most of the water from the river. The results of these hydro-geomorphic factors collectively indicate that the extent and magnitudes of sediment sinks becomes larger downstream (from Manacapuru to Monte Alegre), which is proportionally related to the development of the water-saturated floodplain. This indicates the nonlinear geomorphic evolution of the Amazon floodplain through its longitudinal profile since the late Holocene that downstream reaches are still to be infilled with sediments (incomplete floodplain) thus acting as sediment sinks (Latrubesse 2015).

Chapter 6: Brief Summary and Final Remarks

In this dissertation, the roles of the large tributaries and vast floodplain along the Amazon River on suspended sediment distribution patterns are studied through specific studies focusing on representative reaches. Tributary impacts and interactions with floodplain are dealt in Chapters 2 and 5, and Chapters 3, 4 and 5, respectively at a different scale.

In Chapter 2, surface water types and sediment distribution patterns over different seasons and years (2007-standard, 2005-drought and 2009-flood) are assessed in the largest confluence in the world where two rivers with distinct hydrosedimentologic regimes drain: The Solimões and Negro Rivers. Post-confluence surface water types dominance was determined by discharge contribution of each river, which depends on the season. That is, during the Q_{rising} when the discharge gap between the Solimões and Negro is the largest of the year, Amazonian surface dominance was the greatest, and this patterns was observed regardless of the annual hydrological conditions. In contrast, surface water mixing along the river depended both on the hydrological seasons and years, with the highest mixed-homogenized area observed during water discharge peak season and the lowest during discharge rising season. The highest rates of water mixing were observed in 2009, followed by 2005 and 2007. Particular emphasis on floodplain ecology is made as surface water types along the river affects the ecological patterns, such as distribution of trees and fauna in the floodplain. In Chapter 5, dynamics

hydrosedimentologic inputs from the tributaries through differential timings on the Amazon main channel are examined through suspended sediment fluxes monitoring at *in-situ* gauge stations. Along the lower Amazon River, hydrosedimentary contributions from Madeira and Negro Rivers, and their influence on suspended sediment characteristics were significant. For example, washload flux at Obidos was the highest during March when Madeira's flux was also the highest. Likewise, Surface sediment concentration was the lowest in July and August at Obidos when Negro's discharge was the highest.

In Chapter 3, I assessed hydrological connectivity processes using a representative water-saturated and morphologically complex floodplain in the lower Amazon, the Lago Miratuba. Understanding on the channel-floodplain connectivity processes is very important as the Amazon River has enormous amount of water and sediment exchange continuously with floodplain, which is determined by the connectivity patterns. Complex inundation patterns over the different morpho-sedimentary units in floodplain are assessed by tracing the sediment-laden water throughout the annual hydrological cycle. Each geomorphic units in floodplain presented own threshold of connection with the main channel, and this did not correlate with the distance from the channel. Therefore in this chapter, I also addressed that the connectivity framework developed upon ecological application is not appropriate for large river floodplain, and rather specific reach-by-reach study is recommended.

In Chapter 4, the rating curve of the Amazon River at Obidos during flood stage is revisited. Obidos is the most downstream gauge station and considered the most

important station, as the discharge at Obidos has been widely used for several decades across disciplines. However as mentioned in Filizola et al. (2014), rating curve during flood stage overestimates the discharge mainly due to the seasonal floodplain water storage. In this chapter, by using the series of ADCP data collected over different seasons, the rating curve failure is systematically investigated. Here, I addressed that seasonal water storage of floodplain cause hysteresis in the rating curve during flood stages, especially after the channel-floodplain hydrological connection. Hysteresis during flood stage, i.e. higher discharge during $Q_{falling}$ than Q_{rising} on similar water level, is induced by the faster velocity during $Q_{falling}$ due to steeper water surface slope. Finally, a revised rating curve at Obidos was developed based on empirical relationships with field measurements, and also an upstream gauge station (Parintins) where rating curve does not fail was recommended as a new gauge station expected to better represent the basin.

In Chapter 5, using the *in situ* gauge stations along the Amazon River and major tributaries (Manacapuru, Manaus, Fazenda Vista Alegre, Obidos and Itaituba), I estimated washload discharge at each gauge stations over 15 years (2001-2015). Using the gauge station fluxes, the annual floodplain sedimentation along the lower Amazon River is estimated to be 79 Mt. I further investigated geomorphologic factors, such as floodplain width, area, bank heights, channel migration rates, inundation area and frequency, seasonal suspended sediment concentration distribution patterns over floodplain, influencing the spatial distribution of floodplain sediment sinks along the river. All these above mentioned geomorphic factors collectively indicated that the extent and magnitudes of sediment sinks become larger downstream, from Manacapuru to

Obidos (and Monte Alegre), which is proportionally related to the development of the water-saturated floodplain. This result supports the concept “incomplete floodplain” of the Amazon River that is, floodplain sediment infilling processes are transferred from up- to downstream along the river.

Through series of chapters, I could arrive to the conclusion that the hydrosedimentologic influences of the tributaries and channel-floodplain interactions on the Amazon River system’s suspended sediment distribution are significant and their patterns are complex than ever expected. The major factor contributing to this complexity are the geomorphology of the river, which is locally related to the long and intricate evolution history since the Holocene, but also to the current anabranching channel dynamics that formed the mosaic of geomorphic units. The geomorphologic styles along the Amazon River are, however also different reach-by-reach due to the varying interactive processes with regional tectonics, hydroclimatology and human activities. Hence, as in this dissertation, studying the Amazon River system has to be conducted reach-by-reach, by the nature of geomorphic complexity of the river. Series of the individual chapters in this dissertation, which focuses on the representative geomorphic styles of the each reach, play a role in enhancing the understanding of the hydrosedimentary processes and providing insights on the Amazon fluvial system processes. Lastly, the methodology developed in this dissertation research is expected to contribute to other researches studying the hydrosedimentologic processes of large river systems around the world.

Bibliography

Abril, G., Martinez, J.-M., Artigas, L.F., Moreira-Turcq, P., Benedetti, M.F., Vidal, L., Meziane, T., Kim, J.-H., Bernardes, M.C., & Savoye, N. (2014). Amazon River carbon dioxide outgassing fuelled by wetlands. *Nature, 505*, 395-398

Adams, J.B., Smith, M.O., & Johnson, P.E. (1986). Spectral Mixture Modeling - a New Analysis of Rock and Soil Types at the Viking Lander-1 Site. *Journal of Geophysical Research-Solid Earth and Planets, 91*, 8098-8112

Alcântara, E., Barbosa, C., Stech, J., Novo, E., & Shimabukuro, Y. (2009). Improving the spectral unmixing algorithm to map water turbidity distributions. *Environmental Modelling & Software, 24*, 1051-1061

Alsdorf, D., Bates, P., Melack, J., Wilson, M., & Dunne, T. (2007). Spatial and temporal complexity of the Amazon flood measured from space. *Geophysical Research Letters, 34*

Alsdorf, D., Dunne, T., Melack, J., Smith, L., & Hess, L. (2005). Diffusion modeling of recessional flow on central Amazonian floodplains. *Geophysical research letters, 32*

Alsdorf, D., Han, S.-C., Bates, P., & Melack, J. (2010). Seasonal water storage on the Amazon floodplain measured from satellites. *Remote Sensing of Environment, 114*, 2448-2456

Alsdorf, D.E. (2003). Water storage of the central Amazon floodplain measured with GIS and remote sensing imagery. *Annals of the Association of American Geographers, 93*, 55-66

Amoros, C., & Bornette, G. (2002). Connectivity and biocomplexity in waterbodies of riverine floodplains. *Freshwater Biology, 47*, 761-776

Arnesen, A.S., Silva, T.S., Hess, L.L., Novo, E.M., Rudorff, C.M., Chapman, B.D., & McDonald, K.C. (2013). Monitoring flood extent in the lower Amazon River floodplain using ALOS/PALSAR ScanSAR images. *Remote sensing of Environment, 130*, 51-61

Aucour, A.M., Tao, F.A., Moreira-Turcq, P., Seyler, P., Sheppard, S., & Benedetti, M.F. (2003). The Amazon River: behaviour of metals (Fe, Al, Mn) and dissolved organic matter in the initial mixing at the Rio Negro/Solimoes confluence. *Chemical Geology, 197*, 271-285

Baranya, S., Olsen, N., & Józsa, J. (2013). FLOW ANALYSIS OF A RIVER CONFLUENCE WITH FIELD MEASUREMENTS AND RANS MODEL WITH NESTED GRID APPROACH. *River Research and Applications*

Barbosa, C.C.F., de Moraes Novo, E.M.L., Melack, J.M., Gastil-Buhl, M., & Pereira Filho, W. (2010). Geospatial analysis of spatiotemporal patterns of pH, total suspended sediment and chlorophyll-a on the Amazon floodplain. *Limnology, 11*, 155-166

Bayley, P.B. (1995). Understanding Large River Floodplain Ecosystems. *BioScience, 45*, 153-158

Benda, L., Poff, N.L., Miller, D., Dunne, T., Reeves, G., Pess, G., & Pollock, M. (2004). The network dynamics hypothesis: How channel networks structure riverine habitats. *BioScience, 54*, 413-427

Best, J., & Rhoads, B.L. (2008). Sediment transport, bed morphology and the sedimentology of river channel confluences. In S.P. Rice, A.G. Roy, & B.L. Rhoads (Eds.), *River Confluences, Tributaries and the Fluvial Network* (pp. 45-72). West Sussex: John Wiley & Sons, Ltd

Best, J.L. (1988). Sediment Transport and Bed Morphology at River Channel Confluences. *Sedimentology, 35*, 481-498

Best, J.L., & Ashworth, P.J. (1997a). Scour in large braided rivers and the recognition of sequence stratigraphic boundaries. *Nature, 387*, 275-277

Best, J.L., & Ashworth, P.J. (1997b). Scour in large braided rivers, and the recognition of sequence stratigraphic boundaries. *Nature, 387*, 275-277

Best, J.L., & Roy, A.G. (1991). Mixing-Layer Distortion at the Confluence of Channels of Different Depth. *Nature, 350*, 411-413

Birkett, C., Mertes, L., Dunne, T., Costa, M., & Jasinski, M. (2002). Surface water dynamics in the Amazon Basin: Application of satellite radar altimetry. *Journal of Geophysical Research: Atmospheres, 107*

Biron, P.M., Richer, A., Kirkbride, A.D., Roy, A.G., & Han, S. (2002). Spatial patterns of water surface topography at a river confluence. *Earth Surface Processes and Landforms, 27*, 913-928

Blettler, M., Amsler, M.L., Ezcurra de Drago, I., Espinola, L.A., Eberle, E., Paira, A., Best, J.L., Parsons, D.R., & Drago, E.E. (2014). The impact of significant input of fine sediment on benthic fauna at tributary junctions: a case study of the Bermejo–Paraguay River confluence, Argentina. *Ecohydrology*

Bonnet, M.-P., Barroux, G., Martinez, J.-M., Seyler, F., Moreira-Turcq, P., Cochonneau, G., Melack, J., Boaventura, G., Maurice-Bourgoin, L., & León, J. (2008). Floodplain hydrology in an Amazon floodplain lake (Lago Grande de Curuaí). *Journal of Hydrology, 349*, 18-30

Bouchez, J., Lajeunesse, E., Gaillardet, J., France-Lanord, C., Dutra-Maia, P., & Maurice, L. (2010). Turbulent mixing in the Amazon River: The isotopic memory of confluences. *Earth and Planetary Science Letters, 290*, 37-43

Bouchez, J., Lupker, M., Gaillardet, J., France-Lanord, C., & Maurice, L. (2011). How important is it to integrate riverine suspended sediment chemical composition with depth? Clues from Amazon River depth-profiles. *Geochimica et Cosmochimica Acta, 75*, 6955-6970

Bourgoin, L.M., Bonnet, M.-P., Martinez, J.-M., Kosuth, P., Cochonneau, G., Moreira-Turcq, P., Guyot, J.-L., Vauchel, P., Filizola, N., & Seyler, P. (2007). Temporal dynamics of water and sediment exchanges between the Curuaí floodplain and the Amazon River, Brazil. *Journal of Hydrology, 335*, 140-156

Bradbrook, K.F., Lane, S.N., Richards, K.S., Biron, P.M., & Roy, A.G. (2001). Role of bed discordance at asymmetrical river confluences. *Journal of Hydraulic Engineering-Asce, 127*, 351-368

Callède, J., Guyot, J., Molinier, M., Guimaraes, V., Oliveira, E., & Filizola, N. (1997). La variabilité des débits de l'Amazone à Obidos (Amazonas, Brésil). *Sustainability of Water Resources under Increasing Uncertainty*, 163-172

Carder, K.L., Chen, F.R., Lee, Z., Hawes, S.K., & Cannizzaro, J.P. (2003). MODIS ocean science team algorithm theoretical basis document. *ATBD, 19*, 7-18

Chavula, G., Brezonik, P., Thenkabail, P., Johnson, T., & Bauer, M. (2009). Estimating chlorophyll concentration in Lake Malawi from MODIS satellite imagery. *Physics and Chemistry of the Earth, Parts A/B/C, 34*, 755-760

Cochonneau, G., Sondag, F., Guyot, J.L., Geraldo, B., Filizola, N., Fraizy, P., Laraque, A., Magat, P., Martinez, J.M., Noriega, L., Oliveira, E., Ordonez, J., Pombosa, R., Seyler, F., Sidgwick, J., & Vauchel, P. (2006). The environmental observation and research project, ORE HYBAM, and the rivers of the Amazon basin. *Climate Variability and Change - Hydrological Impacts, 308*, 44-50

Cohn-Haft, M., Whittaker, A., & Stouffer, P.C. (1997). A new look at the" species-poor" central Amazon: the avifauna north of Manaus, Brazil. *Ornithological monographs*, 205-235

Colby, B.R. (1963). *Fluvial sediments: a summary of source, transportation, deposition, and measurement of sediment discharge*. US Government Printing Office

Constantine, J.A., Dunne, T., Ahmed, J., Legleiter, C., & Lazarus, E.D. (2014). Sediment supply as a driver of river meandering and floodplain evolution in the Amazon Basin. *Nature Geoscience, 7*, 899-903

Constantinescu, G., Miyawaki, S., Rhoads, B., & Sukhodolov, A. (2012). Numerical analysis of the effect of momentum ratio on the dynamics and sediment-entrainment capacity of coherent flow structures at a stream confluence. *Journal of Geophysical Research-Earth Surface, 117*

de Andrade, G.O. (1956). *Furos, paranás e igarapés: análise genética de alguns elementos do sistema potamográfico amazònico; comunicação oferecida ao XVIII Congresso Internacional de Geografia, Rio, agosto de 1956*.

de Moraes Novo, E.M.L., de Farias Barbosa, C.C., de Freitas, R.M., Shimabukuro, Y.E., Melack, J.M., & Pereira Filho, W. (2006). Seasonal changes in chlorophyll distributions in Amazon floodplain lakes derived from MODIS images. *Limnology, 7*, 153-161

de Paiva, R.C.D., Buarque, D.C., Collischonn, W., Bonnet, M.P., Frappart, F., Calmant, S., & Bulhões Mendes, C.A. (2013). Large-scale hydrologic and hydrodynamic modeling of the Amazon River basin. *Water Resources Research, 49*, 1226-1243

Dogliotti, A., Ruddick, K., Nechad, B., Doxaran, D., & Knaeps, E. (2015). A single algorithm to retrieve turbidity from remotely-sensed data in all coastal and estuarine waters. *Remote Sensing of Environment, 156*, 157-168

Doxaran, D., Froidefond, J.M., Lavender, S., & Castaing, P. (2002). Spectral signature of highly turbid waters - Application with SPOT data to quantify suspended particulate matter concentrations. *Remote Sensing of Environment, 81*, 149-161

Drago, E., de Drago, I.E., Oliveros, O., & Paira, A. (2003). Aquatic habitats, fish and invertebrate assemblages of the Middle Paraná River. *Amazoniana, 17*, 291-341

Drago, E.C., Paira, A.R., & Wantzen, K.M. (2008). Channel-floodplain geomorphology and connectivity of the Lower Paraguay hydrosystem. *Ecohydrology & Hydrobiology, 8*, 31-48

Dring, M.J. (1984). Light and Photosynthesis in Aquatic Ecosystems - Kirk,Jto. *Nature, 309*, 382-382

Dunne, T., & Aalto, R. (2013a). Large river floodplains. In J.F. Shroder (Ed.), *Treatise on geomorphology* (pp. 645-678). Netherland: Elsevier

Dunne, T., & Aalto, R. (2013b). Large river floodplains. *Treatise on geomorphology, 9*, 645-678

Dunne, T., Mertes, L.A., Meade, R.H., Richey, J.E., & Forsberg, B.R. (1998a). Exchanges of sediment between the flood plain and channel of the Amazon River in Brazil. *Geological Society of America Bulletin, 110*, 450-467

Dunne, T., Mertes, L.A.K., Meade, R.H., Richey, J.E., & Forsberg, B.R. (1998b). Exchanges of sediment between the flood plain and channel of the Amazon River in Brazil. *Geological Society of America Bulletin, 110*, 0450

Escauriaza, C., Gonzalez, C., Guerra, P., Pasten, P., & Pizarro, G. (2012). Formation and fate of contaminant particles controlled by turbulent coherent structures and geochemistry in a reactive river confluence. *Bulletin of the American Physical Society, 57*

Evans, T.L., Costa, M., Telmer, K., & Silva, T.S. (2010). Using ALOS/PALSAR and RADARSAT-2 to map land cover and seasonal inundation in the Brazilian Pantanal. *Selected Topics in Applied Earth Observations and Remote Sensing, IEEE Journal of, 3*, 560-575

FGDC, N. (2008). Federal Geographic Data Committee National Vegetation Classification. In: FGDC-STD-005-2008 (Version 2). Federal Geographic Data Committee, US Geological Survey, Reston, Virginia, USA. http://www. fgdc. gov/standards/projects/FGDC-standardsprojects/vegetation/standards/projects/vegetation

Filizola Jr, N.P. (1999). *O fluxo de sedimentos em suspensão nos rios da bacia Amazônica Brasileira*. ANEEL

Filizola, N., de Oliveira, E., Wittmann, H., Guyot, J.-L., & Martinez, J.-M. (2011a). *The significance of suspended sediment transport determination on the Amazonian hydrological scenario*. INTECH Open Access Publisher

Filizola, N., & Guyot, J.L. (2004). The use of Doppler technology for suspended sediment discharge determination in the River Amazon. *Hydrological Sciences Journal-Journal Des Sciences Hydrologiques, 49*, 143-153

Filizola, N., & Guyot, J.L. (2009). Suspended sediment yields in the Amazon basin: an assessment using the Brazilian national data set. *Hydrological Processes, 23*, 3207-3215

Filizola, N., Guyot, J.L., Wittmann, H., Martinez, J.M., & Oliveira, E. (2011b). The Significance of Suspended Sediment Transport Determination on the Amazonian Hydrological Scenario. In A. Manning (Ed.), *Sediment Transport in Aquatic Environments*: InTech

Filizola, N., Latrubesse, E.M., Fraizy, P., Souza, R., Guimarães, V., & Guyot, J.-L. (2013). Was the 2009 flood the most hazardous or the largest ever recorded in the Amazon? *Geomorphology*

Filizola, N., Latrubesse, E.M., Fraizy, P., Souza, R., Guimarães, V., & Guyot, J.-L. (2014). Was the 2009 flood the most hazardous or the largest ever recorded in the Amazon? *Geomorphology, 215*, 99-105

Filizola, N., Spínola, N., Arruda, W., Seyler, F., Calmant, S., & Silva, J. (2009). The Rio Negro and Rio Solimões confluence point—Hydrometric observations during the 2006/2007 cycle. *River, Coastal and Estuarine Morphodynamics—RCEM, 2009*, 1003-1006

Fleischmann, A.S., Paiva, R.C., Collischonn, W., Sorribas, M.V., & Pontes, P.R. (2016). On river-floodplain interaction and hydrograph skewness. *Water Resources Research, 52*

Franzinelli, E., & Igreja, H. (2011). Ponta das Lajes eo Encontro das Águas, AM

Frias, C., Abad, J., Mendoza, A., Paredes, J., Ortals, C., & Montoro, H. (2015). Planform evolution of two anabranching structures in the Upper Peruvian Amazon River. *Water Resources Research, 51*, 2742-2759

Fricke, A.T., Nittrouer, C.A., Ogston, A.S., Nowacki, D.J., Asp, N.E., Souza Filho, P.W., da Silva, M.S., & Jalowska, A.M. (2017). River tributaries as sediment sinks: Processes operating where the Tapajós and Xingu rivers meet the Amazon tidal river. *Sedimentology*

Goulding, M., Barthem, R., Ferreira, E.J.G., & Duenas, R. (2003). *The Smithsonian atlas of the Amazon*. Smithsonian Books Washington, DC

Graf, W.L. (1999). Dam nation: A geographic census of American dams and their large-scale hydrologic impacts. *Water Resources Research, 35*, 1305-1311

Guyot, J.L., Bazan, H., Fraizy, P., Ordonez, J.J., Armijos, E., & Laraque, A. (2007). Suspended sediment yields in the Amazon basin of Peru: a first estimation. *IAHS publication, 314*, 3

Hackney, C., & Carling, P. (2011). The occurrence of obtuse junction angles and changes in channel width below tributaries along the Mekong River, south-east Asia. *Earth Surface Processes and Landforms, 36*, 1563-1576

Han, S.C., Kim, H., Yeo, I.Y., Yeh, P., Oki, T., Seo, K.W., Alsdorf, D., & Luthcke, S.B. (2009). Dynamics of surface water storage in the Amazon inferred from measurements of inter-satellite distance change. *Geophysical Research Letters, 36*

Heiler, G., Hein, T., Schiemer, F., & Bornette, G. (1995). Hydrological connectivity and flood pulses as the central aspects for the integrity of a river-floodplain system. *Regulated Rivers: Research & Management, 11*, 351-361

Hess, L.L., Melack, J.M., Affonso, A.G., Barbosa, C.C.F., Gastil-Buhl, M., & Novo., E.M.L.M. (2015). LBA-ECO LC-07 Wetland Extent, Vegetation, and Inundation: Lowland Amazon Basin. In. Oak Ridge, Tennessee, USA: ORNL DAAC

Hess, L.L., Melack, J.M., Novo, E.M., Barbosa, C.C., & Gastil, M. (2003). Dual-season mapping of wetland inundation and vegetation for the central Amazon basin. *Remote Sensing of Environment, 87*, 404-428

Hudson, P., Sounny-Slitine, M., & LaFevor, M. (2013). A new longitudinal approach to assess hydrologic connectivity: Embanked floodplain inundation along the lower Mississippi River. *Hydrological Processes, 27*, 2187-2196

Hudson, P.F., & Colditz, R.R. (2003). Flood delineation in a large and complex alluvial valley, lower Panuco basin, Mexico. *Journal of Hydrology, 280*, 229-245

Hudson, P.F., Heitmuller, F.T., & Leitch, M.B. (2012). Hydrologic connectivity of oxbow lakes along the lower Guadalupe River, Texas: the influence of geomorphic and climatic controls on the "flood pulse concept". *Journal of Hydrology, 414*, 174-183

Huete, A., Didan, K., Miura, T., Rodriguez, E.P., Gao, X., & Ferreira, L.G. (2002a). Overview of the radiometric and biophysical performance of the MODIS vegetation indices. *Remote Sensing of Environment, 83*, 195-213

Huete, A., Didan, K., Miura, T., Rodriguez, E.P., Gao, X., & Ferreira, L.G. (2002b). Overview of the radiometric and biophysical performance of the MODIS vegetation indices. *Remote Sensing of Environment, 83*, 195-213

Iriondo, M. (1982). Geomorfologia da planície Amazônica. *SBG, Simp. Quatern. Brasil, 4*, 323-348

Isaaks, E., & Srivastava, R. (2011). Applied Geostatistics. *London: Oxford University*

Jung, H.C., & Alsdorf, D. (2010). Repeat-pass multi-temporal interferometric SAR coherence variations with Amazon floodplain and lake habitats. *International Journal of Remote Sensing, 31*, 881-901

Junk, W.J. (1997). *The central Amazon floodplain: ecology of a pulsing system*. Springer

Junk, W.J., Bayley, P.B., & Sparks, R.E. (1989). The flood pulse concept in river-floodplain systems. *Canadian special publication of fisheries and aquatic sciences, 106*, 110-127

Kilham, N.E., & Roberts, D. (2011). Amazon River time series of surface sediment concentration from MODIS. *International journal of remote sensing, 32*, 2659-2679

Kirk, J. (1989). The upwelling light stream in natural waters. *Limnology and Oceanography, 34*, 1410-1425

Kirk, J.T. (1994). *Light and photosynthesis in aquatic ecosystems*. Cambridge university press

Koponen, P., Nygren, P., Sabatier, D., Rousteau, A., & Saur, E. (2004). Tree species diversity and forest structure in relation to microtopography in a tropical freshwater swamp forest in French Guiana. *Plant Ecology, 173*, 17-32

Kosuth, P., Callede, J., Laraque, A., Filizola, N., Guyot, J.L., Seyler, P., Fritsch, J.M., & Guimaraes, V. (2009). Sea-tide effects on flows in the lower reaches of the Amazon River. *Hydrological Processes, 23*, 3141-3150

Lane, S., Parsons, D., Best, J., Orfeo, O., Kostaschuk, R., & Hardy, R. (2008a). Causes of rapid mixing at a junction of two large rivers: Río Paraná and Río Paraguay, Argentina. *Journal of Geophysical Research: Earth Surface (2003–2012), 113*

Lane, S.N., Parsons, D.R., Best, J.L., Orfeo, O., Kostaschuk, R.A., & Hardy, R.J. (2008b). Causes of rapid mixing at a junction of two large rivers: Rio Parana and Rio Paraguay, Argentina. *Journal of Geophysical Research-Earth Surface, 113*

Laraque, A., Guyot, J.L., & Filizola, N. (2009). Mixing processes in the Amazon River at the confluences of the Negro and Solimoes Rivers, Encontro das Aguas, Manaus, Brazil. *Hydrological Processes, 23*, 3131-3140

Latrubesse, E. (2010). The paradox of large alluvial rivers. *AGU Fall Meeting Abstracts, 1*, 05

Latrubesse, E.M. (2008). Patterns of anabranching channels: The ultimate end-member adjustment of mega rivers. *Geomorphology, 101*, 130-145

Latrubesse, E.M. (2012). Amazon Lakes. In L. Bengtsson, R. Herschy, & R. Fairbridge (Eds.), *Lakes and Reservoirs* (pp. 13-26): Springer Verlag

Latrubesse, E.M. (2015). Large rivers, megafans and other Quaternary avulsive fluvial systems: A potential "who's who" in the geological record. *Earth-Science Reviews, 146*, 1-30

Latrubesse, E.M., Arima, E.Y., Dunne, T., Park, E., Baker, V., d'Horta, F., & others, a. (2017). Damming the rivers of the Amazon Basin. *Nature, 546*, 363-369

Latrubesse, E.M., & Franzinelli, E. (2002). The Holocene alluvial plain of the middle Amazon River, Brazil. *Geomorphology, 44*, 241-257

Latrubesse, E.M., & Franzinelli, E. (2005). The late Quaternary evolution of the Negro River, Amazon, Brazil: Implications for island and floodplain formation in large anabranching tropical systems. *Geomorphology, 70*, 372-397

Latrubesse, E.M., & Park, E. (2017). Rivers and Streams. In R.A. Marston (Ed.), *The International Encyclopedia of Geography*: John Wiley & Sons, Ltd.

Latrubesse, E.M., & Restrepo, J.D. (2014). Sediment yield along the Andes: continental budget, regional variations, and comparisons with other basins from orogenic mountain belts. *Geomorphology, 216*, 225-233

Latrubesse, E.M., Stevaux, J.C., & Sinha, R. (2005). Tropical rivers. *Geomorphology, 70*, 187-206

Latrubesse, E.M., Stevaux, J.C., & Young, K.R. (2013). Hydro-geomorphologic processes and Quaternary landforms controlling biotic components in South American wetlands: Introduction. *Journal of South American Earth Sciences, 46*, 110-112

Lee, H., Jung, H.C., Yuan, T., Beighley, R.E., & Duan, J. (2014). Controls of Terrestrial Water Storage Changes Over the Central Congo Basin Determined by Integrating PALSAR ScanSAR, Envisat Altimetry, and GRACE Data. *Remote Sensing of the Terrestrial Water Cycle* (pp. 115-129): John Wiley & Sons, Inc

Lewin, J., Ashworth, P.J., & Strick, R.J. (2017). Spillage sedimentation on large river floodplains. *Earth Surface Processes and Landforms*

Lima, I.B.T., Rosa, R.R., Ramos, F.M., & de Moraes Novo, E.M.L. (2003). Water level dynamics in the Amazon floodplain. *Advances in Water Resources, 26*, 725-732

Lininger, K.B., & Latrubesse, E.M. (2016). Flooding hydrology and peak discharge attenuation along the middle Araguaia River in central Brazil. *CATENA, 143*, 90-101

Mangiarotti, S., Martinez, J.M., Bonnet, M.P., Buarque, D.C., Filizola, N., & Mazzega, P. (2013). Discharge and suspended sediment flux estimated along the mainstream of the Amazon and the Madeira Rivers (from in situ and MODIS Satellite Data). *International Journal of Applied Earth Observation and Geoinformation, 21*, 341-355

Marchetti, Z., Latrubesse, E., Pereira, M., & Ramonell, C. (2013). Vegetation and its relationship with geomorphologic units in the Parana River floodplain, Argentina. *Journal of South American Earth Sciences, 46*, 122-136

Martinez, J.-M., Bourgoin, L.M., Kosuth, P., Seyler, F., & Guyot, J. (2003). Analysis of multitemporal MODIS and Landsat 7 images acquired over Amazonian floodplains lakes for suspended sediment concentrations retrieval. In, *Geoscience and Remote Sensing Symposium, 2003. IGARSS'03. Proceedings. 2003 IEEE International* (pp. 2122-2124): IEEE

Martinez, J.-M., & Le Toan, T. (2007). Mapping of flood dynamics and spatial distribution of vegetation in the Amazon floodplain using multitemporal SAR data. *Remote Sensing of Environment, 108*, 209-223

Martinez, J.M., Guyot, J.L., Filizola, N., & Sondag, F. (2009). Increase in suspended sediment discharge of the Amazon River assessed by monitoring network and satellite data. *CATENA, 79*, 257-264

Maurice-Bourgoin, L., Quemerais, B., Moreira-Turcq, P., & Seyler, P. (2003). Transport, distribution and speciation of mercury in the Amazon River at the confluence of black and white waters of the Negro and Solimoes Rivers. *Hydrological Processes, 17*, 1405-1417

McFeeters, S. (1996). The use of the Normalized Difference Water Index (NDWI) in the delineation of open water features. *International journal of remote sensing, 17*, 1425-1432

Meade, R.H. (1985). Suspended sediment in the Amazon River and its tributaries in Brazil during 1982-84. In: US Geological Survey

Meade, R.H. (1988). Movement and storage of sediment in river systems. *Physical and chemical weathering in geochemical cycles* (pp. 165-179): Springer

Meade, R.H. (1994). Suspended sediments of the modern Amazon and Orinoco rivers. *Quaternary International, 21*, 29-39

Meade, R.H. (1996). River-sediment inputs to major deltas. *Sea-level rise and coastal subsidence* (pp. 63-85): Springer

Meade, R.H. (2007). *Transcontinental moving and storage: the Orinoco and Amazon Rivers transfer the Andes to the Atlantic*. John Wiley & Sons: Chichester

Meade, R.H., Dunne, T., Richey, J.E., Santos, U.d.M., & Salati, E. (1985). Storage and remobilization of suspended sediment in the lower Amazon River of Brazil. *Science, 228*, 488-490

Meade, R.H., Nordin, C.F., Curtis, W.F., Costarodrigues, F.M., Dovale, C.M., & Edmond, J.M. (1979). Sediment Loads in the Amazon River. *Nature, 278*, 161-163

Meade, R.H., Rayol, J.M., Daconceicao, S.C., & Natividade, J.R.G. (1991). Backwater Effects in the Amazon River Basin of Brazil. *Environmental Geology and Water Sciences, 18*, 105-114

Mertes, L.A. (1994). Rates of flood-plain sedimentation on the central Amazon River. *Geology, 22*, 171-174

Mertes, L.A. (1997). Documentation and significance of the perirheic zone on inundated floodplains. *Water Resources Research, 33*, 1749-1762

Mertes, L.A. (2000). *Inundation hydrology*. Cambridge University Press: Cambridge

Mertes, L.A., Daniel, D.L., Melack, J.M., Nelson, B., Martinelli, L.A., & Forsberg, B.R. (1995a). Spatial patterns of hydrology, geomorphology, and vegetation on the floodplain of the Amazon River in Brazil from a remote sensing perspective. *Geomorphology, 13*, 215-232

Mertes, L.A., Dunne, T., & Martinelli, L.A. (1996a). Channel-floodplain geomorphology along the Solimões-Amazon river, Brazil. *Geological Society of America Bulletin, 108*, 1089-1107

Mertes, L.A., & Magadzire, T.T. (2007). Large rivers from space. *Large Rivers: Geomorphology and Management*, 535-552

Mertes, L.A., Smith, M.O., & Adams, J.B. (1993a). Estimating suspended sediment concentrations in surface waters of the Amazon River wetlands from Landsat images. *Remote Sensing of Environment, 43*, 281-301

Mertes, L.A.K., Daniel, D.L., Melack, J.M., Nelson, B., Martinelli, L.A., & Forsberg, B.R. (1995b). Spatial Patterns of Hydrology, Geomorphology, and Vegetation on the Floodplain of the Amazon River in Brazil from a Remote-Sensing Perspective. *Geomorphology, 13*, 215-232

Mertes, L.A.K., Dunne, T., & Martinelli, L.A. (1996b). Channel-floodplain geomorphology along the Solimoes-Amazon River, Brazil. *Geological Society of America Bulletin, 108*, 1089-1107

Mertes, L.A.K., & Magadzire, T.T. (2008a). Large Rivers from Space. In A. Gupta (Ed.), *Large Rivers: Geomorphology and Management* (pp. 535-552): John Wiley & Sons, Ltd

Mertes, L.A.K., & Magadzire, T.T. (2008b). Large Rivers from Space. *Large Rivers* (pp. 535-552): John Wiley & Sons, Ltd

Mertes, L.A.K., Smith, M.O., & Adams, J.B. (1993b). Estimating Suspended Sediment Concentrations in Surface Waters of the Amazon River Wetlands from Landsat Images. *Remote Sensing of Environment, 43*, 281-301

Merwade, V.M., Maidment, D.R., & Goff, J.A. (2006). Anisotropic considerations while interpolating river channel bathymetry. *Journal of Hydrology, 331*, 731-741

Milliman, J.D., & Meade, R.H. (1983). World-Wide Delivery of River Sediment to the Oceans. *Journal of Geology, 91*, 1-21

Molinier, M., Guyot, J.-L., De Oliveira, E., Guimarães, V., & Chaves, A. (1995). Hydrologie du bassin de l'Amazone. *Proc. Grands Bassins Fluviaux Péri-atlantiques, 1*, 335-344

Montanher, O.C., Novo, E.M., Barbosa, C.C., Rennó, C.D., & Silva, T.S. (2014). Empirical models for estimating the suspended sediment concentration in Amazonian white water rivers using Landsat 5/TM. *International Journal of Applied Earth Observation and Geoinformation, 29*, 67-77

Moreira-Turcq, P., Jouanneau, J., Turcq, B., Seyler, P., Weber, O., & Guyot, J.-L. (2004). Carbon sedimentation at Lago Grande de Curuai, a floodplain lake in the low Amazon region: insights into sedimentation rates. *Palaeogeography, Palaeoclimatology, Palaeoecology, 214*, 27-40

Mortillaro, J., Abril, G., Moreira-Turcq, P., Sobrinho, R., Perez, M., & Meziane, T. (2011). Fatty acid and stable isotope (δ 13 C, δ 15 N) signatures of particulate organic matter in the lower Amazon River: seasonal contrasts and connectivity between floodplain lakes and the mainstem. *Organic Geochemistry, 42*, 1159-1168

Neiff, J. (1996). Large rivers of South America: toward the new approach. In, *Verh. Int. Ver. Theor. Angew. Limnol./Proc. Int. Assoc. Theor. Appl. Limnol./Trav. Assoc. Int. Limnol. Theor. Appl.* (pp. 167-180)

Neiff, J., Poi de Neiff, A., Thomaz, S., & Bini, L. (2003). Connectivity processes as a basis for the management of aquatic plants. *Ecologia e manejo de macrófitas aquáticas*, 39-58

Nittrouer, C.A., Kuehl, S.A., Sternberg, R.W., Figueiredo, A.G., & Faria, L.E. (1995). An introduction to the geological significance of sediment transport and accumulation on the Amazon continental shelf. *Marine Geology, 125*, 177-192

Novo, E.M.L., de Farias Barbosa, C.C., de Freitas, R.M., Shimabukuro, Y.E., Melack, J.M., & Pereira Filho, W. (2006). Seasonal changes in chlorophyll distributions in Amazon floodplain lakes derived from MODIS images. *Limnology, 7*, 153-161

O'Loughlin, F., Paiva, R., Durand, M., Alsdorf, D., & Bates, P. (2016). A multi-sensor approach towards a global vegetation corrected SRTM DEM product. *Remote Sensing of Environment, 182*, 49-59

Ozesmi, S.L., & Bauer, M.E. (2002). Satellite remote sensing of wetlands. *Wetlands Ecology and Management, 10*, 381-402

Paiva, R.C.D., Buarque, D.C., Collischonn, W., Bonnet, M.P., Frappart, F., Calmant, S., & Bulhões Mendes, C.A. (2013). Large-scale hydrologic and hydrodynamic modeling of the Amazon River basin. *Water Resources Research, 49*, 1226-1243

Park, E. (2013). Temporal and spatial analysis of suspended sediment distribution in the Amazon River using satellite imagery. In, *Geography and Environment*. Austin: University of Texas

Park, E., & Latrubesse, E.M. (2014). Modeling suspended sediment distribution patterns of the Amazon River using MODIS data. *Remote sensing of Environment, 147*, 232-242

Park, E., & Latrubesse, E.M. (2015). Surface water types and sediment distribution patterns at the confluence of mega rivers: The Solimões-Amazon and Negro Rivers junction. *Water Resources Research, 51,* 6197-6213

Park, E., & Latrubesse, E.M. (2017). The hydro-geomorphologic complexity of the lower Amazon River floodplain and hydrological connectivity assessed by remote sensing and field control. *Remote Sensing of Environment, 198,* 321-332

Park, E., & Latrubesse, E.M. (in prep.). Spatiotemporal distribution of floodplain sediment sinks in the lower Amazon River: a geomorphological assessment using *in situ* gauge stations. *To be submitted to Geological Society of America Bulletin*

Park, E., & Latrubesse, E.M. (Submitted). Amazon River rating curve at Obidos revisited incorporating channel-floodplain interrelated processes. *Water Resources Research*

Parsons, D., Jackson, P., Czuba, J., Engel, F., Rhoads, B., Oberg, K., Best, J., Mueller, D., Johnson, K., & Riley, J. (2013). Velocity Mapping Toolbox (VMT): a processing and visualization suite for moving-vessel ADCP measurements. *Earth Surface Processes and Landforms, 38,* 1244-1260

Parsons, D.R., Best, J.L., Lane, S.N., Orfeo, O., Hardy, R.J., & Kostaschuk, R. (2007). Form roughness and the absence of secondary flow in a large confluence-diffluence, Rio Parana, Argentina. *Earth Surface Processes and Landforms, 32*, 155-162

Pavelsky, T.M., & Smith, L.C. (2009). Remote sensing of suspended sediment concentration, flow velocity, and lake recharge in the Peace-Athabasca Delta, Canada. *Water Resources Research, 45*

Petry, P., Bayley, P., & Markle, D. (2003). Relationships between fish assemblages, macrophytes and environmental gradients in the Amazon River floodplain. *Journal of Fish Biology, 63,* 547-579

Petts, G.E. (1984). *Impounded rivers: perspectives for ecological management*. john Wiley

Phillips, J.D. (2013). Hydrological connectivity of abandoned channel water bodies on a coastal plain river. *River Research and Applications, 29*, 149-160

Pringle, C. (2003). What is hydrologic connectivity and why is it ecologically important? *Hydrological Processes, 17,* 2685-2689

Remsen Jr, J., & Parker III, T.A. (1983). Contribution of river-created habitats to bird species richness in Amazonia. *Biotropica*, 223-231

Restrepo, J.D., Park, E., Aquino, S., & Latrubesse, E.M. (2016). Coral reefs chronically exposed to river sediment plumes in the southwestern Caribbean: Rosario Islands, Colombia. *Science of the Total Environment, 553,* 316-329

Rice, S., & Church, M. (1998). Grain size along two gravel-bed rivers: Statistical variation, spatial pattern and sedimentary links. *Earth Surface Processes and Landforms, 23*, 345-363

Rice, S.P., Roy, A.G., Rhoads, B.L., & Anne and Joseph Trachtman Memorial Book Fund. (2008). *River confluences, tributaries, and the fluvial network*. Hoboken, N.J.: Wiley

Richey, J.E., Mertes, L.A., Dunne, T., Victoria, R.L., Forsberg, B.R., Tancredi, A.C., & Oliveira, E. (1989). Sources and routing of the Amazon River flood wave. *Global Biogeochemical Cycles, 3*, 191-204

Ronchail, J., Guyot, J., Villar, J.C.E., Fraizy, P., Cochonneau, G., De Oliveira, E., Filizola, N., & Ordenez, J.J. (2006). Impact of the Amazon tributaries on major floods at Óbidos. *IAHS publication, 308*, 220

Rosenqvist, A., Shimada, M., Ito, N., & Watanabe, M. (2007). ALOS PALSAR: A pathfinder mission for global-scale monitoring of the environment. *Geoscience and Remote Sensing, IEEE Transactions on, 45*, 3307-3316

Rozo, M.G., Nogueira, A.C.R., & Truckenbrodt, W. (2012). The anastomosing pattern and the extensively distributed scroll bars in the middle Amazon River. *Earth Surface Processes and Landforms, 37*, 1471-1488

Rudorff, C.M., Melack, J.M., & Bates, P.D. (2014a). Flooding dynamics on the lower Amazon floodplain: 1. Hydraulic controls on water elevation, inundation extent, and river-floodplain discharge. *Water Resources Research, 50*, 619-634

Rudorff, C.M., Melack, J.M., & Bates, P.D. (2014b). Flooding dynamics on the lower Amazon floodplain: 2. Seasonal and interannual hydrological variability. *Water Resources Research, 50*, 635-649

Sayers, M.J., Grimm, A.G., Shuchman, R.A., Deines, A.M., Bunnell, D.B., Raymer, Z.B., Rogers, M.W., Woelmer, W., Bennion, D.H., & Brooks, C.N. (2015). A new method to generate a high-resolution global distribution map of lake chlorophyll. *International journal of remote sensing, 36*, 1942-1964

Shimada, M., Isoguchi, O., Tadono, T., & Isono, K. (2009). PALSAR radiometric and geometric calibration. *Geoscience and Remote Sensing, IEEE Transactions on, 47*, 3915-3932

Sioli, H. (1984). The Amazon and its main affluents: hydrography, morphology of the river courses, and river types. *The Amazon* (pp. 127-165): Springer

Sippel, S.J., Hamilton, S.K., Melack, J.M., & Choudhury, B.J. (1994). Determination of inundation area in the Amazon River floodplain using the SMMR 37 GHz polarization difference. *Remote Sensing of Environment, 48*, 70-76

Sobrinho, R., Bernardes, M., Abril, G., Kim, J., Zell, C., Mortillaro, J., Meziane, T., Moreira-Turcq, P., & Damsté, J.S. (2015). Spatial and seasonal contrasts of sedimentary organic matter in floodplain lakes of the central Amazon basin. *Biogeosciences Discussions, 12*, 8747-8787

Stevaux, J.C., Amâncio, A., de Carlos Etchebehere, M.L., & Fujita, R.H. (2009a). Flow structure and dynamics in large tropical rivers confluence: Example of the Ivai and Parana rivers, Southern Brazil. *Geociências (São Paulo), 28*, 5-13

Stevaux, J.C., Corradini, F.A., & Aquino, S. (2013). Connectivity processes and riparian vegetation of the upper Paraná River, Brazil. *Journal of South American Earth Sciences, 46*, 113-121

Stevaux, J.C., Franco, A.A., Etchebehere, M.L.d.C., & Fujita, R.H. (2009b). Flow structure and dynamics in large tropical river confluence: Example of the Ivaí and Paraná rivers, Southern Brazil. *Geociências (São Paulo), 28*, 5-13

Stevaux, J.C., Paes, R.J., Franco, A.A., Etchebehere, M.L., & Fujita, R.H. (2011). Morphodynamics in the Confluence of large regulated Rivers: the case of Paraná and Paranapanema Rivers. *Latin American journal of sedimentology and basin analysis, 16*

Strasser, M., Vinzon, S., & Kosuth, P. (2002). Bottom structures geometry of the Amazon River. In, *International Conference on Fluvial Hydraulics, Louvain-la-Neuve* (pp. 1185-1193)

Strasser, M.A. (2008). Dunas fluviais no Rio Solimoes-Amazonas-Dinamica e transporte de sedimentos. In: Universidade Federal do Rio de Janeiro

Strasser, M.A., Ribeiro Neto, A., SILVA, R., & MASCARENHAS, F. (2005). Estudo da variação do coeficiente de rugosidade de Manning em rios da Bacia Amazônica por meio de modelagem hidrodinâmica. *XVI Simpósio Brasileiro de Recursos Hídricos*

Syvitski, J.P., Vörösmarty, C.J., Kettner, A.J., & Green, P. (2005). Impact of humans on the flux of terrestrial sediment to the global coastal ocean. *Science, 308*, 376-380

Szupiany, R.N., Amsler, M.L., Parsons, D.R., & Best, J.L. (2009a). Morphology, flow structure, and suspended bed sediment transport at two large braid-bar confluences. *Water Resources Research, 45*

Szupiany, R.N., Amsler, M.L., Parsons, D.R., & Best, J.L. (2009b). Morphology, flow structure, and suspended bed sediment transport at two large braid-bar confluences. *Water Resources Research, 45*

Tockner, K., Malard, F., & Ward, J. (2000). An extension of the flood pulse concept. *Hydrological Processes, 14*, 2861-2883

Tomasella, J., Pinho, P.F., Borma, L.S., Marengo, J.A., Nobre, C.A., Bittencourt, O.R., Prado, M.C., Rodriguez, D.A., & Cuartas, L.A. (2013). The droughts of 1997 and 2005 in Amazonia: floodplain hydrology and its potential ecological and human impacts. *Climatic change*, *116*, 723-746

Tricart, J.L. (1977). Types de lits fluviaux en Amazonie brésilienne. In, *Annales de géographie* (pp. 1-54): JSTOR

Vermote, E., & Vermeulen, A. (1999). Atmospheric correction algorithm: spectral reflectances (MOD09). *ATBD version, 4*

Villar, R.E., Martinez, J.M., Guyot, J.L., Fraizy, P., Armijos, E., Crave, A., Bazan, H., Vauchel, P., & Lavado, W. (2012). The integration of field measurements and satellite observations to determine river solid loads in poorly monitored basins. *Journal of Hydrology, 444*, 221-228

Villar, R.E., Martinez, J.M., Le Texier, M., Guyot, J.L., Fraizy, P., Meneses, P.R., & de Oliveira, E. (2013). A study of sediment transport in the Madeira River, Brazil, using MODIS remote-sensing images. *Journal of South American Earth Sciences, 44*, 45-54

Wilson, M., Bates, P., Alsdorf, D., Forsberg, B., Horritt, M., Melack, J., Frappart, F., & Famiglietti, J. (2007). Modeling large-scale inundation of Amazonian seasonally flooded wetlands. *Geophysical research letters, 34*

Wittmann, H., von Blanckenburg, F., Guyot, J.L., Laraque, A., Bernal, C., & Kubik, P.W. (2011). Sediment production and transport from in situ-produced cosmogenic Be-10 and river loads in the Napo River basin, an upper Amazon tributary of Ecuador and Peru. *Journal of South American Earth Sciences, 31*, 45-53

Wren, D., Davidson, G., Walker, W., & Galicki, S. (2008). The evolution of an oxbow lake in the Mississippi alluvial floodplain. *Journal of Soil and Water Conservation, 63*, 129-135

Wu, M., Zhang, W., Wang, X., & Luo, D. (2009). Application of MODIS satellite data in monitoring water quality parameters of Chaohu Lake in China. *Environmental monitoring and assessment, 148*, 255-264

Xu, H. (2006). Modification of normalised difference water index (NDWI) to enhance open water features in remotely sensed imagery. *International journal of remote sensing, 27*, 3025-3033

Zhang, Y., Wang, P., Wu, B., & Hou, S. (2014). An experimental study of fluvial processes at asymmetrical river confluences with hyperconcentrated tributary flows. *Geomorphology*

VITA

Edward Park was born in Boston, Massachusetts. He attended Hyundai High School in Seoul, Korea. He received the degree of Bachelor of Art in Geography from the Ohio State University in 2010. In August 2011, he entered the Graduate School at the University of Texas at Austin.

Address: geo.edpark@gmail.com

This manuscript was typed by the author.